Azimuthal Anisotropy of Particle Emission at Target Rapidity Region in Pb + Pb 158 AGeV Collisions

Mizuki KURATA

A dissertation submitted to the Doctoral Program
in Physics, the University of Tsukuba
in partial fulfillment of the requirements for the
degree of Doctor of Philosophy (Science)

January, 1999

Abstract

The measurements of particle production at 158 AGeV Pb + Pb collisions had been carried out at the WA98 experiment in CERN SPS. Particles produced around the target rapidity region were observed by the Plastic Ball detector with a full azimuthal coverage. The particle identification for π^+, proton, deuteron and triton had been performed by using the $\Delta E - E$ particle identification method. This detector is suitable for the study of the characteristics of azimuthal anisotropy of particle emission, because of the full coverage in azimuthal angle and the particle identification capability.

In order to study the characteristics of particle emission at 158 A GeV Pb + Pb collisions, the azimuthal angle, Φ_0 was defined as the direction of total transverse momentum vector of protons, deuterons and tritons event by event. The azimuthal anisotropy of particle emission was studied by the subevent analysis related to the Φ_0. The experimental resolution of the Φ_0 was estimated as $\langle \cos(\Delta\Phi_0) \rangle = 0.377$ from this analysis.

The azimuthal anisotropy of particle emission with respect to the Φ_0 was studied for protons and pions as a function of centralities. Protons and pions showed anisotropic emission and protons tended to be emitted to the same direction as Φ_0, while pions were emitted to the opposite direction. The strength of the anisotropy, quantified as v_1, showed clear centrality dependence. Protons indicated maximum anisotropy at the mid-central collisions, while for pion the anisotropy showed monotonic increase towards peripheral collisions.

In order to understand the mechanism of those anisotropic emissions, the geometrical participant-spectator model with interaction processes was employed. Semiquantitatively, this model explained that the anti-correlation of protons and pions was produced by the absorption and the resonance process of pions and rescattering of protons with nucleons in the target spectator. As a result of these processes, it was found that protons show the tendency to be emitted to the azimuthal direction of the target spectator. This simple model calculation also suggested the importance of the secondary interactions in the target spectator. Motivated by this requirement, the intranuclear cascade model, RQMD was introduced. The RQMD gave consistent results with the model calculations and better reproduction of anisotropies of pions and protons.

From those model calculations, reaction mechanism of the anisotropies are semiquantitatively understood. Consequently, it was confirmed that the azimuthal direction of protons at the target rapidity region pointed to the

direction of the target spectator. Finally, we concluded that the Φ_0 pointed to the direction of the impact parameter vector. In this thesis, we established the technique to define the azimuthal direction of the impact parameter at 158 A GeV Pb + Pb collisions as a first time. This contribution is expected to provide a new additional information of particle production at 158 A GeV Pb + Pb collisions.

Acknowledgments

I express my great appreciation for Prof. K. Yagi and Prof. Y. Miake who guided me through my students days. They opened the load to study in the exciting field and continuously encouraged me to catch up the front of the research. Furthermore Prof. Y. Miake provided me the opportunity to join the WA98 experiment and to have extremely beautiful experiences during my staying at CERN.

I wish to thank Dr.K. Kurita, Dr.H. Sako and Mr.S. Kato who gave me many advises and helps with their talented technique for experimental physics. I also wish to thank Dr.T. Maruyama who provided me many important advises from the theoretical point of view. I acknowledge my Japanese collaborators: Ms.H.U. Sachiko, Dr.Y. Igarashi, Dr.A. Kumagai, Dr.T. Ikeda, Mr.S. Sato, Mr.K. Enosawa, Mr.K. Kanoh, Ms.Y. Miyamoto, Mr.Y. Yokota, Mr.T. Chujo, Mr.Y. Okuma, Mr.R. Higuchi, Mr.A. Kiyomichi, Ms.U. Sachiko, Mr.D. Miura, Mr.T. Ishibashi, Mr.H. Hayashi, Mr.T. Shimada, Mr.T. Hirano, Mr.M. Inaba, Mr.K. Koseki, Ms. M. Suzuki and Mr.T. Yoshikawa. I was very happy to have various discussions with those colleagues.

I would like to appreciate the WA98 collaboration, especially, two spokespersons: Prof. Hans Gutbrod who encouraged me any time perfectly and Dr. Terry C. Awes who advised me to get good results in straight forward. And I would like to thank Dr.M.L. Purschke who constructed the excellent analysis software and Mr. Tonny who provided his excellent techniques to carry experiments successfully. They always make me happy with their cheerful personality. And my successful results own to all of WA98 collaborators who operated huge amount of detectors and built excellent softwares. I wish to thank those peoples:
A.L.S. Angelis, C. Blume, D. Bucher, P. Donni, I. Doubovik, S. Dutt,
S. Garpman, F.J.M. Geurts, H. Å.Gustafsson, H. Kalechofsky, K.-H. Kampert, B. W. Kolb, Y.Y. Lee, H. Löhner, M. Martin, D. Morrison, H. Naef, B. K. Nandi, T. K. Nayak, S. Neumaier, P. Nilsson, P. Nomokonov, I. Otterlund, T. Peitzmann, V. Petracek, F. Plasil, W. Pinganaud, L. Rosselet,

J.M. Rubio, R. Santo, H. Schlagheck, T.H. Shah, B.C. Sinha, K. Söderström, P. Stankus, G. Stefanek, P. Steinberg, M. Sumbera, J. Urbahn, G.J.v. Nieuwenhuizen, Y.P. Viyogi, S. Vörös, B. Wysłouch, G.R. Young.
By their great efforts, the experiments was made possible. The success of the WA98 experiments provided me an ideal opportunity to study many interesting physics issues.

I wish to express my gratitude to the CERN accelerator division for the excellent performance of the SPS accelerator complex. I gratefully acknowledge the effort of all engineers, technicians, and support staff who have made possible the construction and operation of this experiment.

This work is supported by the PPE division of CERN, the Swiss National Fund, the International Science Foundation under Contract N8Y000, the Grant-in-Aid for Scientific Research (Specially Promoted Research & International Scientific Research) of the Ministry of Education, Science and Culture, JSPS Research Fellowships for Young Scientists and also by the University of Tsukuba Special Research Projects.

I also want to express my gratitude to the RIKEN Linac peoples, especially to Dr.I. Tanihata, Dr.K. morimoto, Dr.F. Tokanai, Dr.R. Kanungo, Dr.M. Ahmady who kindly supported me to establish this work.

Finally, this thesis never be completed without the love and support of my husband, Dr. Shunji Nishimura who has always been beside me and guided me how to survive among top physicists and he continuously encouraged me when I lost form.

This thesis is also dedicated to my parents, Sohei Kurata and Yoko Kurata and to my grandparents, Kishiro Kurata and Sizue Kurata and also to my sisters and brother, Machiko Kurata, Akemi Kurata and Yoshikazu Kurata. Certainly without their support and comprehension, I would never be what I am. I really wish my father and my grandfather find pleasure in my success from the heaven.

Contents

Chapter 1

Introduction

1.1 Overview

According to a strong interaction theory based on Quantum Chromodynamics (QCD), a phase transition from the normal matter to plasma phase of quarks and gluons would occur at sufficiently high temperature and/or high baryon densities. This new phase of matter is called as Quark Gluon Plasma (QGP). It is believed that the phase transition from QGP to hadronic gas took place at a certain stage of the evolution of the universe as early as several microseconds after the “Big Bang”. However, it is not proved experimentally, yet.

Lattice QCD calculations predict that the critical temperature of this phase transition is around $T_c = 150$ MeV, corresponding to an energy density of $2 \sim 3$ GeV/fm^3 [1]. This unusual condition is expected to be achieved in the laboratory using ultra-relativistic heavy ion collisions. In the central region of head-on nucleus-nucleus collisions, the energy density is estimated to be reached as high as $1 \sim 10$GeV/fm^3 [2].

Currently, ultra-relativistic heavy ion experiments have been performed using two facilities in the world. One is the Alternating Gradient Synchrotron (AGS) at Brookhaven National Laboratory (BNL) in USA with Au beam of $10 \sim 11$AGeV. The other is the Super Proton Synchrotron (SPS) at *Conseil Européen orgnaisation européenne pour la Recherche Nucléaire* (CERN) in

Geneva in Switzerland with Pb beam of 158 AGeV in the highest beam energy at this moment. The latter provides us the possibility to reach the highest energy density in the world at this moment. In near future, Relativistic Heavy Ion Collider (RHIC) at BNL also will be operated accelerating Au (100 AGeV) + Au (100 AGeV), where the higher energy density with a baryon-free (or low) environment would be produced. In Table 1.1, the leading facilities and the invariant mass per nucleon-pairs are listed.

Accelerator	Location	Projectile	Beam energy [AGeV]	$\sqrt{s}_{nn}$ [GeV]	First beam
AGS	BNL	^{16}O,^{28}Si	14.6	5.6	1986
SPS	CERN	^{16}O	60	11	1986
SPS	CERN	^{16}O,^{32}S	200	20	1986
AGS	BNL	^{197}Au	11.6	5	1992
SPS	CERN	^{208}Pb	158	18	1994
RHIC	BNL	^{197}Pb	100	200	1999 ?
LHC	CERN	^{208}Pb	2760	5520	2005 ?

Table 1.1: Ultra-relativistic heavy-ions facilities: past, present and future.

1.2 Space-Time Evolution of Collisions

In Figure 1.1, the QGP phase diagram is shown together with paths expected in ultra-relativistic heavy ion collisions. Along these paths, space-time evolution of nuclear collisions is expected as following [3].

At the beginning, two highly Lorentz-contracted nuclei collide each other and inelastic nucleon-nucleon interactions redistribute the original beam energy into other degrees of freedom, like the production of transverse momenta, thermal energy and entropy. After a short time of about the order of 1fm/c, the highly excited and interacting zone may reach and pass beyond the phase boundary to the QGP phase.

Then the whole system expands outward into the vacuum, mainly along

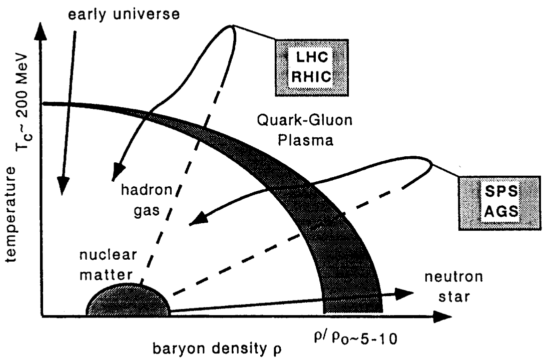

Figure 1.1: QGP phase diagram together with paths expected in ultra-relativistic heavy ion collisions [3]. The shaded band area qualitatively represents where phase transitions are expected to take place. The solid curves show paths expected in ultra-relativistic heavy ion collisions.

the transverse direction and cool down till it reaches the critical transition temperature T_c. The matter then stays in the mixed phase where hadronization of the QGP takes place. In particular, if the phase transition is of the first order, the lifetime of the mixed phase is expected to be long, e.g., of the order of 10fm/c.

Finally the system returns to a strongly interacting hadronic gas and expands to a large volume that all particles "freeze-out". Through this evolution, particles "freeze-out" when their mean free path is larger than the radius of the system, and stream away to detectors.

There are various signatures proposed to detect the formation of the QGP in the collisions. However, whenever we search the QGP signature, it is influenced by the hadronic gas which is formed after the phase transition from the QGP. Therefore, to confirm the signature of QGP, it is required to understand the property of highly dense matter and/or hadron gas, for instance, size, density, temperature, entropy, from the produced particles.

1.3 Participant-Spectator Model

Since nuclei are extended objects, their geometry plays an important role in the heavy ion collisions. Figure 1.2 and Figure 1.3 show a sketch of before and after the nuclear collision with a certain impact parameter, b, in the center of mass system. After the collision, each nuclei are separated into two regions. Nucleons interacted with other nucleons are called participant and those passing through beside the colliding region are called spectators. There are target spectator made from the target nucleus and projectile spectator from the projectile nucleus.

Such geometrical picture of collision becomes possible because of the following features of relativistic heavy ion collisions.

1. The de Broglie wavelength is much shorter than the radius of nucleus. Thus, nucleon-nucleon collisions become the elementary process of collisions.

2. The mean free path of nucleon-nucleon collisions in the nucleus is shorter than the radius of the nucleus.
   Thus, nucleon-nucleon collisions are expected where nuclei overlapped geometrically.

3. Momentum of incoming nucleons is much larger than Fermi momentum in the nucleus.
   Movements of nucleons expected from the Fermi momentum during the crossing time is negligible.

Based on this picture, it is suggested the experimental method to determine the impact parameter. in heavy ion collisions. That is to measure the energy of the projectile spectator at the zero degree in the polar angle. This method is effectively used in AGS and SPS experiments.

This model is one of the most important aspect of this thesis.

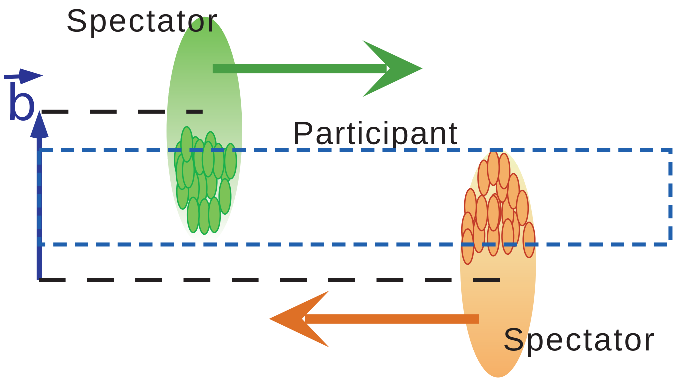

Figure 1.2: Schematic view of before colliding nuclei with a certain impact parameter, b.

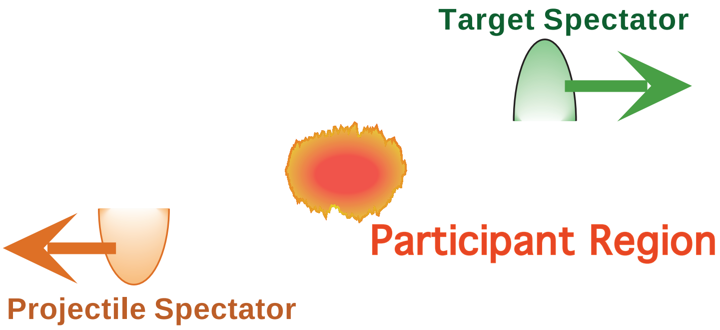

Figure 1.3: Schematic view of spectator and participant, after the collisions.

1.4 Hadron Measurement in High Energy Heavy Ion Collisions

One of the major goals of the high energy heavy ion collisions is to confirm the creation of high density and high energy state in the collisions, and hopeful to detect the formation of QGP. Study of the reaction mechanism from hadron productions is required for this purpose, and also very interesting by itself.

As a kinematical observable to measure hadron production in heavy ion collisions, rapidity and transverse mass distributions have been used in the various system. The definitions of them are given as;

Rapidity

$$y = \frac{1}{2} \log \frac{E + P_z}{E - P_z} \tag{1.1}$$

where E is a total energy and p_z is a longitudinal momentum along with the incident beam direction. Since the rapidity distribution does not change under the Lorentz transform, it is useful to compare among different energy system. From the rapidity distribution, the maximum baryon density achieved in the collisions can be estimated [2]

Transverse mass

$$m_t = \sqrt{{p_T}^2 + {m_0}^2} \tag{1.2}$$

where p_T and m_0 are the transverse momentum and the rest mass, respectively. For example, the transverse mass distributions measured at AGS energy are shown in Figure 1.4, Those spectra were measured for $\pi^{\pm}$, $k^{\pm}$ and proton in the system of p + p(Be), p + A(Au) and A(Au) + A(Au) [4, 5, 6]. A general feature which has emerged from those measurements of transverse mass is that the invariant distributions are approximately exponential in shape, that is,

$$d^2N/m_T dm_T dy \propto \exp(-m_T/T). \tag{1.3}$$

The inverse slope parameters, T are defined.

The transverse mass distribution is one of the most common tools used in studying high energy collisions. This is because the transverse motion is generated during the collisions and hence is sensitive to the collision dynamics.

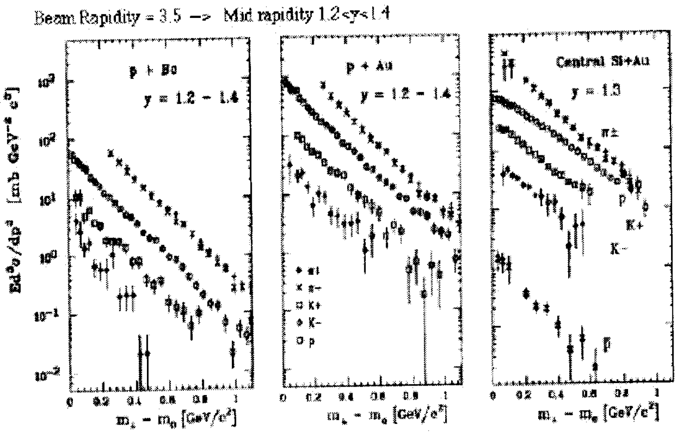

Figure 1.4: Rapidity transverse mass distributions at mid-rapidity, measured by E802 experiments at AGS for (left) p + p(Be), (middle) p + A(Au) and (right) A(Au) + A(Au) collisions.

1.4.1 Measurement with Impact Parameter Selection

In early experiments, the importance of determination of the impact parameter has been discussed in heavy nucleus collisions. Experimentally, it was found the strong dependence of the inverse slope parameter, T on the impact parameter. The slope parameter, T measured at AGS energy is plotted as a function of the centrality (impact parameter) for Si + Au (left) and p + Au (right) in Figure 1.5 [7]. In Si + Au collisions, the slope parameter, T of proton becomes larger towards the central collisions while pion's do not change much. On the other hand, no significant difference is seen in p + Au. It indicates that the reaction dynamics is gradually changed from large impact parameter (peripheral) to small impact parameter (central) collisions in the heavy system.

Furthermore, the impact parameter dependence was also found in the rapidity distribution. In Figure 1.6, the proton rapidity distributions measured for Si + Al (central and peripheral) and Au + Au (central) [8] are shown together with p + p [9]. A distinct feature is seen at central and peripheral collisions in Si + Al system. In the peripheral collisions, the distribution shows forward and backward peeks similarly with p + p collisions, which indicates, the peripheral collisions is understood as superpositions of the elementary collisions of nucleon + nucleon. However, in the central collisions those peaks are shifted to the mid-rapidity. It indicates that the initial beam energy is lost in the center of collision.

Those features suggest that the increase of the slope parameter and peak shift of the rapidity distribution are due to some kind of many body effects. Therefore, classification of collisions according to their impact parameters (called as centrality here after) are important for the measurements. The selection of collisions according the centrality provides us the additional information on the mechanism of particle production in high energy heavy ion collisions.

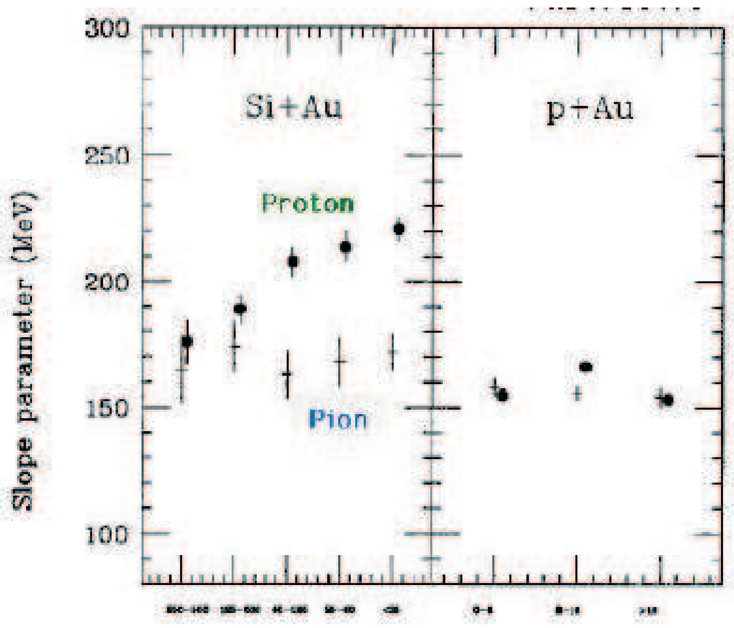

Figure 1.5: Slope parameter, T as a function of centrality. The left panel shows Si + Au collisions and the right panel shows p + Au collisions [7].

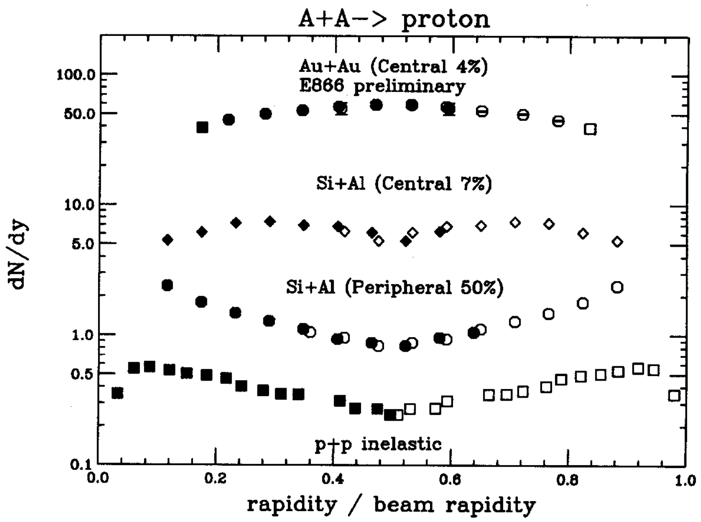

Figure 1.6: Proton rapidity distribution for Si + Al (central and peripheral) and Au + Au measured by E802 collaboration [8] at AGS. The p + p data are from Blobel [9]. The horizontal axis is normalized by the beam rapidity. The filled symbols are the measured data while the open symbols represent the data reflected at the mid-rapidity.

Chapter 2

Azimuthal Anisotropy

2.1 Overview

According to the Participant-Spectator Model, the number of participant nucleons is determined by the impact parameter of collisions. Since strength of many body effects varies with the number of particles, experimentally it was realized very important to measure any observables together with the number of participant nucleon. At that moment, the impact parameter was treated as the scalar value.

However, a new observable is proposed recently in ultra-relativistic energy concerning the direction of impact parameter [10, 11]. Particles produced in the central rapidity region may be emitted anisotropically on the transverse plane and preferentially onto the reaction plane. This speculation is associated with an anisotropic geometry of the participant region for non-central collisions: it has a smaller size in the direction of the impact parameter than in the perpendicular direction. (See Figure 2.1.) This anisotropic emission is caused by the difference of average number of rescattering due to different thickness of matter along with those two direction [12]. This picture is suitable for the case if the participant and spectator region is split sharply in a short time and if the high density matter is created in the center of the collision, which are expected in ultra-relativistic heavy ion collisions, like 158 AGeV Pb + Pb collisions. The study of the anisotropic emission with respect to the direction of the impact parameter is expected to provide additional information of particle production at high energy heavy ion collisions, for instance, nuclear potential effect, collective expansion, many body effect, signature of QGP [13], and so on.

For this study, there is an important requirement to the experiment, which is the extraction of the direction of the impact parameter. It has to be determined event by event because in the laboratory frame, the direction of the impact parameter should be random through all events.

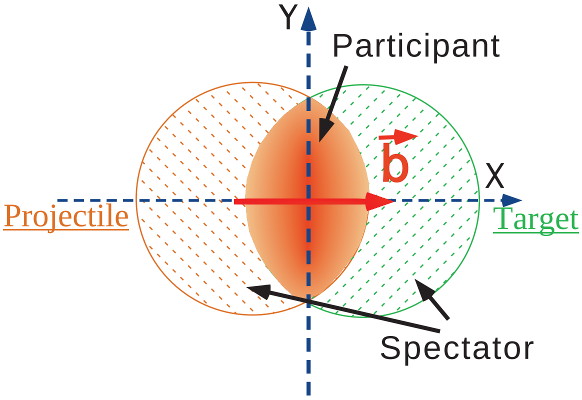

Figure 2.1: Beam view of colliding nuclei

Historically, it was firstly proved that the direction of the impact parameter vector can be determined in the beam momentum of $\leq$ 400AMeV [14] at BEVALAC. They could determine it from the shape of produced particle emission with a nearly 4 π coverage spectrometer for each event. Detailed studies [15, 16] and the developments of the analysis method [17] was carried out at BEVALAC and also at SIS [18, 19, 20, 21, 22] energies ($\leq$ 1 AGeV). However, this kind of 4π measurements is only possible for those low energy collision environment, due to less multiplicity and low energy of produced particles This is not realistic for higher energy collisions, like AGS and SPS.

Recently, those studies at ultra-relativistic energy have been carried out at AGS, Au + Au 11.4 AGeV by E877 collaboration [23]. They succeeded to extrapolate the direction of the impact parameter vector by measuring the transverse energy of produced particles with calorimeters. Based on this study, they found the essential features of particle emission pattern in high energy heavy ion collisions. Technical details and observations are discussed later in this chapter.

In the following sections, we introduce the definition of the impact parameter vector, $\vec{b}$ and the reaction plane. Then technical details which is applied to determine the $\vec{b}$ at AGS experiment are explained. Finally, we introduce the motivation of this thesis.

2.2 Impact Parameter Vector $\vec{b}$

Here, the direction of the impact parameter vector, $\vec{b}$ and the reaction plane are described. In the nucleus-nucleus collision, the scale of the impact parameter is given by the distance between the center of two nuclei. The direction of $\vec{b}$ is defined as the direction from the center of the projectile to the center of the target nucleus on the transverse plane as is sketched in Figure 2.2. Also, the reaction plane is defined as a plane spanned by a collision axis and the impact parameter as schematically depicted in Figure 2.3.

Because the directions of $\vec{b}$ are random through all events in the laboratory frame, a detector with full 2π azimuthal coverage is required to determine the direction of $\vec{b}$ experimentally.

2.3 Review of AGS experiments

2.3.1 Method to Determine $\vec{b}$ Applied at AGS

The method to extract the direction of $\vec{b}$ was established at 11.4 AGeV Au + Au collisions by AGS-E877 collaboration [24, 25, 26, 27]. In the E877 setup there are two calorimeter: one is Target Calorimeter (TCAL) and another is Participant Colorimeter (PCAL). The TCAL measures the transverse energy, E_T with 2π azimuthal coverage in the region of about $48^o < \theta < 135^o$ in polar

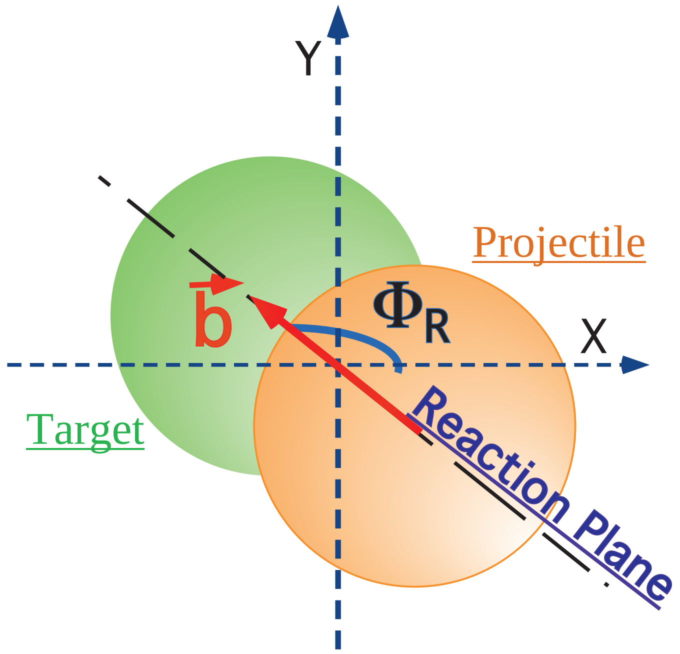

Figure 2.2: Definition of direction of the impact parameter vector $\vec{b}$ on the transverse plane in the beam view.

angle, which corresponds to the target rapidity region ($-0.5 < \eta < 0.8$ in pseudo-rapidity). The PCAL is a lead/iron/scintillator sampling calorimeter for measuring the transverse energy in the polar angular region of $1^o < \theta < 47^o$ with full azimuthal coverage, corresponding to the beam rapidity region ($0.83 < \eta < 4.7$).

Utilizing the full azimuthal coverage of those calorimeters, transverse energies with azimuthal information were obtained;

$$\begin{aligned} E_T &= \sum_{i=1}^{N} E_{Ti} \\ E_x &= \sum_{i=1}^{N} E_{Ti}\cos(\phi_i^{lab}) \\ E_y &= \sum_{i=1}^{N} E_{Ti}\sin(\phi_i^{lab}) \end{aligned}$$

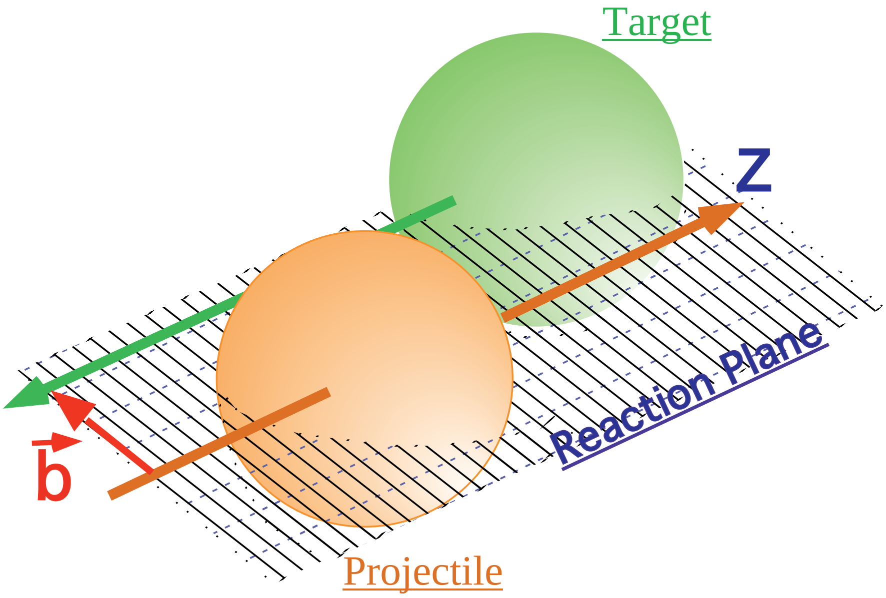

Figure 2.3: Schematic picture of the reaction plane is drown.

$$\begin{aligned} \vec{E_T} &= (E_x, E_y) \\ \Phi^{f(b)} &= \arctan(\frac{E_y}{E_x}) \end{aligned} \tag{2.1}$$

where i is the index of each cell of the calorimeter and ϕ_i^{lab} is the azimuthal angle of the cell in the laboratory coordinate. Thus the $\Phi^{f(b)}$ is defined as the azimuthal angle of the total transverse energy at forward (backward) hemisphere in each for every event [25]. In Figure 2.4, the azimuthal distributions of $\Phi^{f(b)}$ accumulated for many events are shown on the right top and on the left lower side, respectively and those show almost flat distribution. However, a relative angle between Φ^f and Φ^b; $\Delta\Phi^{fb} = \Phi^f - \Phi^b$, presents a strong correlation, which peaks at 180^{o} as is shown on the right lower side. It indicates that the produced particles are not emitted isotropically and those direct to the opposite direction in the forward and backward region.

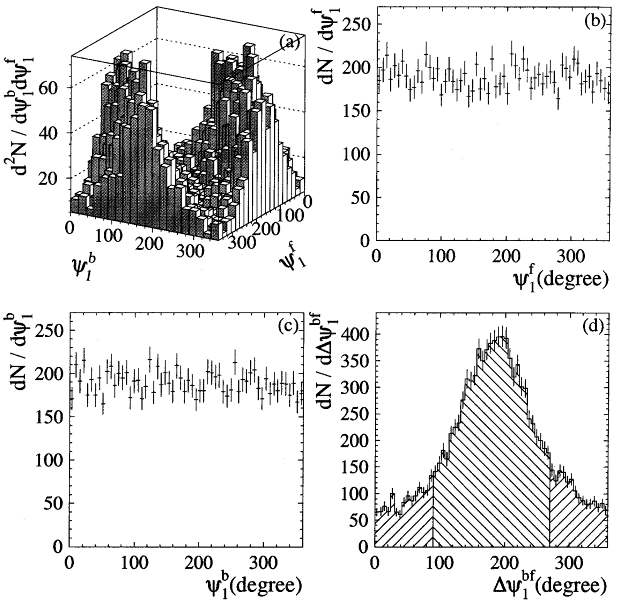

Figure 2.4: Azimuthal angle distribution of the total transverse energy at forward (b) and backward (c) hemisphere, $(\Phi^{f(b)})$. Difference of Φ^f and Φ^b is shown in (d) and correlation of them is shown in (a) [25]
.

This correlation is quantified by taking the ratio;

$$R = \frac{N\left(\left|\Delta\Phi^{bf} - \pi\right| < \pi/2\right)}{N\left(\left|\Delta\Phi^{bf} - \pi\right| > \pi/2\right)} \tag{2.2}$$

The ratio R depends strongly on the centrality, as shown in Figure 2.5. It reaches the maximum for mid-central collisions where $b \sim 4$fm, and approaches unity for peripheral and the most central collisions. This back-to-back correlation and the centrality dependence is understood from the relation with the the geometrical asymmetry of the target and the projectile spectator. They conformed that the Φ^b (Φ^f) points to the (opposite) direction of the impact parameter vector, $\vec{b}$ [25].

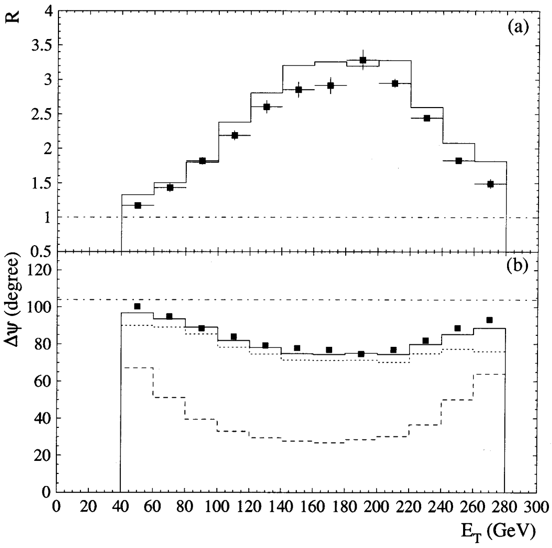

Figure 2.5: Strength of correlation of the azimuthal direction determined at forward and backward hemisphere. The definition of R is described in text [25]

.

2.3.2 Azimuthal Anisotropy of Particle Emission at AGS

Furthermore, protons and pions produced around mid-rapidity region was studied with respect to the direction of $\vec{b}$ [28]. A triple differential cross sections, $\frac{1}{N_0}\int\frac{d^3N}{dp'_x dp'_y dy}$ are reconstructed for those particles, where the new axis p'_x corresponds to the projection on the $\vec{b}$ determined from total transverse energy vector measured by calorimeters. Then the average transverse momentum transfer, $\langle p_x\rangle$ on the $\vec{b}$ is evaluated for wide rapidity region. Figure 2.6 shows that the $\langle p_x\rangle$ of protons reaches at the maximum around the target ($y = 0$) and around beam rapidity region ($y = 3.2$). The opposite sign of $\langle p_x\rangle$ between those regions indicates that protons tend to be emitted to the direction of the target or projectile spectators. For pion, smaller $\langle p_x\rangle$ is observed and it shows that pions tend to be emitted to the opposite direction to protons. The RQMD model well reproduce this data under the condition of with mean field, while it under estimates the data in the case of pure cascade. It is shown by the histograms in this figure. They argue the importance of the medium effect from this study.

It is claimed that an elliptic emission at mid-rapidity region was found in the azimuthal distribution of pions [24]. (See Figure 2.7). Pions are emitted more onto the reaction plane as is predicted [10, 11]. However it is so small that it might be due to the effect of the spectator or less energy density in the center of collision. Nevertheless, this measurement demonstrates the importance of the study at higher energy, where those effect is expected much less.

They found the remarkable features in the particle emission distribution in high energy heavy ion collisions. Those studies provide the new information for the study of hadron production in heavy ion collisions. Those fruitful observations owe to the successful extrapolation of the direction of the impact parameter, $\vec{b}$.

2.3.3 SPS versus AGS Energies

At AGS energy, they succeeded to extrapolate the direction of $\vec{b}$ and the remarkable features of the particle emission was observed at around the mid-rapidity region. The particles show weak elliptic emission pattern onto the reaction plane. This result suggests the importance of this study at higher beam energy, where higher energy density and less effect of the spectator is expected.

It is also observed that the azimuthal particle emission depends on the particle species, which is that pions are emitted to the opposite direction of nucleons. It suggests the importance of the particle identification for this study. In high energy heavy ion collisions, the proposed way for this study is to use a calorimeter with full azimuthal coverage as is done in the E877 experiments because of extremely high multiplicity of produced particles. However, it is not appropriate way in SPS energy. Since pion yield at 158

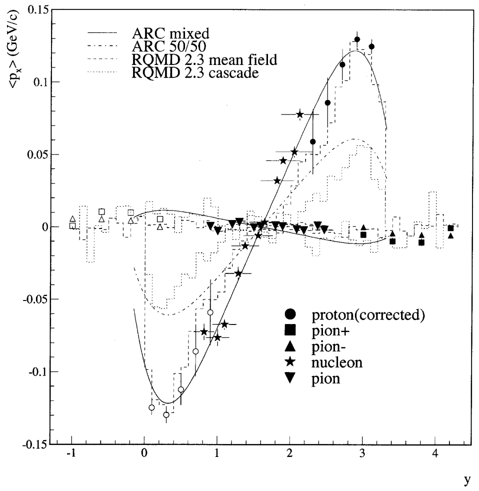

Figure 2.6: average transverse momentum transfer, $\langle p_x \rangle$ on the reaction plan measured by E877 experiments [28]

J. Barrette et al./Nuclear Physics A610 (1996) 63c–75c

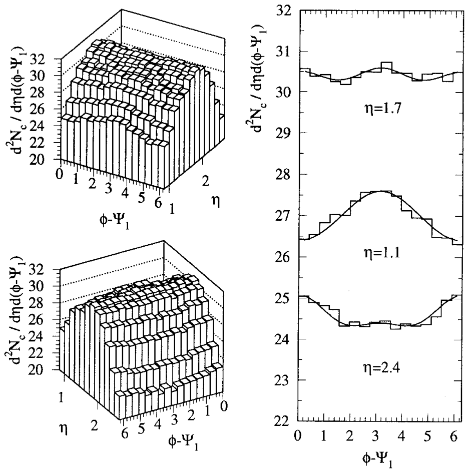

Figure 2.7: Charged particle multiplicity measured as a function of pseudorapidity and direction with respect to the direction of the impact parameter [24]. The left two panels are the same distribution plotted from two perspective. The right panel shows slices at three fixed η values

AGeV Pb + Pb collisions is much higher than 11.4 AGeV Au + Au collisions, the particle identification become more crucial problem in SPS energy.

2.4 Motivation of this Thesis

It is expected to be difficult to extrapolate the direction of impact parameter in SPS energy. Because of two strict requirements for this study, which are full azimuthal coverage and particle identification.

The main goal of this thesis is to establish the method to extract the direction of the impact parameter at 158 A GeV Pb + Pb collisions. This is the first trial at this energy. This is expected to provide the additional information for the study of particle production in 158 A GeV Pb + Pb collisions.

For this purpose, we implemented Plastic Ball detector, which provides full azimuthal coverage around the target region (polar angler range $70^{\circ} < \theta < 165^{\circ}$). And this detector can identify particles for π^+, proton, deuteron and triton by using a $\Delta E - E$ particle identification method and additional delayed timing information from π^+ decay. Thus the Plastic Ball is suitable for this study.

In this thesis, we discuss how to extrapolate the direction of the impact parameter vector from the particles observed at the target rapidity region. To confirm the our method, we study the azimuthal distribution for protons and pions. From comparisons of experimental results with a simple model based on geometrical spectator-participant model and an intranuclear cascade model RQMD, we conclude that the direction of the impact parameter can be determined at 158 AGeV Pb + Pb collisions.

This study is expected to provide the the additional degree of freedom for the study of particle production in 158 AGeV Pb + Pb collisions.

Chapter 3

Experimental Setup and Data Collection

3.1 CERN SPS

3.1.1 SPS Facility and Beam

The WA98 experiments was installed at the H3 beam line in West Area at the CERN SPS facility (See Fig. 3.1). Since 1994, the SPS has started to provide fully stripped lead beams (^{208}Pb) with momentum of 158 GeV per nucleon. This corresponds to 32.8 TeV in total energy.

The lead ions are produced by evaporation of the metal from a micro oven and fed into an Electron Cyclotron Resonance source (ECR). The source is a plasma generator which confines a plasma longitudinally in a magnetic bottle produced by a set of two solenoids. Radial confinement is achieved by a permanent magnet sextuple. The plasma electrons at the cyclotron frequency are heated and cause additional ionization. The ions which escape longitudinally out the ends of the source can be extracted. After injection from the Electron Cyclotron Resonance source (ECR), the partially stripped heavy-ion beam $^{208}\text{Pb}^{28+}$ with the momentum of 2.5 AKeV is accelerated by the LINAC3 up to 4.2 AMeV. After stripping to $^{208}\text{Pb}^{53+}$, the beam is again accelerated, firstly by the Proton Synchrotron Booster (PSB) to 95.4 AMeV, then by the Proton Synchrotron (PS) to 4.25 AGeV. After the PS acceleration, the second stripping of the lead ion is done before injecting in the Super Proton Synchrotron (SPS). Finally, the fully stripped $^{208}\mathrm{Pb}^{82+}$ will be accelerated up to 158 AGeV by SPS then delivered into the different experiments installed in the North and West Areas. In the acceleration phase, the stripping of the lead ions is done by passing the beam through carbon foils. In each acceleration stage, the output momentum, the efficiency, and the number of ions in SPS cycle are listed in Table 3.1. A full description of the CERN heavy-ion facility can be found in reference [29]. One cycle takes 19.2 seconds, with 14.4 seconds of acceleration and 4.8 seconds of extraction, which is often called as "spill". The typical rate seen by WA98 varied depending on the experimental configuration but reached a maximum of $1 \sim 2 \times 10^6$ ions per one spill.

Accelerator/Element	**Momentum**	**efficiency %**	**Pb ions/cycle**
ECR Source	2.5 AkeV		2.85×10^{10}
RFQ	250 AkeV	90	
Linac 3	4.2 AMeV	90	2.31×10^{10}
Stripper Foil		16	3.70×10^{9}
PSB	95.4 AMeV	24	8.88×10^{8}
PS	4.25 AGeV	67	5.91×10^{8}
SPS	158 AGeV	67	3.93×10^{8}

Table 3.1: Summary of output momentum, efficiency, and number of ions in each acceleration stage in SPS cycle. The overall efficiency between the ion source and the SPS extraction is 1.4 % [29]

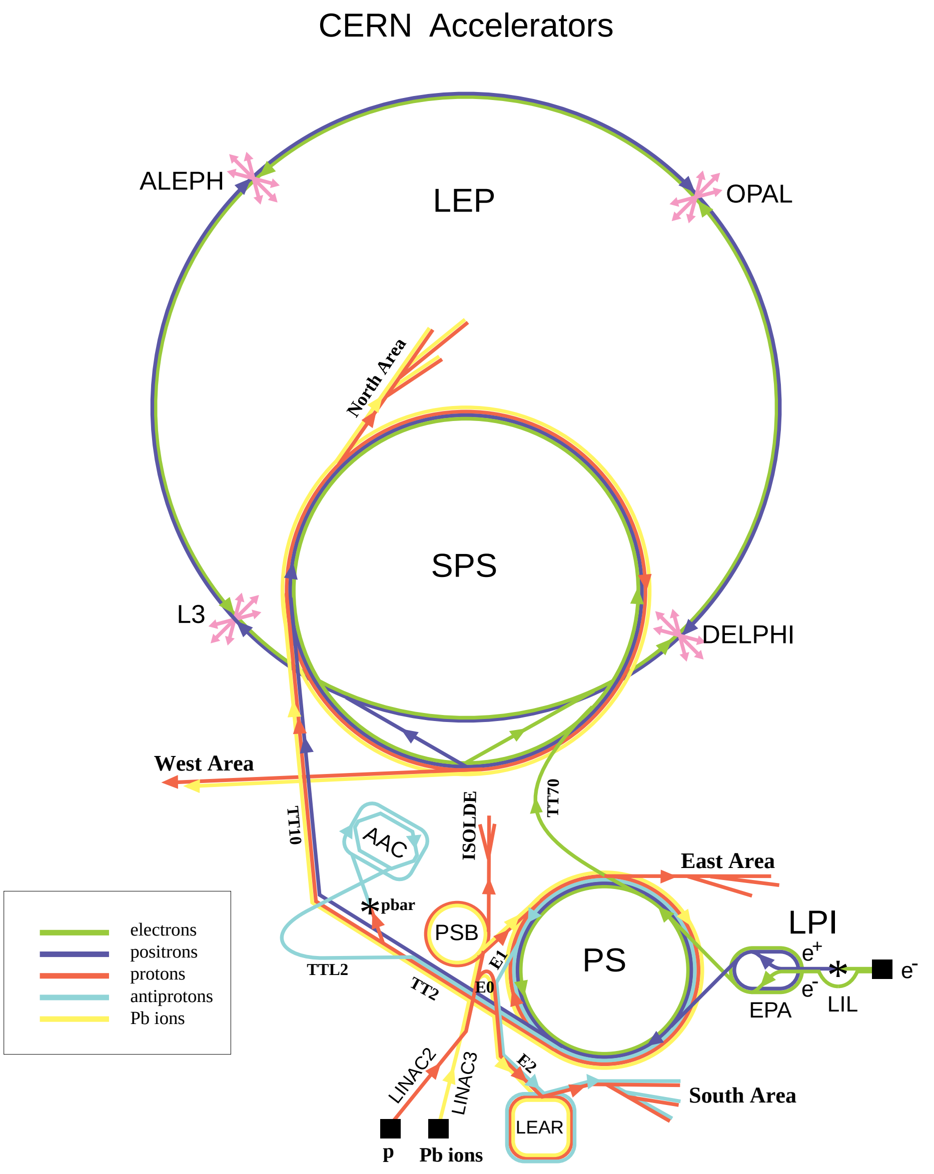

LEP: Large Electron Positron collider
SPS: Super Proton Synchrotron
AAC: Antiproton Accumulator Complex
ISOLDE: Isotope Separator OnLine DEvice
PSB: Proton Synchrotron Booster
PS: Proton Synchrotron

LPI: Lep Pre-Injector
EPA: Electron Positron Accumulator
LIL: Lep Injector Linac
LINAC: LINear ACcelerator
LEAR: Low Energy Antiproton Ring

Rudolf LEY, PS Division, CERN, 02.09.96

Figure 3.1: CERN accelerators

3.1.2 Target

During the beam time in 1996, several kinds of targets were used, e.g., not only lead but also nickel and niobium. The data were mainly taken with a 0.2 mm thick lead target. The types of targets are summarized in Table 3.2. The data presented in this thesis are limited only for ^{208}Pb.

Target name	Target	Thickness		
		mm	mg/cm^2	interaction probability
S1	^{208}Pb	0.210	239	$\sim 0.2\%$
S2	^{208}Pb	0.436	495	$\sim 0.5\%$
S3	Empty	0	0	
S4	^{58}Ni	0.250	223	
S5	^{93}Nb	0.254	218	

Table 3.2: Various kinds of targets used in WA98.

3.2 WA98 Apparatus

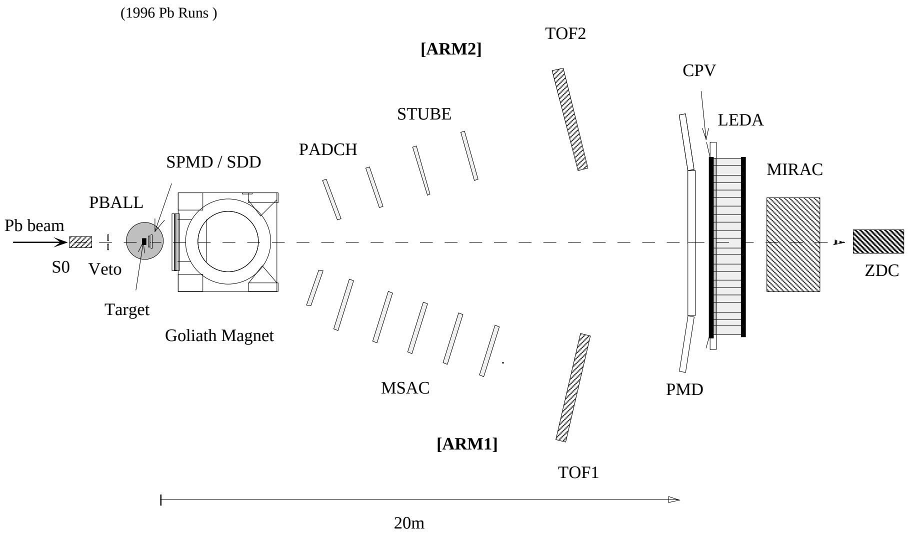

Figure 3.2: Schematic view of the WA98 experimental setup

3.2.1 Overview

The full apparatus of WA98 is briefly described in this section. The experimental setup of the WA98 apparatus is displayed in Figure 3.2. The WA98 experiment is uniquely designed to handle both of positive-, negative- charged and neutral hadrons and photons event by event with several types of detectors. These are roughly categorized into three types of detector system by their features; (1) event selection, (2) charged particle measurements, and (3) photon and neutral hadron measurements. The detectors categorized in the event selection are optimized not only for the interaction trigger but also for the selection of the rare events. The detectors for photon measurements provide the capability of detection for direct thermal photons created via hard quark-quark and quark-gluon processes. And the detectors for charged particle measurements enable us to study mechanisms of hadron particle production in highly condensed matter produced by high energy collisions.

1. **Event Selection**

   Beam-Counter
   Nitrogen gas cherenkov counter [30] was designed to measure lead ion beams with high timing resolution and with less radiation damage. This beam counter installed at 3.5 m up stream of the target had been achieving high detection efficiency close to ~ 100 % for the beam intensity of $1 \sim 2 \times 10^6$. This counter has two independent counter cells to evaluate their intrinsic timing resolution by themselves. The signals read by two photomultipliers of each cell was split into two lines, one goes into Time to Digital Converter (TDC) after three discriminators to obtain the precise start timing for the Time-of-Flight measurements. Another line are prepared for the pulse height measurement, which enables us to reject double beam events within the integration time of Analogue to Digital Converter (ADC) ($\sim 100ns$). The gas pressure was always kept at 1 atmosphere with continuous N_2 gas flow, so that

radiation damage should never happen in the radiator. The intrinsic timing resolution of $< 30ps$ was obtained stably during the whole runs.

Mid Rapidity Calorimeter (MIRAC)

The mid rapidity calorimeter (MIRAC) is located at 24 m downstream of the target which provides a total transverse energy, E_T in the rapidity interval of $3.5 < \eta < 5.8$. MIRAC has a hole of 10 cm in vertical and 40 cm in horizontal in the center to avoid the interaction with the beam or projectile spectators. The detector consists of 30 stacks, each divided vertically and horizontally into six towers (one tower has the geometry of $20 \times 20cm^2$) and segmented longitudinally into an electromagnetic and a hadronic section. The electromagnetic section of each tower is 15.6 radiation length (0.8 absorption length) and consists of alternating layers of lead ($3mm$) and scintillating plastic ($3mm$). The hadronic section is 6.1 absorption length deep and consists of layers of iron ($8mm$) and scintillator. The showers in both sections were read out through wavelength shifter coupled to photomultipliers. The calorimeter has a resolution of $17.9\%/\sqrt{E}$ for electromagnetic energy and $46.1\%/\sqrt{E}$ for hadronic energy. Further details of the construction and operations of this calorimeter have been described in the reference [31]. The centrality of each collision was determined by the total energy in MIRAC not only at online data taking but also at off line analysis.

Zero Degree Calorimeter (ZDC)

The zero degree calorimeter (ZDC) is a sampling uranium-scintillator sandwich-type calorimeter. It consists of 35 modules with (7×5) layers of lead and scintillator and read out by wavelength shifter. The dimension of this detector is $105 \times 75 \times 202cm^3$ which corresponds to 9 absorption lengths, This calorimeter was designed to be used to measure the energy of projectile spectator in the polar angle of $\theta < 0.3$ [Degree] with the energy resolution of $\sigma/E = 0.02 + 0.67/\sqrt{E}$. It is located at 30 m downstream of the target behind MIRAC. More details are described in the reference [32].

Veto Counters

Since it is important to reject particles produced at upstream of the target due to possible contaminations in the downstream detectors, two types of veto counters were installed before the target. The inner halo counter which consist of scintillation counter layers was located about 5.7 m upstream of the target. The little veto with a hole of $3mm$ diameter was installed at $2.7m$ upstream of the target to reject halo particles close to the beam axis.

Interaction Counter

An interaction counter which covers an area of $80 \times 80cm^2$ with an hole of 15 cm diameter was used to identify interactions at the target. It was located at a distance of about 25 cm downstream of the target.

2. **Charged Particles Measurement**

Plastic Ball (PBALL)

The Plastic Ball detector was originally built for experiments at the Bevalac accelerator in Berkeley and installed in WA98 to measure particles at the target rapidity region. The Plastic Ball is the main component of the detectors in this analysis. The details of this detector are described in section 3.2.2 and also in the reference [33].

Two Charged Particle Spectrometers, ARM I and ARM II

Goliath Magnet

The Goliath magnet is a 1.6 Tm dipole magnet with a gap size of 1600 mm. The center of the magnet was located at 3280 mm downstream of the target. The magnetic field was measured with hall probes in steps of 2 cm along the z direction and in steps of 4 cm along the x and the y direction, respectively. In total, 1.3×10^6 points were measured. The polarity of the Goliath magnet was mainly set in such a way that the negative particles were bended to ARM I side, while the positive particles were swept to ARM II side. During the 1996 run, the data with reversed polarity setting were also collected to cover larger acceptance and to test consistency between both spectrometers.

ARM l

On the negative x side, the charged particle spectrometer (ARM I) were located in the field free region after the Goliath magnet covering around the mid-rapidity region. This spectrometer was made of 6 tracking planes followed by a time-of-flight wall for particle identification. The tracking planes consist of six multi-step avalanche chambers [34] (MSAC) with optical readout by CCD cameras. The active area of the first chambers is $1.2 \times 0.8m^2$ and $1.6 \times 1.2m^2$ for the set of five chambers. After those chambers a time-of-flight wall was installed in the $15m$ downstream of the target. The ARM I provides the momentum resolution of $\Delta p/p \sim 0.94\% - 1.11\%p + 1.06\%p^2$ and the time-of-flight resolution of $< 120ps$ is achieved by using our analysis method. The time of flight detector with MSAC tracking enables us to identify pion, kaon and proton with the transverse momentum of < 1.0 GeV/c. Furthermore detailed descriptions can be found in [35, 36]

ARM ll

On the opposite side of ARM I, another spectrometer was installed in 1996 to measure positively (negatively in the reversed field) charged particles at the same time with negatively (positively) charged particles in ARM I around the mid-rapidity region. In ARM II, there are two pad chambers and two streamer tube chambers with pad-readout and a time-of-flight system in the behind of chambers. The ARM II provides the momentum resolution of $\Delta p/p \sim 1.03\% - 0.08\%p + 0.06\%p^2$ and the time-of-flight resolution of < 90 ps is obtained. The particle identification of pion, kaon and proton is carried out for the transverse momentum of < 1.0 GeV/c. Those spectrometers are not included in this analysis.

Silicon Pad Multiplicity Detector (SPMD)

The silicon pad multiplicity detector (SPMD) was located at $30cm$ downstream of the target. This detector is based on a double metal, AC coupled design consisting of approximately 4000 pads. The pads are arranged radially with 180 bins in ϕ angle and 22 equal-η bins $2.35 < \eta < 3.75$. The detector is composed of four identical quadrants, each with eight 128-channel readout chips. The signal from each channel were multiplexed and the four quadrants were digitized in parallel. Further detailed description can be found in [37].

Silicon Drift Detector (SDD)
The silicon drift detector covers a pseudo-rapidity range of $2 < \eta < 3.4$, locating at $12.5cm$ downstream of the target. It is made of silicon wafer with a thickness of $280\mu m$ and a diameter of $7.62cm$ with a hole of $15mm\phi$ in the center of the detector to avoid extra interaction with the incident beam. Electron clouds originated by particles on SDD were drifted and collected by the pads at the end. Digitization of the output signals from the 360 anodes was processed by a Flash-ADC system with a sampling rate of 50 MHz. The radial position of the hit was obtained from the drift time to reach these pads. Single hit resolution of $25\mu m$ along the drift direction and $35\mu m$ in the azimuthal direction were predicted.

3. **Photon measurement**

Lead Glass Calorimeter Array (LEDA)
The lead glass detector array (LEDA) is made of 10000 lead-glass modules which were designed to detect photon and neutral hadron. The LEDA detector is located at $21.5m$ downstream of the target. Each module is made of a $4 \times 4 \times 40cm^3$ lead-glass block and read out by photomultiplier tubes. High voltage (HV) to each photomultiplier tube was supplied by a newly developed on-tube, on-board Greinacher voltage multipliers, controlled by a VME based system. High stability and low noise of the LEDA system kept an excellent energy resolution which were confirmed by electron beams at CERN ($\sigma(E)/E =$

$5.5\%/\sqrt{E} + 0.8$). A full technical description of the HV system, the monitoring system and the ADC system can be found in the reference [38, 39, 40].

Photon Multiplicity detector (PMD)

The photon multiplicity detector (PMD) was designed as a large pre-shower instruments to measure photon multiplicity in the pseudo-rapidity of $2.8 < \eta < 4.4$. Photon conversion occurs in 3 radiation length of lead and it leaves an appreciable amount of energy about $\sim 70\%$, while hadrons convert only 15%. The secondaries shower were collected in ~ 40000 scintillating tiles read out through wavelength shifting fibers and digitized by a system of image intensifies coupled to CCD cameras. The digitized data was filtered through a cluster algorithm and the number of resolved clusters for each events corresponds to multiplicity of photon like particles, which contains an admixture of primary photons, photons from target and air conversions and background from hadrons that interact strongly and mimic a photon signal. Further details are described in the reference [37].

3.2.2 Plastic Ball Detector

Structure of the Plastic Ball

The Plastic Ball detector has full azimuthal coverage around the target region (polar angler range $70^o < \theta < 165^o$) with 655 detector modules The drawing of the Plastic Ball detector is given in Figure 3.3. Each module consists of two types of scintillators and one photomultiplier tube (PMT). In each module, ΔE and E signals are measured using slow and fast signals from these scintillators reading out by one PMT. The thickness of the $CaF_2(Eu)$ crystal was chosen to be $4mm$ and that of the plastic scintillator was optimized to $35.6cm$ to measure stopped proton spectra up to 240 MeV with high detection efficiency more than $\sim$ 80% (See Figure 3.4). Each module is wrapped with a double layer of aluminised Mylar foil ($6\mu m$) as an optical separator between adjacent modules.

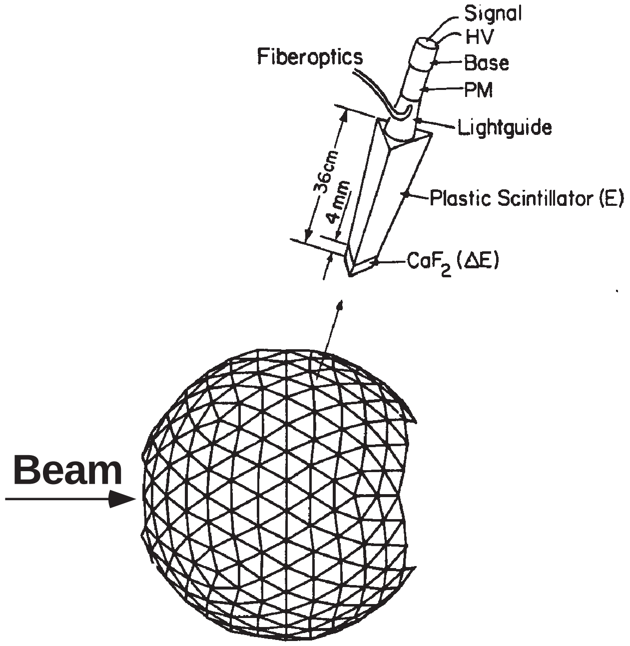

Figure 3.3: Sketch of Plastic Ball detector

The ΔE counter is made of a $CaF_2(Eu)$ crystal with a characteristic decay time of 1 μs. The light output from the $CaF_2(Eu)$ is 100 to 120 % of that of anthracene and is read out through the E counter. which serves as a light guide for the ΔE counter. The E counter is made of plastic scintillator and the light output from the plastic scintillator is about 45 % that of anthracene. The light emission of the plastic scintillator is approximately 100 times faster than that of the $CaF_2(Eu)$, so that 90 % of the E signals are measured within $10ns$, while the E signal is integrated over $80ns$. An optimal resolution has been found for the $\Delta E - E$ identification when the ΔE light integration lasts for $1.5\mu s$ and starts about $240ns$ after the start timing of the E signal.

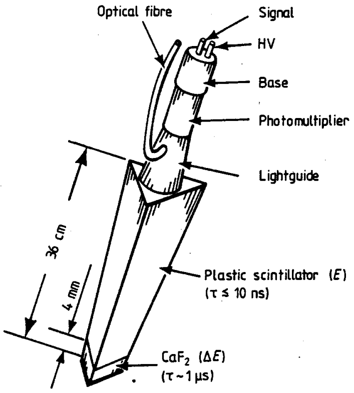

Figure 3.4: Sketch of Plastic Ball detector module

Pion Identification

In designing the Plastic Ball, special care was taken for detections of positive pions. In a pure $\Delta E - E$ identification scheme, the pions would be overshadowed by background produced by heavier particles. Thus, the additional requirement for the delayed signal from decay is applied in the identification of π^+ to eliminate those backgrounds. A stopped π^+ decays into a μ^+ and a neutrino with a mean life time of $26ns$ and a Q Value of $4.12MeV$. Then the μ^+ decays into a e^+ and two neutrinos with a mean life of $2.2\mu s$. In this decay the e^+ is emitted with an energy of up to $53MeV$ and produces a signal easily detectable in the plastic scintillator. This delayed signal from e^+ whose energy is more than 1 to 2 MeV, is measured by TDC with the gate width between $250ns$ and $10\mu s$ so that about 90 % of all the decay signal from $\pi^+ \rightarrow \mu^+ \rightarrow e^+$ is recorded.

This method cannot be used to detect negative pions, because the π^- are promptly absorbed by a nucleus [41] in the detector and most of the 140 MeV rest mass of the pion is released as kinetic energy.

3.3 Trigger and Data Collection

3.3.1 Trigger

The full WA98 experiment utilizes detectors of different readout speeds, from the nanoseconds achievable by the PMT-based detectors, to the milliseconds needed by the SPMD and PMD, to the very slow MSACs. Thus, the trigger system has been designed to interleave different trigger types, in order to read out the faster detectors while the slower detectors are busy.

In Table 3.3, we summarize the main trigger conditions referred to in this thesis. Coincidence is indicated by "+", anti-coincidence by "-" and a blank indicates that this signal is not relevant to the particular trigger. The main "beam" trigger is provided by the signal in two start counters and no coincident signal in the little veto and also no signal in the halo, which would indicate the passage of an off-axis beam halo particles. The hardware sum of the MIRAC energy, the signal in each tube weighted to simulate the $\sin\theta$ calculation, is fed into three discriminators with thresholds set to define three further event classes. The lowest threshold defines a "minimum-bias" physics event, where an interaction is thought to have occurred. The next highest threshold defines the upper bound on "peripheral" (large impact-parameter) events. The highest threshold then defines the lower bound on "peripheral" (small impact-parameter) events. Events which satisfy the peripheral condition but not the central condition are classified as "not-so-central". Particularly for peripheral events, a additional interaction trigger is provided by the threshold on the hardware sum of energy signals from the forward two rings in the Plastic Ball detector. Requiring this signal to be present lets us reject downstream interactions, where a beam particle or part of the halo strikes the beam pipe, causing a shower of significant energy that satisfies the minimum-bias trigger conditions. To optimize the use of the output tape drives, the different types of triggers are "scaled down", i.e. rejected randomly by factor of 2^n, to enrich various samples by decreasing the number of events of other types written to tape. Typically, peripheral events were scaled down by a factor of 16, N.S.C. by a factor of 8 and centrals are left alone, in order to keep rare high-multiplicity events.

Start counter	Little Veto	Inner Halo	Interaction counter	E_T			Trigger Condition
				Low	Peri.	Cent	
Accepted							
+	-	-					Beam
+	-	-		-	-	-	Clean Beam
+	-	-	+	+			Per. Int./Min bias
+	-	-	+	+	+	-	NSC Int.
+	-	-	+	+	+	+	Central Int.
Rejected							
+	+	-	-	-			Upstream Int.
+	-	-	-	+	+	-	Downstream Int.

Table 3.3: Main WA98 trigger condition.

3.3.2 Data Acquisition

The WA98 data acquisition (DAQ) is based on the QDAC system, originally designed as a "Quick Data Acquisition" for test beams, which was found to have a low enough overhead to be adequate for the full setup. Detectors are read out independently by OS9-based front-end processors running a Sub-

Event Builder (SEB) program. While each SEB process is capable of reading out every detector on the experiment, the program running on a particular processor is configured externally by reading in a "CAMAC Definition File" (CDF) that instructs the program which detector to read, how to read it, and assigns a subevent ID, which uniquely identifies the subevent on the data structure written to tape. The SEB processors are used for buffering as well as readout, a fact which allows one to distribute the data acquisition load more evenly by adding additional processors as needed. The processors communicate among themselves via TAXI (Transparent Asynchronous transmitter/receiver Interface) units connected by fiber-optic cables. Upon receiving a hardware trigger, a "trigger" process running on the main event builder requests the SEBs to read their subevents and store them in memory. When this is finished, they tell the trigger process that they are ready for the next event. SEBs are read out on any of three conditions: 1) The SEB memory is 80 rarely, 2) A spill-on event arrives, 3 seconds ahead of the actual spill, to flush the buffers of calibration events taken between spills, or 3) A spill-off event arrives, indicating that no physics events will happen for 14 seconds. At these times the main event builder (located near the tape drive) reads out the SEB buffers, constructs the full events, and writes out the events to a DLT2000 Digital Linear Tape. Thus, a minimum amount of data is written to tape during the spill, minimizing the arbitration overhead on the front-end processors, and maximizing the number of written events.

The WA98 data were written out in 400 MB segments, called "runs", each containing from 7000 $\sim$ 10000 events. The events were divided into three "trigger types", listed in Table 3.4. The trigger types are ordered by the integration time and readout speed of the detectors included. Type 1 events contain the various PMT-based detectors. Type 2 contains the multiplicity counters which have large event size. Type 3 is mainly for the optical-readout MSACs which had to be run at a lower rate than the other detectors. Each trigger type includes those detectors of lower types, i.e. Type 2 contains the Type 1 detectors, and Type 3 contains Types 1 and 2. This arrangement allows the faster detectors to collect data while the slower are busy, optimizing the use of the data acquisition.

Trigger type	**Detectors**
1	Trigger counters, Plastic Ball, LEDA, Calorimeters
2	CPV, ARM II, PMD, SDD, SPMD
3	ARM I

Table 3.4: Trigger types used by the WA98 trigger and data acquisition.

3.3.3 Data Production

The data used in this thesis was processed using the WA98 analysis package (ANPACK [42]) on a Silicon Graphics ORIGIN 2000. The basic structure of this analysis package was designed to handle file access and access to the events in a run. The off-line analysis codes were developed for each detector independently and complied together into the WA98_PB95 package. This package converted the output data run by run into Column-Wise Ntuple (CWN) for use with PAW [43].

In this thesis, totally 998 runs ($\sim$ 3.2 M Events) are analyzed for the lead target (S1).

Chapter 4

Data Reduction

4.1 Global Parameters

In the heavy ion collisions, it is important to classify each event by the centrality (the impact parameter) of collisions. For example, number of nucleons participated in the collisions varies from 2 to 400, collision environment from peripheral collisions (large impact parameter) to central collisions (small impact parameter) in Pb + Pb collisions. Therefore to study the reaction mechanism, in particular, the behavior in central collisions, selection of the impact parameter is very essential in the experiment.

In WA98 experiment, two detectors are installed to define the centrality in every event, one is the Mid-Rapidity calorimeter (MIRAC) which measures the total transverse energy of hadrons produced around mid-rapidity region and the other is Zero Degree calorimeter (ZDC) which measures the total energy of beam spectators. In Figure 4.1, the total transverse energy measured by MIRAC versus the total energy measured by ZDC are shown. The determination of the centrality of collisions using those measurements is authorized by this strong correlation.

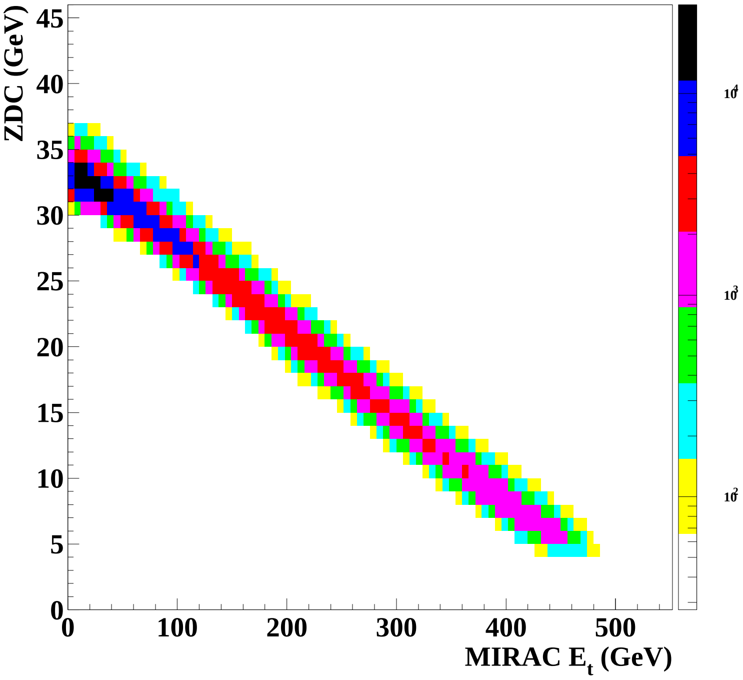

Figure 4.1: Correlation between transverse energy measured by MIRAC and total energy of beam spectators measured by ZDC.

4.1.1 Trigger Cross Section

Under the condition of a thin target, it is reasonable to assume that the probability of the interaction for each beam particle is small. The interaction cross section is associated with an area swept out by a beam nucleus passing through the target. The probability of the interaction is obtained by considering a point like target nucleus in that volume, where the assumption of thin target enables us to neglect double interaction in its target. The number of interaction is then given by:

$$N_{int} = P_{int} \times N_{Beam} \quad (4.1)$$

$$P_{int} = \rho_N \times \sigma_{int} \times t \quad (4.2)$$

where ρ_N is the number of nuclei in unit volume, t is the target thickness and σ_{int} is the interaction cross section. Thus the interaction cross section is given by

$$\sigma_{int} = \frac{N_{int}}{\rho_N \times t \times N_{Beam}}[mb]. \tag{4.3}$$

In the case of the Pb target, for instance, ρ_N is driven by

$$\begin{aligned} \rho_N &= N_A \times \rho/A \\ &= 6.023 \times 10^{23}[nuclei/mole] \times 11.35[g/cm^3]/208[g/mole] \\ &= 0.3287 \times 10^{23}[nuclei/cm^3], \end{aligned} \tag{4.4}$$

where N_A is the Avogadro number, ρ and A are the density and the mass number of the target material, respectively. The number of interactions must be corrected for the background contamination, which can be estimated by using target out events. In order to correct that number, the rescaling should be done with the same run condition as following

$$N_{int}(corrected) = N_{int} - N_{int}^{empty} \times \frac{N_{beam}}{N_{beam}^{empty}}, \tag{4.5}$$

where N_{int}^{empty} and N_{beam}^{emtpy} are the number of interactions and the number of beams obtained by the empty target run, respectively. After this correction, the minimum bias cross section obtained in the WA98 experiment is $\sigma_{int} =$ 6451mb. This number agrees with the geometrical cross section of Pb + Pb collisions which is estimated from the radius of the Pb nucleus ($R \approx 7.2$fm) as $\pi(2R)^2 = 6514$mb.

4.2 Definition of Centrality

The definition of the centrality of collisions used in this analysis is given by the total transverse, E_T energy measured by MIRAC. The E_T distribution observed in Pb + Pb 158 AGeV collisions is shown in Figure 4.2 In this analysis, we classify the collisions into 9 bins of centralities, namely, class A to class I as is listed in the table 4.1. The range of E_T, the mean E_T, and

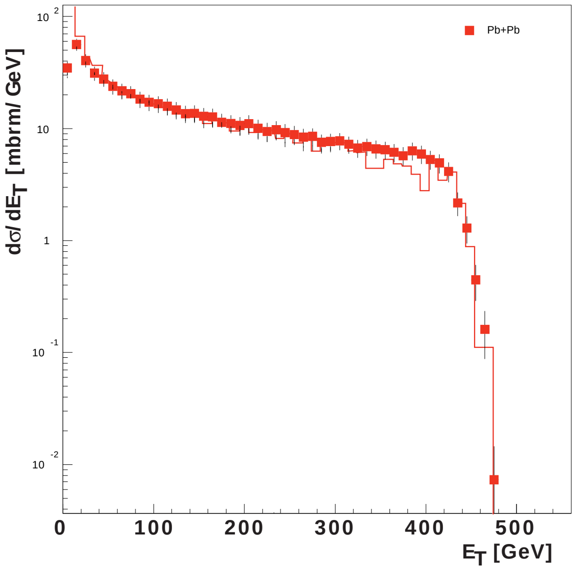

Figure 4.2: Transverse energy distribution measured by MIRAC.

the corresponding trigger cross section of those classes are also tabulated in Table 4.1. From this trigger cross section, an scalar impact parameter, b, of Pb + Pb collisions are estimated from a geometrical picture assuming sharp nucleon sphere of Pb nucleus as sketched in Figure 4.3:

$$\begin{aligned} \frac{\sigma_{int}}{\sigma_{tot}} &= \frac{\pi b^2}{\pi (2R_0)^2} \\ b &= 2R_0 \sqrt{\frac{\sigma_{int}}{\sigma_{tot}}}, \end{aligned} \tag{4.6}$$

where R_0 is the nuclear radius of Pb assumed to be 7.2 fm and the σ_{int} and σ_{tot} are the trigger cross section and the total trigger cross section in the minimum bias, respectively. The mean impact parameters, $\langle b \rangle$ in those centralities are also listed that table.

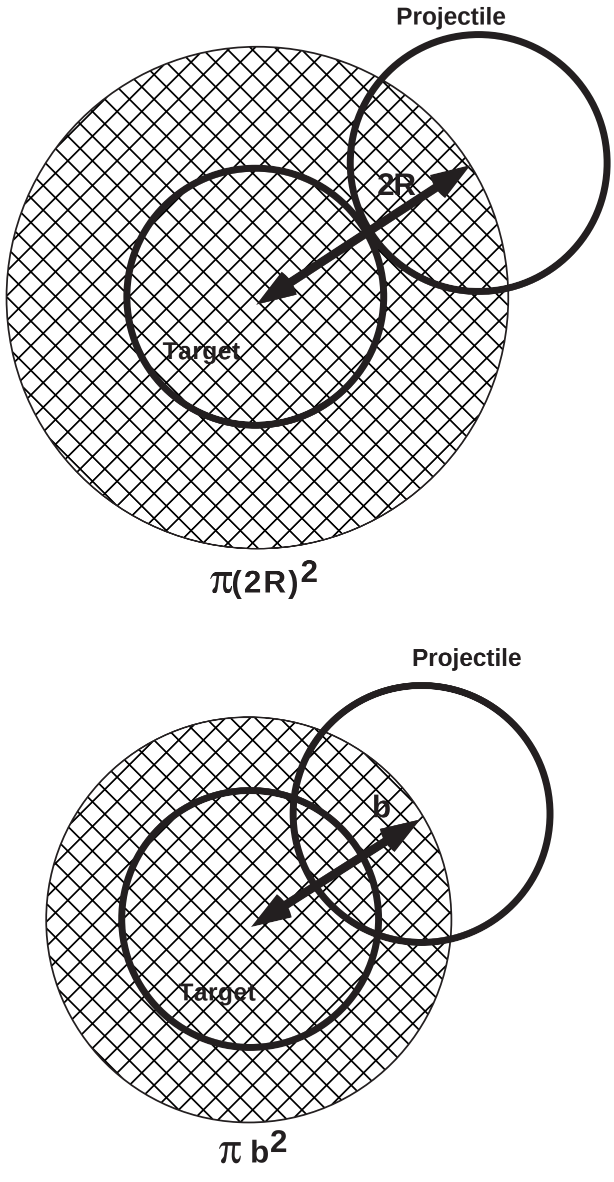

Figure 4.3: Schematic picture of geometrical cross section

Class	E_T [GeV]	$\langle E_T \rangle$ [GeV]	$\sigma_{int}/\sigma_{tot}$[%]	$\langle b \rangle$ [fm]
A	$420 \sim$	440.8	1.1	1.5
B	$380 \sim 420$	401.1	4.1	2.9
C	$350 \sim 380$	366.8	7.0	3.8
D	$320 \sim 350$	336.5	9.8	4.5
E	$280 \sim 320$	302.0	13.4	5.3
F	$200 \sim 280$	238.5	21.3	6.7
G	$100 \sim 200$	145.9	36.1	8.7
H	$50 \sim 100$	73.62	54.8	10.7
I	$0 \sim 50$	24.71	79.1	12.8

Table 4.1: Definition of Centrality. In the text, Class A to E are called central, Class F to H are called mid-central and Class I is called peripheral collisions.

4.3 Characteristics of Plastic Ball

4.3.1 Calibrations

In order to understand the geometrical properties and optimize the calibration method for the particle identification, an experiment was performed first at the Low Energy Pion Beam. An assembly of 13 Plastic Ball modules was placed in the beam defined by two $2 \times 2cm^2$ scintillation counters. A very important objective of the test was to obtain energy calibration curves for pions and protons. The geometrical light collection along with the particle path was measured with an electron source, and it was not constant, that is the light collection near the CaF_2 crystal was about a factor of two higher than near the photomultiplier. However, it was ensured that the light outputs from low energy proton and high energy pions were surprisingly linear with energy. After assembly each individual module of the Plastic Ball was calibrated at LBL 184-inch Cyclotron with 800 MeV and 400 MeV α beams. This procedure allowed the determination of the proper high voltage for each individual photomultiplier and of an important constant for each modules, the ratio of E to ΔE pulse heights at a given energy.

4.3.2 Performance

The following energy resolution (FWHM) were measured: for 75 MeV protons the Plastic Ball scintillator (E signal) had a resolution of 5 % and the CaF_2 crystal (Δ E signal) of 12 %. For the 800 MeV α beam the values were 2 % for the plastic scintillator and 10 % for the CaF_2. From the actual data and from the calibration measurements, correction factors for the ΔE and the E pulse heights could be derived to achieve the proper gain matching for all modules.

After this gain matching, the quality of the particle identification is shown for 420 modules between 70^{rmo} and 160^{rmo} in Figure 4.4. As is seen in this scatter plot between ΔE and E, the contamination is large at larger E region due to less energy deposit in the detectors by punch-through particles Those particles would be miss-identified and also give wrong energy value. To reduce the effect of contaminations, we only choose the $\Delta E > 30$[channel] and $800 > E > 156$[channel] for proton, deuteron and triton and $\Delta E > 50$ and $700 > E > 50$[channel] for pion in this thesis.

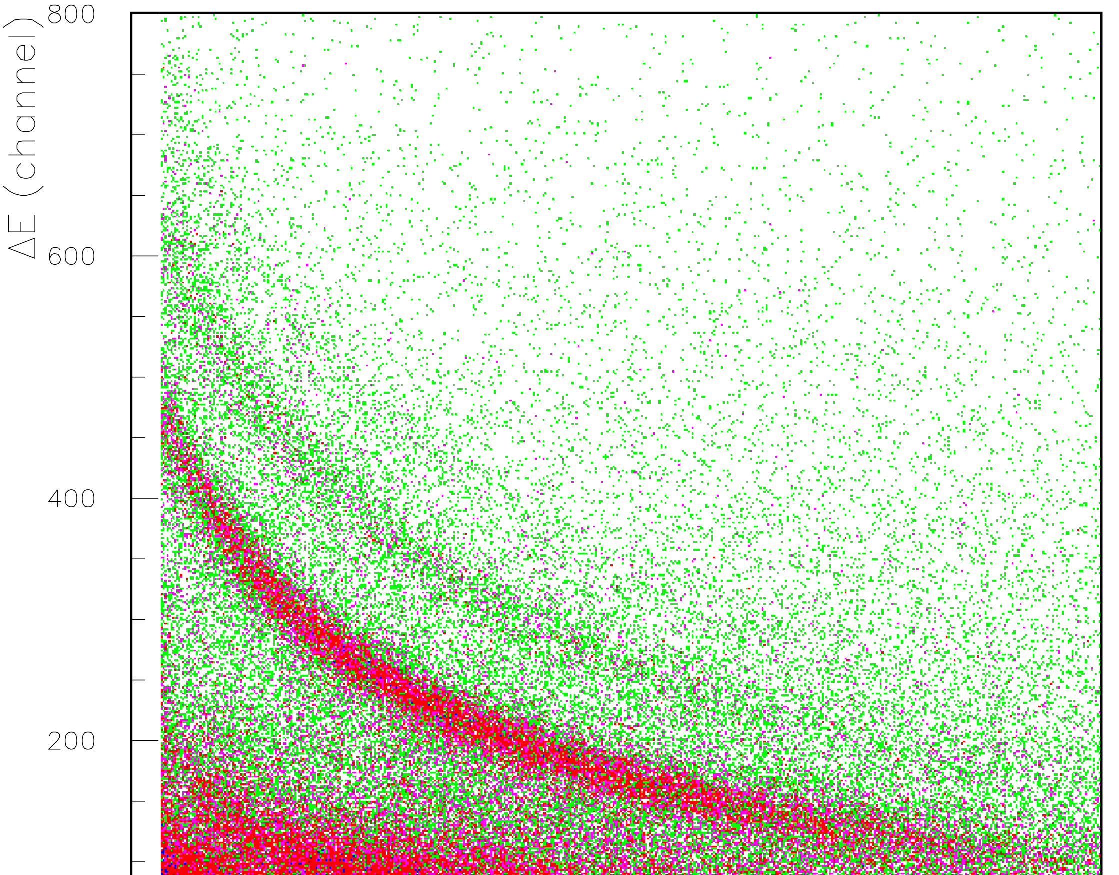

Figure 4.4: Scatter plots of dE and E measured by the Plastic Ball. Bands of several particles (pion, proton, deuteron and triton) are seen clearly.

4.3.3 Particle Identification

Concerning on separation of particles, linearized method which is suggested in early measurements [44] are applied by using the function;

$$PI(\Delta E, E) = \ln(\alpha \cdot \Delta E) + (\alpha - 1)\log(E + 0.5\Delta E) - \alpha \ln 300 \quad (4.7)$$

$$\alpha = a - b\frac{\Delta E}{T} \quad (4.8)$$

where, a and b are fixed parameters and T represents the thickness of the ΔE counter. In this experiment, $\alpha = 1.95$ is chosen for a good separation of proton and fragments. The scatter plots of $(\Delta E + E)$ as a function of $PI(\Delta E, E)$ is shown in Figure 4.5. The result proofs that the linearized methods works well. The projection of this plots on the x-axis is shown in Figure 4.6, where, protons, deuterons and tritons can be identified. This distribution is fitted by a function of three Gaussian distribution to extract the region of proton, deuteron and triton peak. Each particles are chosen within the three sigma of the Gaussian and the boundaries are drown in Figure 4.6 by the solid line.

Additionally, for better identification of pions, a delayed signal registered by TDC is required. The spectrum of the delayed signal is shown in Figure 4.7 with a fitting result of an exponential function, $\exp(-t/\tau)$. Here $\tau = 2.2 \pm 0.01 \mu s$ is obtained, which corresponds to the life time of μ-on. This requirement provides good quality pion samples as is shown in Figure 4.8.

The multiplicity distributions of identified protons and pions are shown in left and right half of Figure 4.9, respectively for the central, mid-central and peripheral collisions from the top to the bottom. The acceptance on the rapidity and the transverse momentum plane is shown for protons and pions in Figure 4.10, where zero rapidity indicates the target rapidity.

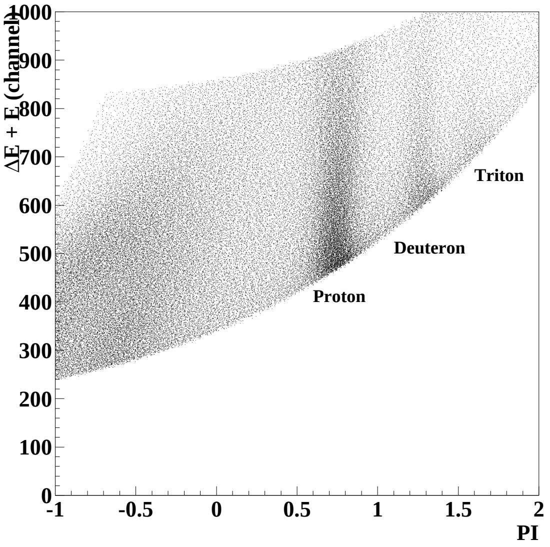

Figure 4.5: Scatter plots of $(\Delta E + E)$ versus $PI(\Delta E, E)$. The definition of PI is described in the text.

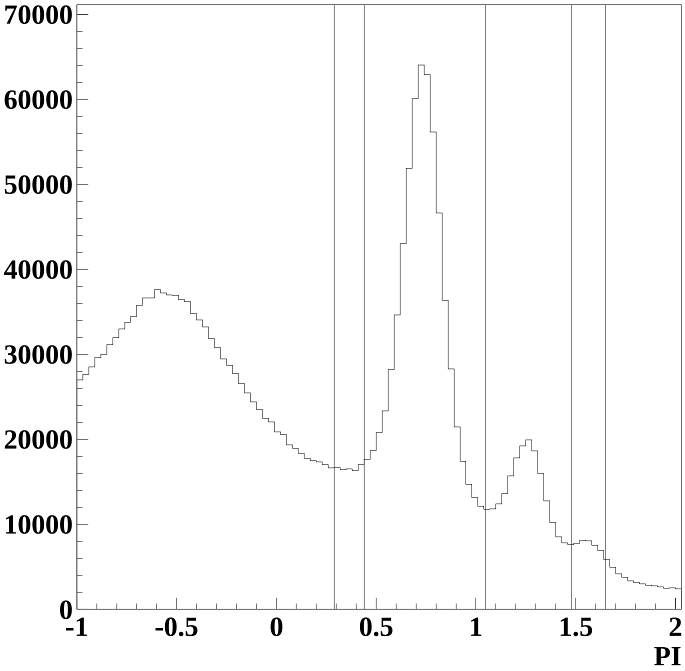

Figure 4.6: Particle identification spectrum. Horizontal axis is calculated from linearizing function, PI (See text)

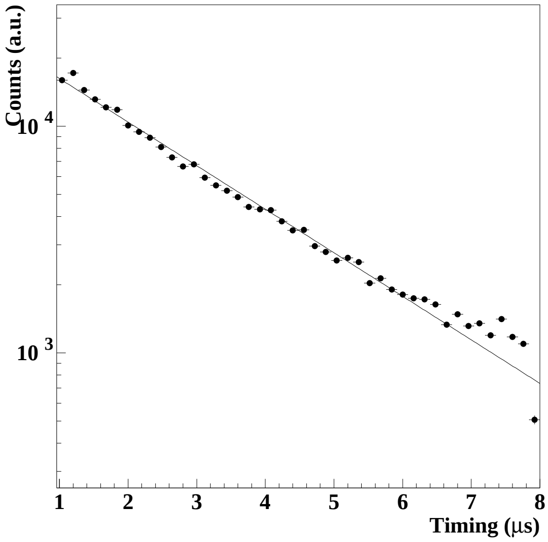

Figure 4.7: Timing spectrum of delayed signal with a fitting results of a exponential function. The inverse slope of the exponential function of $2.2 \pm 0.01 \mu s$ is obtained, which corresponds to the life time of μ-on.

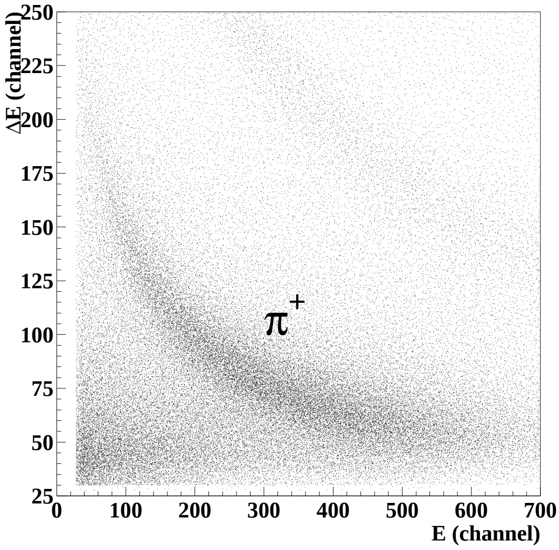

Figure 4.8: Scatter plots of ΔE and E with a requirement of delayed signals. The band of π^+ is seen clearer.

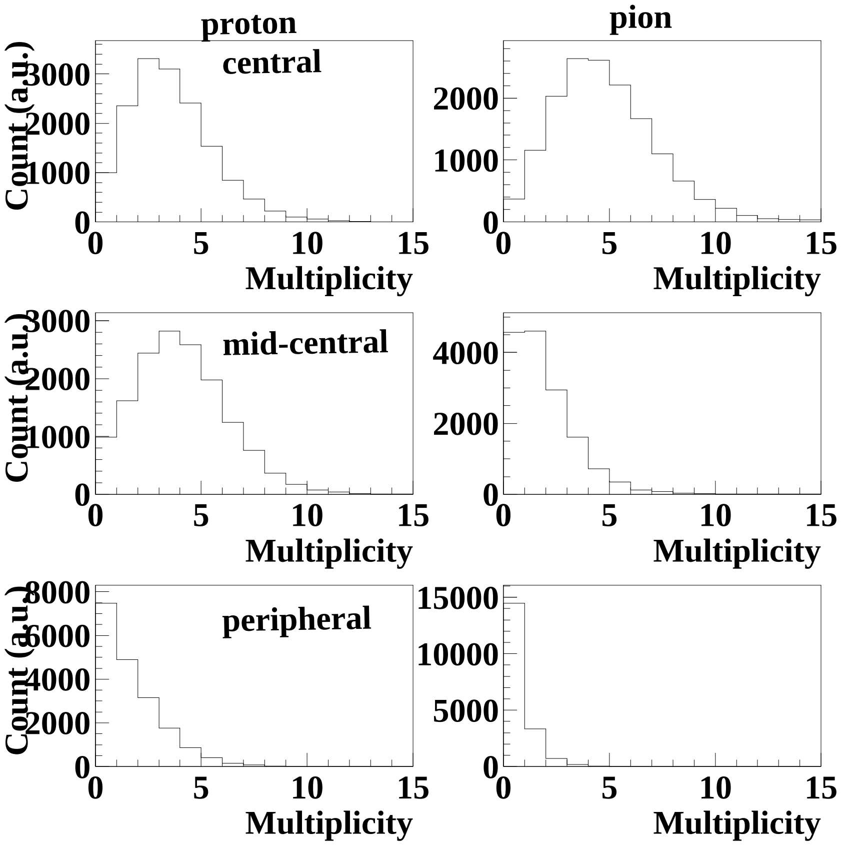

Figure 4.9: Multiplicity distributions of proton (left) and pion (right) for the central, mid-central and peripheral collisions from the top to the bottom.

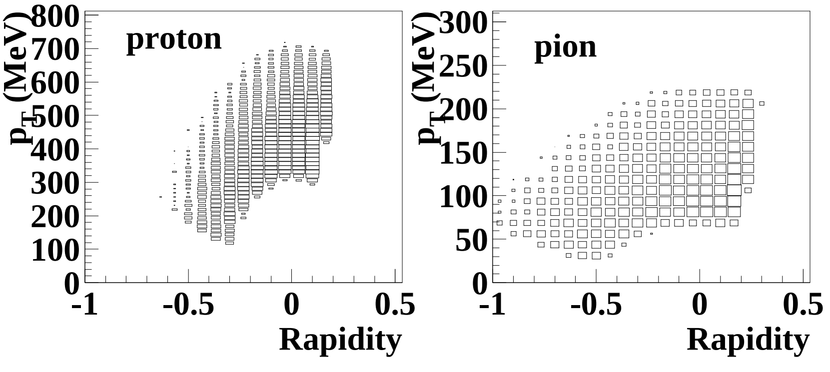

Figure 4.10: Acceptance of proton (left) and pion (right)

Pion Contamination

The pion contamination in protons is estimated by extrapolating the pion distribution described by the Gaussian function into the proton region (See Figure 4.11). The ratio of the contamination is estimated in Figure 4.12 for each centralities. The figure shows that the ratio increase gradually with increasing the centrality up to 24 %. This contamination is included in a systematic error in the following analysis.

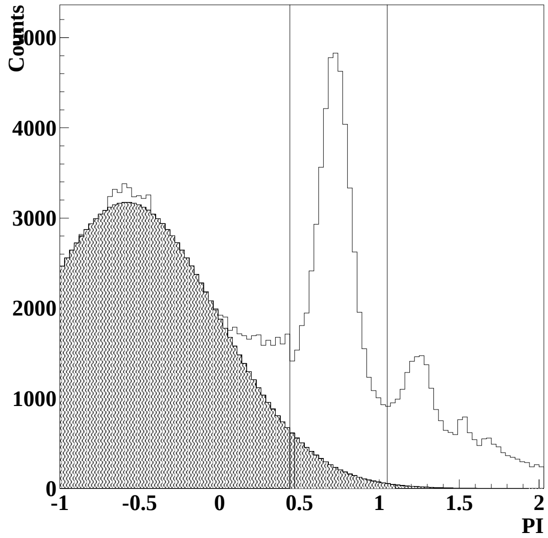

Figure 4.11: Particle identification spectrum. Pion distribution is described by the Gaussian function to estimate the contamination in proton samples.

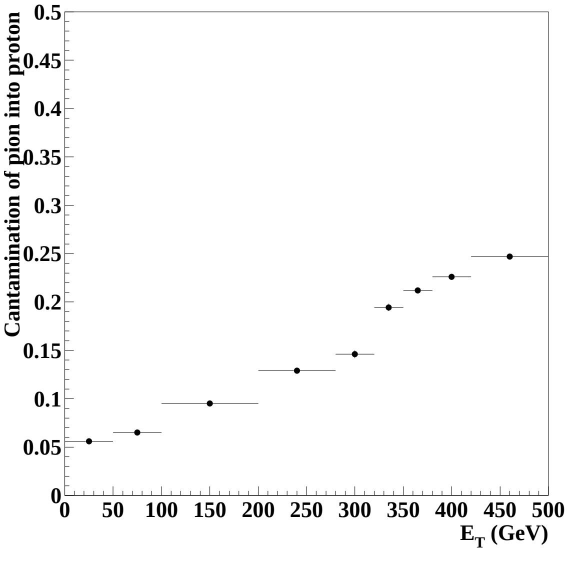

Figure 4.12: Pion contamination in protons as a function of E_T.

4.3.4 Cross Section

In relativistic heavy ion experiment, Lorents invariant cross section $E(d^3\sigma/dp^3)$ is transformed to the conventional form,

$$\begin{aligned} E\frac{d^3\sigma}{d^3p} &= \frac{d^3\sigma}{d\phi dy p_T dp_T} & (4.9) \\ &= \frac{d^3\sigma}{m_T dm_T dy d\phi} & (4.10) \end{aligned}$$

where m_T, E, y and ϕ are the transverse mass, total energy, rapidity and azimuthal angle of a particle, respectively. Furthermore, the transverse mass spectra is parameterized as

$$\frac{d^2\sigma}{2\pi m_T dm_T dy} = N_0 \cdot \exp\left(-\frac{m_T - m_0}{T}\right) \tag{4.11}$$

where T is called the inverse slope parameter, N_0 is a normalization constant and m_0 is a rest mass. From these parameterizations, the equation 4.11 is integrated to obtain the normalization constant,

$$\begin{aligned} \frac{d\sigma}{dy} &= \int \frac{d^2\sigma}{2\pi m_T dm_T dy} m_T dm_t \\ &= 2\pi N_0 T (T + m_0) & (4.12) \end{aligned}$$

To compare rapidity distributions in different centrality conditions, we use the rapidity density, $dN(y)/dy$ defined as

$$\frac{dN(y)}{dy} = \frac{1}{\sigma_{int}} \frac{d\sigma(y)}{dy}. \tag{4.13}$$

where σ_{int} is the interaction cross section which is determined previously (See section 4.1.1).

For the protons, the transverse mass distributions were shown in Figure 4.13 to 4.15 for central, mid-central and peripheral. Those distributions are fitted by Equation 4.11. The fitting results are also shown in these figures with solid lines. After this parameterization, the rapidity density is evaluated as a function of the rapidity in Figure 4.16

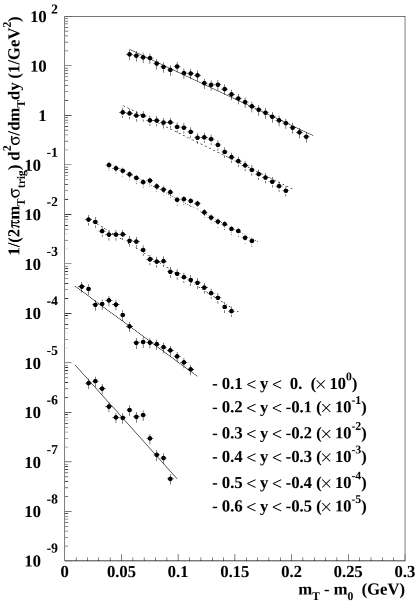

Figure 4.13: Transverse mass distribution of proton for the central collision ($420 \le E_T$GeV)

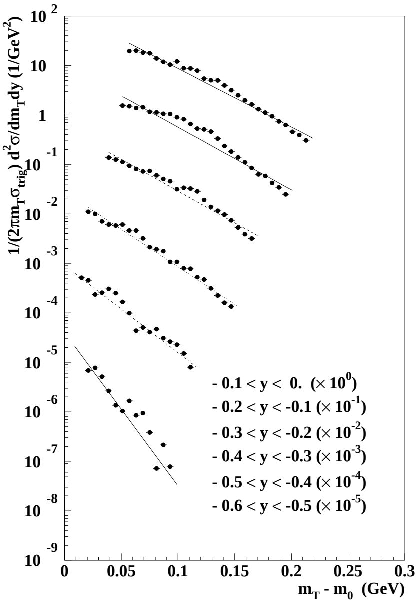

Figure 4.14: Transverse mass distribution of proton for the mid-central collision ($100 \le E_T \le 200$GeV)

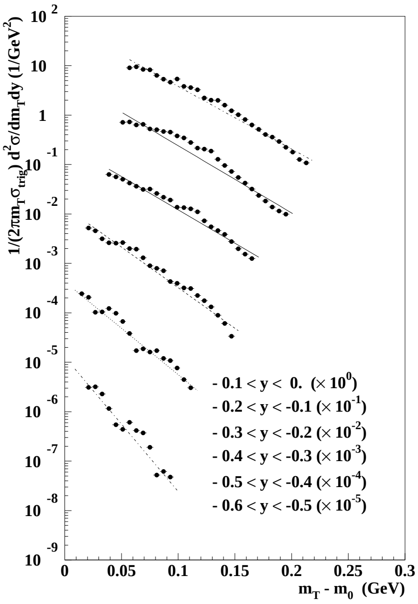

Figure 4.15: Transverse mass distribution of proton for the peripheral collision ($0 \leq E_T \leq 100$GeV)

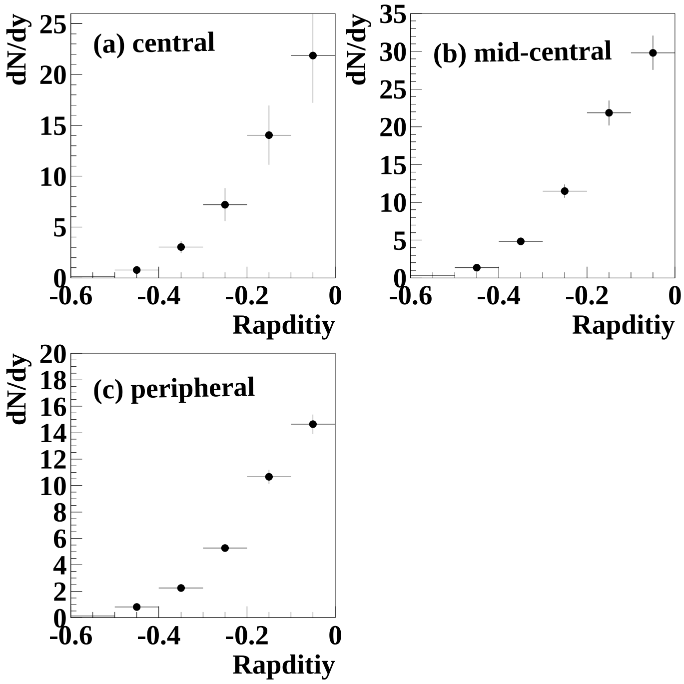

Figure 4.16: Rapidity distribution of proton

Chapter 5

Analysis and Results

5.1 Overview

The main purpose of this thesis is to investigate whether the azimuthal direction of the impact parameter vector, $\vec{b}$ can be extracted at 158 AGeV Pb + Pb collisions from the azimuthal particle emission. And also we like to understand the mechanism of particle emission at the target rapidity region. As introduced previously, the direction of $\vec{b}$ is claimed to be defined from the azimuthal distribution of produced particles in the earlier experiments. Applying the same technique, we extract the particular azimuthal direction, Φ_0, from the particles observed at the target rapidity region by the Plastic Ball detectors. Firstly, employing a subevent analysis, we study the azimuthal particle emission distribution from protons, deuterons and tritons. Those are measured and identified by the Plastic Ball. Secondly, we look into more details of the azimuthal distribution of pion and protons with respect to Φ_0. Then, the centrality dependence of the azimuthal distribution is analyzed for both particles.

5.2 Definition of Φ_0

At the beginning, we define a particular azimuthal angle, Φ_0, for every event from proton, deuteron and triton identified by the Plastic Ball using the following formula:

$$
\begin{aligned}
\mathbf{Q} \equiv [P_x, P_y] &= \sum_{\mu=1}^{M} \left[p_{t\mu} cos\phi_\mu, p_{t\mu} sin\phi_\mu \right], && (5.1) \\
tan\Phi_0 &\equiv \frac{P_y}{P_x}. && (5.2)
\end{aligned}
$$

where M is the total number of measured particles in each event, p_{t_μ} and ϕ_μ is the transverse momentum and the azimuthal angle in the laboratory frame of μ^{th} particles, respectively. So the Φ_0 gives the direction of the total transverse momentum.

The Φ_0 distributions accumulated within each centrality class are shown in the upper half of Figures 5.1(a-1),(b-1) and (c-1) for Class A ($420 < E_T < 500$ GeV), for Class G ($100 < E_T < 200$ GeV) and for Class H ($50 < E_T < 100$ GeV), respectively. Since the direction of the impact parameter vector is randomized through all events in the laboratory frame, the Φ_0 is expected to have flat azimuthal distribution under the condition of uniform detection efficiency. In all centralities, Φ_0 is nearly uniform within 5 % discrepancy from unit. Thereby we can expect the detector uniformity is $\sim 5\%$.

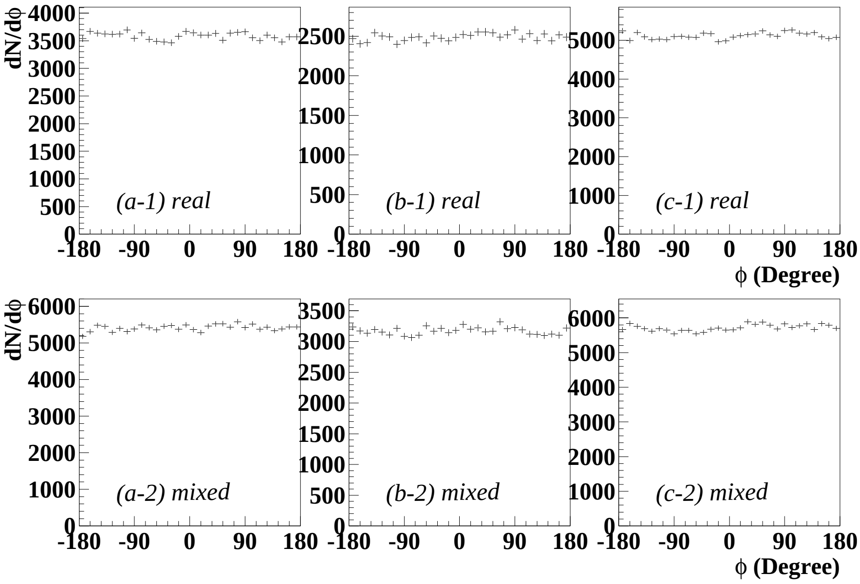

Figure 5.1: Azimuthal angle distribution of Φ_0 which is defined as the direction of total transverse momentum vector of proton, deuteron and triton. Upper half is for real events and lower half is for mixed events. And (a-1(2)), (b-1(2)) and (c-1(2)) correspond to Class A ($420 < E_T < 500$ GeV), Class G ($100 < E_T < 200$ GeV), and Class H (0 $50 < E_T < 100$ GeV), respectively.

5.3 Mixed Events Analysis

In order to test the possible detector effects such as acceptance, efficiency variation, granularity, statistics and so on, which may distort the distribution, fake events are created by collecting particles from different events. The data of 500 events (One event means one trigger.) which are analyzed in the analysis discussed previously are stored in a buffer. From this buffer, a certain number of particles are picked up randomly from independent events keeping the same multiplicity distribution probability as real events. Here, it is forbidden to share one module by more than 2 particles in one mixed event, because multiple hits would be regarded as one hit in real events.

Then, those fake events, called as "mixed events" are analyzed using the same analysis code performed for the real event. Firstly, the azimuthal angle evaluated by the total transverse momentum from the mixed events, Φ_0^{mix}, are shown in the lower half of Figure 5.1, for the corresponding centrality with the real events. Similarly, the Φ_0^{mix} are also distributed flat within 5 %. It can be said that the Φ_0 azimuthal distribution of the real events can be reproduced by the mixed events. Hence, the mixed events is used to correct the real events to exclude the detector effects in the following analysis.

5.4 Azimuthal Correlation

5.4.1 Subevent Analysis among Fragments

In order to study whether the azimuthal angle, Φ_0 is indicating a particular direction correlating with a reaction, a subevent analysis is applied among protons, tritons and deuterons In the subevent analysis, we divide each event randomly into two equal sized subevents.

From those subevents, Φ_a and Φ_b are evaluated as the direction of the total transverse momentum of each subevent similarly with Φ_0 (See Figure 5.2).

$$tan\Phi_{a(b)} \equiv \frac{\sum_{\mu=1}^{M_{a(b)}} p_{t\mu} cos\Phi_\mu}{\sum_{\mu=1}^{M_{a(b)}} p_{t\mu} sin\Phi_\mu}. \tag{5.3}$$

There, the events contain more than 6 particles are selected to require more than 3 particles in both subevents.

In Figure 5.3, the correlation between Φ_a versus Φ_b are shown for the mid-centrality (Class G:100 $< E_T <$ 200 GeV). It is observed that there are clear correlation between them. To make it clearer, the relative angle distribution normalized to unit, are shown in Figure 5.4(a) and (b) for the mid-central collisions (Class G:100 $< E_T <$ 200 GeV) and for the central collisions (Class B:380 $< E_T <$ 420 GeV), respectively. These figures demonstrates that these subevents have clear correlation. And it indicates that those protons and fragments tend to be emitted in the same direction.

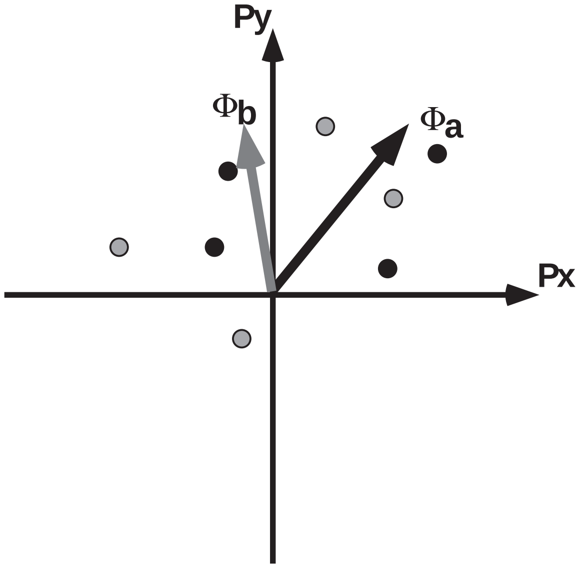

Figure 5.2: The transverse momentum distribution of one events on the transverse plane

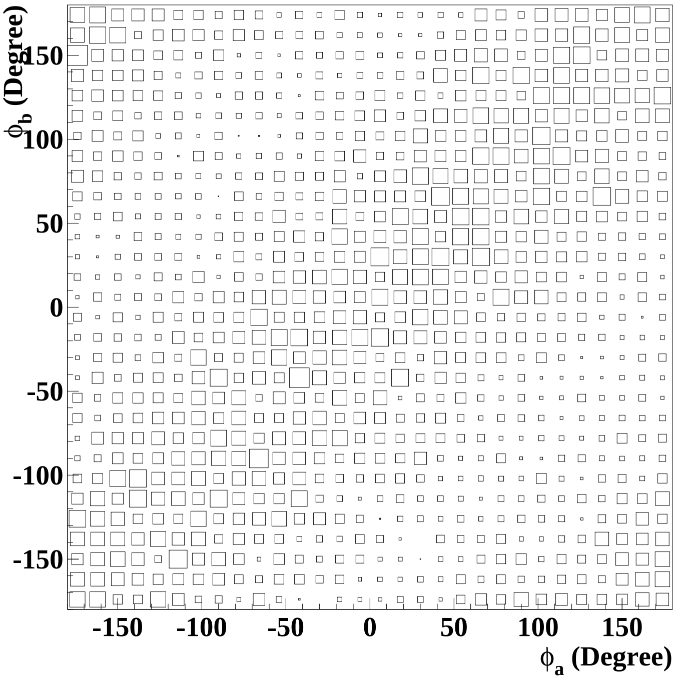

Figure 5.3: Correlation between Φ_a versus Φ_b

Particularly, in the mid-central collisions, strength of the correlation is found to be larger than the central collisions.

In order to quantify the strength of the correlation, the $(\phi_a - \phi_b)$ distributions are fitted with the cosine function as

$$\frac{1}{2\pi N}\frac{dN}{d(\Phi_a - \Phi_b)} = A_1 cos(\Phi_a - \Phi_b) + 1, \tag{5.4}$$

where, A_1 is the fit parameter indicating the strength of the correlations. This fitting procedure describes those distribution well as shown in Figure 5.4 with solid line. The fitted value of A_1 and χ^2 are listed in Table 5.1 for all centrality bins. Statistical errors only are shown.

Label	E_T [GeV]	A_1	$\chi^2/28$
A	420 ∼	0.0124 ± 0.006	0.572
B	380 ∼ 420	0.0236 ± 0.005	0.416
C	350 ∼ 380	0.0513 ± 0.006	0.477
D	320 ∼ 350	0.0712 ± 0.007	0.607
E	280 ∼ 320	0.0983 ± 0.007	0.361
F	200 ∼ 280	0.1294 ± 0.006	0.326
G	100 ∼ 200	0.1496 ± 0.005	0.487
H	50 ∼ 100	0.1194 ± 0.008	0.606
I	0 ∼ 50	0.0498 ± 0.014	0.417

Table 5.1: A_1 and χ^2 obtained for each centrality class

5.4.2 Subevent Analysis in Mixed Events

The subevent analysis is performed for the mixed events using the same code as the real events. The mixed events are randomly divided into two subevents and Φ_a^{mix} and Φ_b^{mix} are calculated accordingly. The relative azimuthal angle, $\Phi_a^{mix} - \Phi_b^{mix}$, are plotted in the left half of Figure 5.5 for the mid-central and the central collisions. In both centralities, there is no strong correlation not like real events, however, slight anti-correlation is seen.

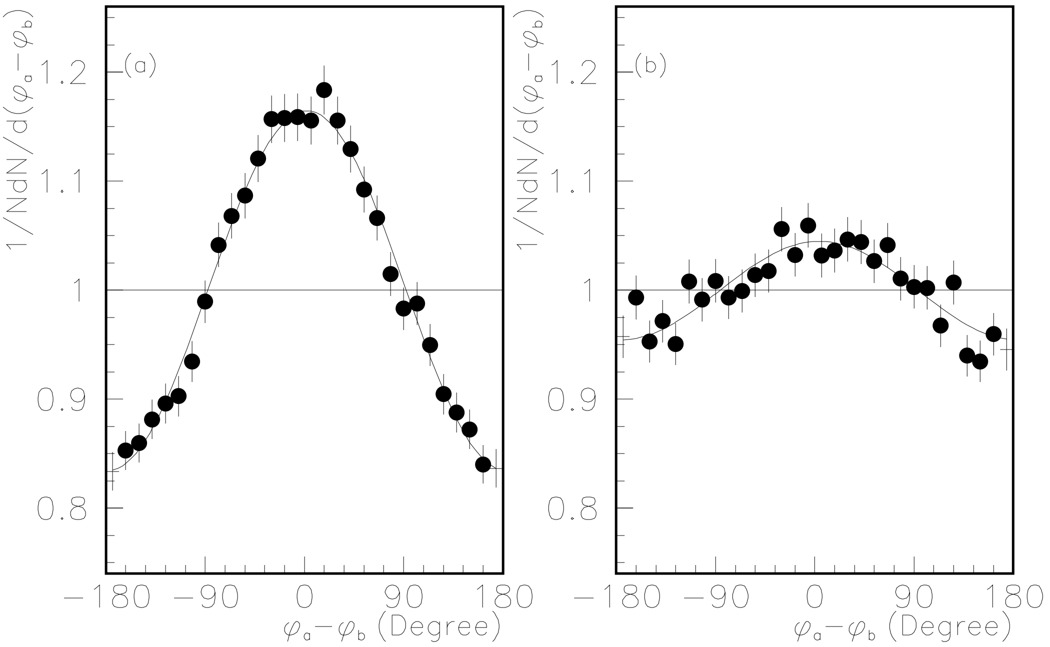

Figure 5.4: Distribution of $(\phi_a - \phi_b)$. (a)for the mid-central collisions (Class G:100 $< E_T <$ 200 GeV) and (b) for the central collisions (Class B:380 $< E_T <$ 420 GeV)

This small dip at around the zero degree is due to the finite detector granularity and an excluding multiple use of each module. When we allow multiple use of any modules, the small dip disappear completely as is shown in the left half of Figure 5.5. This effect of finite granularity is involved also in the real data. Thus, in order to eliminate this effect from the real data, we correct the real data by subtracting a distribution of mixed events from that of real events

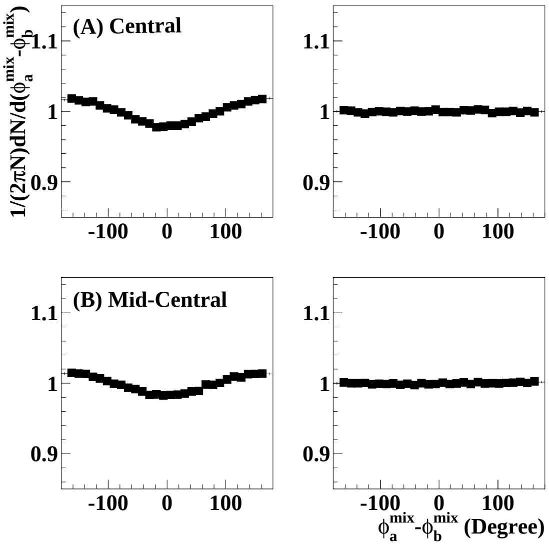

Figure 5.5: Relative angle distribution of two subevents in the mixed events. This small dip at around the zero degree in the left panels are due to the finite detector granularity and an excluding multiple use of each module. Because it disappear for the case of that the multiple use of any modules is allowed as is shown in right panels.

5.5 Azimuthal Distribution with Respect to Φ_0

5.5.1 Azimuthal Distribution of pions

In the preceding study, it is found that the particular azimuthal angle, Φ_0 can be obtained from the protons and the fragments (deuteron and triton). In this section, we study the azimuthal distributions of pions with respect to the Φ_0. The relative azimuthal angle, $\Delta\phi = \phi - \Phi_0$ of pion is analyzed as is shown for 9 centrality classes in Figure 5.6. Here, the correction by the mixed events are applied also. It is necessary for pion to exclude a neighboring hit effect which is further discussed in section 5.5.2.

The anisotropic pion emission is observed clearly for all centralities.

Unlike the correlation among fragments, the pions are found to be enhanced in the direction of $\Phi_0 = 180^o$. In another word, pions tend to emitted to the opposite direction of fragments. And this anti-correlation becomes larger in the peripheral collisions.

In order to quantify the strength of the anisotropy, it is fitted by the function:

$$\frac{dN}{2\pi N d(\phi - \Phi_0)} = 2 \cdot {v_1}' \cos(\phi - \Phi_0) + 1 \tag{5.5}$$

as is shown by the solid line in this figure. The value of ${v_1}'$ are obtained for each centrality.

5.5.2 Neighboring Hit Effect

We make use of the μ^+ decay channel to identify π^+ by the Plastic Ball. This μ^+ decays into positron with the life time of 2.2 μs and would deposit energy in one module. However, those positrons are emitted isotropically with a maximum energy of 53 MeV and have a high probability of leaving the module. With such a process, pions sometimes strew it's energy onto a few neighboring modules at the same time. In the Plastic Ball, we could distinguish if those decay signals originated from one π^+, scanning the delay signals which give the same timing of TDC. In order to estimate how many π^+ make a hit on neighboring modules, we plotted the multiplicity of every module for three cases in Figure 5.7. From the top, (a) is identified pions, (b) is the number of neighborings which have the same timing signal with the pion and (c) is (b) divided by (a). The probability of making neighboring hits are almost constant in full module not only in the mid-central but also central events. although the number of hit counts increase with higher number module ID, because of shifting toward the forward region. The averaged probability of $3.0 \pm 1.2\%$ is obtained in the central events.

Taking into account this factor, the detector biases are simulated in the mixed event analysis. In the mixed event, when one pion is picked up, we treat the neighboring modules as insensitive with a certain probability and

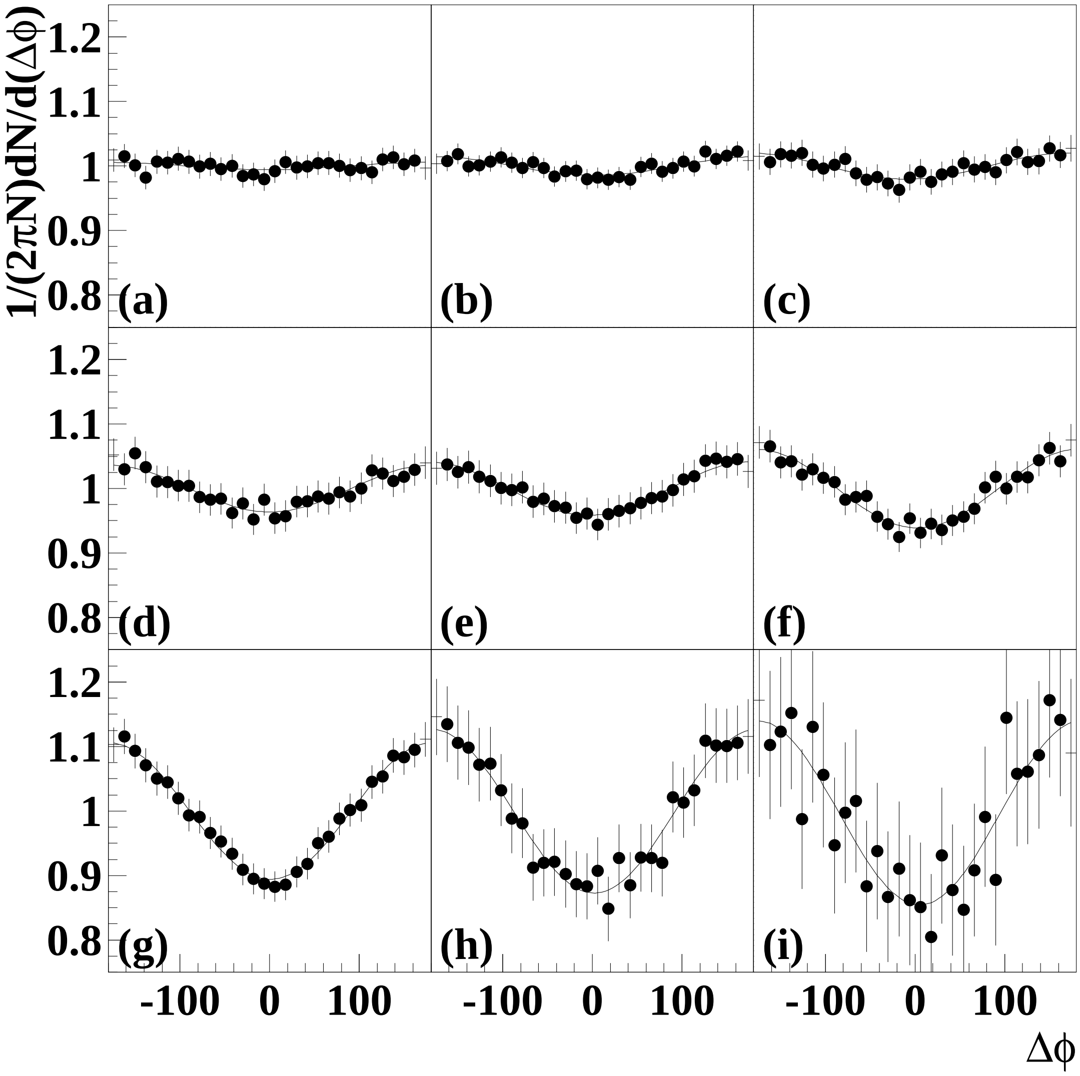

Figure 5.6: Azimuthal distribution of pion with respect to Φ_0. The distributions from (a) to (i) correspond to centrality class A to I.

carry out the analysis. The relative azimuthal angle distribution of pions with respect to the Φ_0^{mix} is plotted for the most central events to compare the real data in Figure 5.8: the left panel is the real data events and the right panel is mixed events when the probability of making the neighboring hit is 3.0%. The mixed events similarly show anti-correlation as is seen in the real event and the degree of anti-correlations are identical with the real data. It is known that this anti-correlation observed in mixed events is created by the excluding module effect due to the neighboring hits, so that it has to be removed from the real data. Therefore, we subtracted the mixed event distribution from the real data and this correction has been done in the preceding analysis.

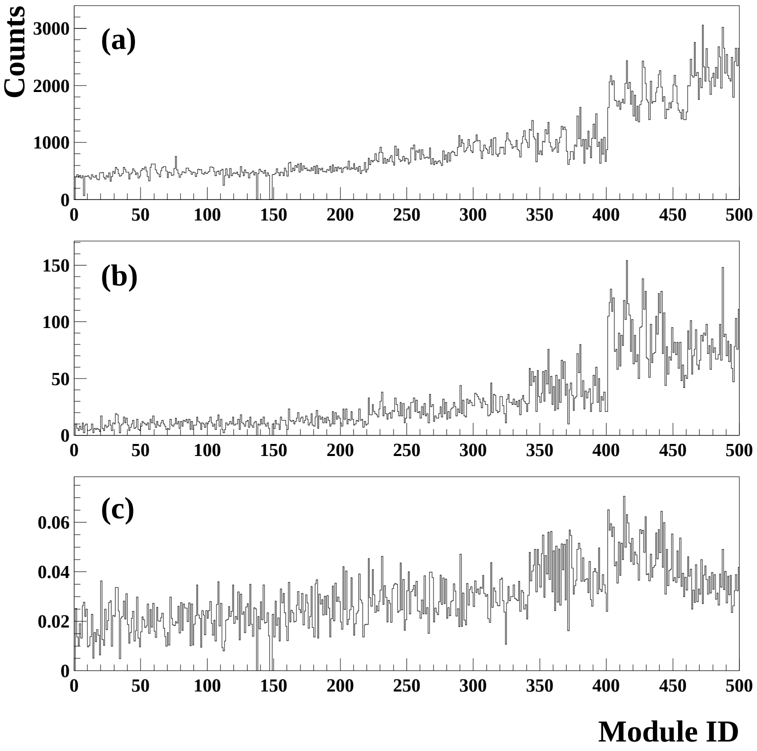

Figure 5.7: Multiplicity of every module (a) for identified π^+ and (b) for neighborings which have the same timing signal with any π^+'s. Probability is obtained in (c) by dividing (b) with (a).

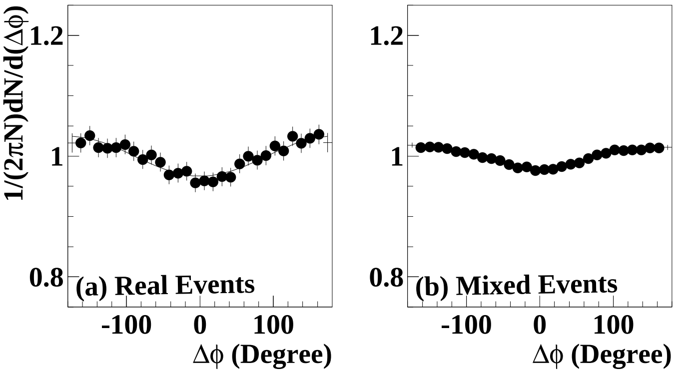

Figure 5.8: Relative azimuthal angle distribution of pions with respect to the Φ_0^{mix} is plotted for the central collisions (Class A). The left panel is the real data events and the right panel is mixed events when the probability of making the neighboring hit is 3.0 %.

5.5.3 Azimuthal Distribution of proton

The azimuthal distribution of protons with respect to the Φ_0 is also studied. The azimuthal angle of proton is needed to be rotated with the Φ_0 event by event. However, if it is done using the common Φ_0 defined from all of proton and fragments, like pion, the automatic correlation between protons and the Φ_0 must be involved due to the finite multiplicity of observed particles.

To remove this auto correlation, a new azimuthal angle of ${\Phi_0}^\mu$ is defined for each proton from the remaining particles in one event, for instance, for $\mu - th$ proton:

$$\begin{aligned} \mathbf{Q}^\mu \equiv [{P_x}^\mu, {P_y}^\mu] &= \sum_{\mu \neq \nu}^{M} [p_{t_\nu} cos\phi_\nu, p_{t_\nu} sin\phi_\nu] , \\ tan{\Phi_0}^\mu &= \frac{{P_y}^\mu}{{P_x}^\mu}. \end{aligned} \tag{5.6}$$

Then the distribution of the relative azimuthal angle with respect to ${\Phi_0}^\mu$, $\Delta\phi_\mu = \phi_\mu - {\Phi_0}^\mu$ is shown in Figure 5.9.

The azimuthal angle distribution is found to be anisotropic for all centralities and protons tends to be emitted into the same direction with other fragments, while pion are emitted into the opposite direction.

From these distributions, ${v_1}'$ is also defined by fitting with the function of equation 5.5.

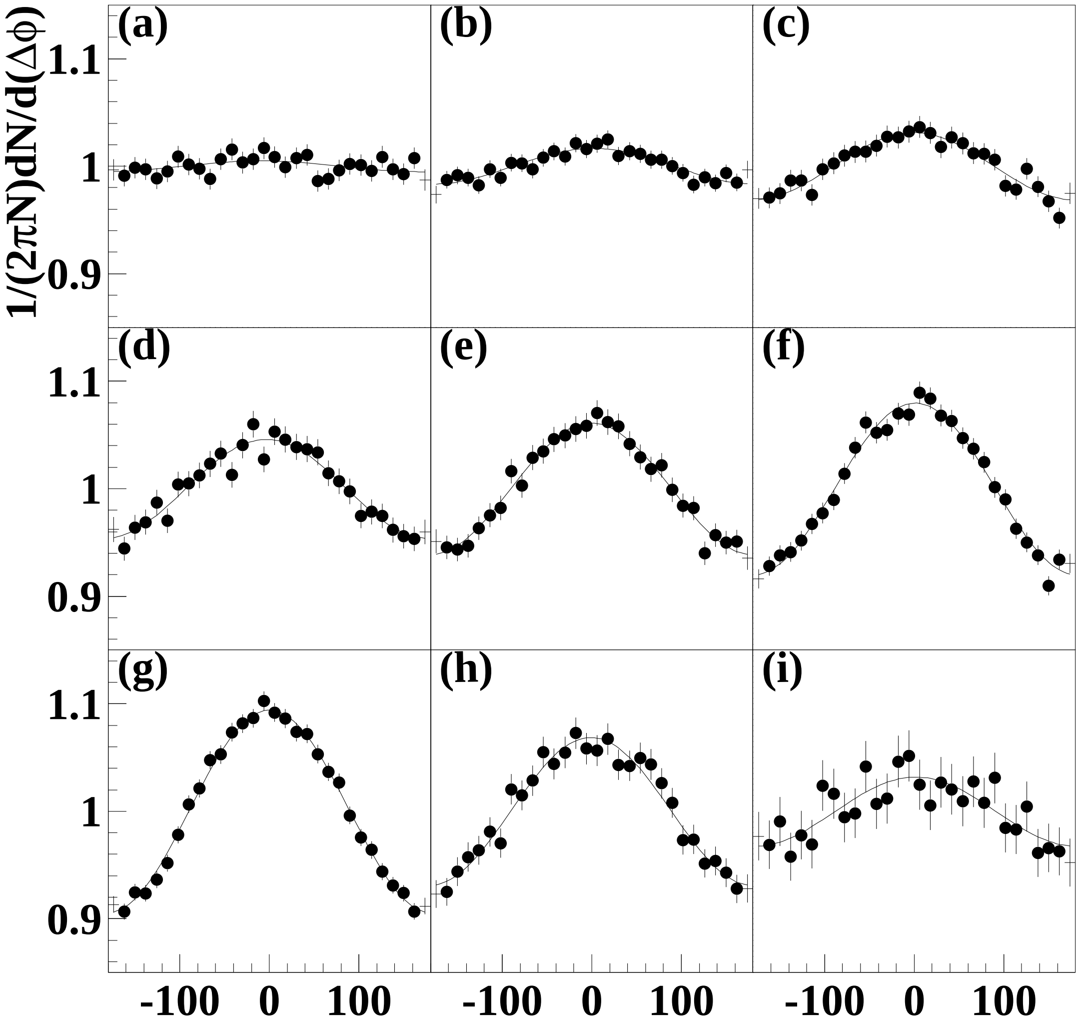

Figure 5.9: Azimuthal distribution of proton with respect to Φ_0

5.6 Resolution of Φ_0

As is discussed in the previous analysis, we observed anisotropy in the distribution of $\phi - \Phi_0$. The strength of anisotropy is quantified as v_1 using the function 5.5. Because of the finite multiplicity particle production and limit-ted detector acceptance, the Φ_0 is distorted from a real angle Φ_R which is the ideal origin. The observed v_1' is reduced from the "true" v_1. due to this experimental resolution, which has to be corrected. This correction factor is derived from the relation between v_1' and v_1:

$$\begin{aligned} v_1 &= \langle \cos(\phi - \Phi_R) \rangle && (5.7) \\ v_1' &= \langle \cos(\phi - \Phi_0) \rangle && (5.8) \\ &= \langle \cos[(\phi - \Phi_R) - (\Phi_0 - \Phi_R)] \rangle \\ &= \langle \cos(\phi - \Phi_R) \rangle \langle \cos(\Phi_0 - \Phi_R) \rangle - \langle \sin(\phi - \Phi_R) \rangle \langle \sin(\Phi_0 - \Phi_R) \rangle \\ &= v_1 \langle \cos(\Phi_0 - \Phi_R) \rangle \\ & && (5.9) \end{aligned}$$

where the $\langle \sin(\Phi_0 - \Phi_R) \rangle$ vanishes because of the symmetry distribution around $\Phi_R = 0$. Thus, the ${v_1}'$ has to be divided by the factor of $\langle \cos{(\Phi_0 - \Phi_R)} \rangle$. The method to estimate this resolution factor is introduced in the next section.

5.6.1 Estimation of Resolution of Φ_0

In this section, we discuss how to evaluate the resolution of Φ_0 in terms of $\langle cos\,(\Phi_0 - \Phi_R) \rangle$ This method is introduced by P.Danielewicz [17] and A.M. Poskanzer [45] in the earlier study.

Two Subevent Correlation

Previously, it is found that the two subevents created among protons and fragments in each event have a correlation as shown in the section 5.4.1

In the first method, the resolution can be estimated from the correlation between two subevents analytically.

$$\begin{aligned}\cos(\Phi_a - \Phi_b) &= \cos\{(\Phi_a - \Phi_R) - (\Phi_b - \Phi_R)\} \\ &= \cos(\Phi_a - \Phi_R)\cos(\Phi_b - \Phi_R) \\ &+ \sin(\Phi_a - \Phi_R)\sin(\Phi_b - \Phi_R) \qquad (5.10)\end{aligned}$$

Here, we take the average of events on the both sides and since the second term on the light side can be ignored,

$$\langle\cos(\Phi_a - \Phi_b)\rangle = \langle\cos(\Phi_a - \Phi_R)\rangle\langle\cos(\Phi_b - \Phi_R)\rangle. \qquad (5.11)$$

Since the subevent A and B are identical, this is definitely true that;

$$\langle\cos(\Phi_a - \Phi_R)\rangle = \langle\cos(\Phi_b - \Phi_R)\rangle \qquad (5.12)$$

Therefore,

$$\begin{aligned}\langle\cos(\Phi_a - \Phi_b)\rangle &= \langle\cos(\Phi_a - \Phi_R)\rangle^2 \\ \langle\cos(\Phi_a - \Phi_R)\rangle &= \sqrt{\langle\cos(\Phi_a - \Phi_b)\rangle} \qquad (5.13)\end{aligned}$$

This correction factor is the estimation only for the Φ_a which is defined from the half of statistics in one event, while the Φ_0 is defined from the full statistics. Hence, the resolution of Φ_0 is better than one of the Φ_a by a factor of $\sim \sqrt{2}$ because of double statistics. The details are described in reference [45] Finally, the resolution of Φ_0 is evaluated as $\langle\cos(\Phi_0 - \Phi_R)\rangle = 0.3770 \pm 0.0045$ at the mid-central (Class G:100 $< E_T <$ 200 GeV). In Table 5.2, the resolution factor is summarized for all centralities.

5.7 Corrections and Error Estimations

5.7.1 Systematic Error from Non-uniformity of Detector

The estimation of the systematic error caused by non-uniformity of the detector is carried out by analyzing the azimuthal uniformity of $\langle\cos(\Phi_a - \Phi_b)\rangle$.

E_T (GeV)	$\langle\cos(\Phi_0 - \Phi_R)\rangle$
420 ∼	0.1099 ± 0.0195
380 ∼ 420	0.1535 ± 0.0116
350 ∼ 380	0.2243 ± 0.0096
320 ∼ 350	0.2639 ± 0.0096
280 ∼ 320	0.3096 ± 0.0078
200 ∼ 280	0.3515 ± 0.0058
100 ∼ 200	0.3770 ± 0.0045
50 ∼ 100	0.3391 ± 0.0084
0 ∼ 50	0.2197 ± 0.0219

Table 5.2: Experimental resolution of Φ_0.

The $\langle\cos(\Phi_a - \Phi_b)\rangle$, which is calculated from the subevents correlation, is plotted as a function of the azimuthal angle in the laboratory frame in Figure 5.10(a) for the mid-central collisions. The mean of $\langle\cos(\Phi_a - \Phi_b)\rangle = 0.2569$ and the root mean square of 0.0149 is obtained as is shown in Figure 5.10(b). From the relation between $\langle\cos(\Phi_a - \Phi_b)\rangle$ and $\langle\cos(\Phi_0 - \Phi_R)\rangle$, The non-uniformity is estimated as 0.021. This factor is included in the systematic error.

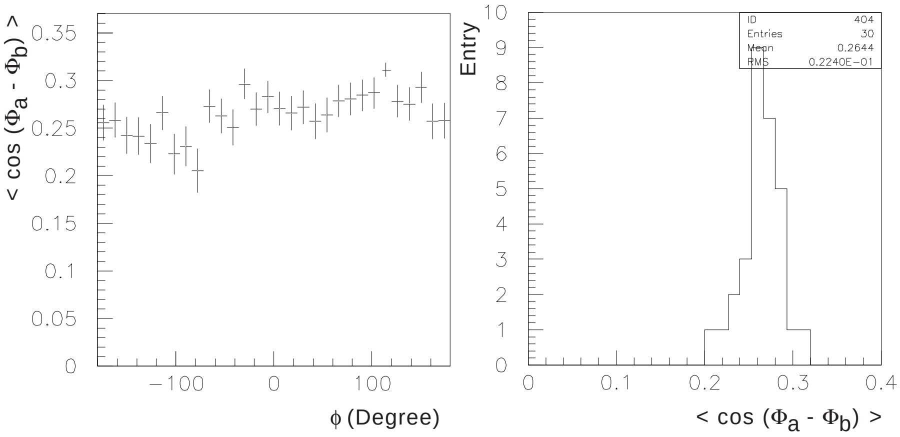

Figure 5.10: Correlation of two subevents, $\langle \cos(\Phi_a - \Phi_b) \rangle$ is plotted as a function of the azimuthal angle in the laboratory frame for the mid-central collisions (Class G).

5.7.2 Correction for Contamination

We mention about the background effect on this analysis. From the linearized spectrum. The pion contamination in proton spectrum is estimated to be about $6 \sim 24\%$ from the peripheral to the most central collisions. The effect of those pion contamination is estimated by an analytical calculation in a simulation.

In the simulation, we assume that protons and pions are emitted as 2 dimensional Gaussian on the transverse momentum plane with additional mean sift of the average momentum $\langle p_x \rangle$ in the axis-x to positive or negative, respectively, that is;

$$\frac{d^2N}{dp_x dp_y} = \exp\left(-\frac{(p_x \pm \langle p_x \rangle)^2}{2\sigma_{p_x}^2} - \frac{p_y^2}{2\sigma_{p_y}^2} \right), \tag{5.14}$$

where $\sigma_{p_x} (= \sigma_{p_y})$ is 215 MeV and 100 MeV for proton and pion, respectively in order to reproduce the observed transverse momentum distribution in our experiment.

Then we generate events from the above protons. Here, some of the protons are replaced artificially with pions by reproducing the contamination rate in the real events. The ratio of replaced proton is changed from 0 % to 25 % by 5 % step. Using those events, we followed the same manner which is applied for the real data. That means, we define the azimuthal angle of Φ_0 from the total transverse momentum of protons which include pion artificially, and the azimuthal distribution of other pions rotated by Φ_0 are calculated to obtain ${v_1}'$. Also the resolution of Φ_0 is evaluated from the correlation of two subevents to obtain v_1 by correcting v_1'. For example, the azimuthal distribution of pion with respect to Φ_0 is shown in Figure 5.11(a) when the contamination is 10 % and $\langle p_x \rangle$ of pion is -20 MeV. At this condition, v_1' of 0.049 ± 0.003 and $\langle \cos(\Phi_0 - \Phi_R) \rangle$ of 0.360 ± 0.001 are obtained. Thereby the corrected v_1 is obtained as 0.136 ± 0.007 from the relation, $v_1 = v_1' / \langle \cos(\Phi_0 - \Phi_R) \rangle$.

On the other hand, we can obtain the ideal v_1 value (v_{1R}) from the azimuthal distribution with respect to the Φ_R, since the Φ_R is fixed to $\Phi_R = 0^o$ in the simulation. In the Figure 5.11(b), the pion azimuthal distribution with respect to Φ_R is shown and v_{1R} of 0.134 ± 0.0025 is obtained. The agreement of those two v_1 prove accuracy of our analysis method.

In oder to estimate the systematic error of this analysis method and the effect of the pion contamination observed in real data, this study is performed under the condition of the different contamination rate and the different average momentum shift. The ratio of the contamination is changed from 0 % to 25 % for the pion's average momentum shift, $\langle p_x \rangle$ of -5, -20 and -50 MeV. The v_1 obtained by following the experimental analysis method are plotted in Figure 5.12 when $\langle p_x \rangle$ is -5, -20 and -50 MeV from the top and the solid lines indicates v_{1R}. It tells us this method is not affected by the ratio of the contamination and also the degree of v_1 for pions. The discrepancy of v_1 from v_{1R} is less than 2 % for any conditions. This value is included in the systematic error.

This simulation is performed also for the analysis of protons. In this case, we found that the corrected v_1 become smaller than the ideal v_{1R} with increasing the the ratio of contamination systematically. The discrepancy of the v_1 from v_{1R} also depends on the azimuthal anisotropy of pions, even pions can be corrected properly. However, we obtained the anisotropy of pions and estimated the pion contamination, we can estimate v_{1R} by using the simulation. The anisotropy of pion is reproduced in each centrality by shifting the mean transverse momentum to negative p_x. Those pions are mixed artificially in generated protons with the measured ratio. Under this condition, the anisotropy of protons are modulated to reproduce the real data by changing $\langle p_x \rangle$. After removing pion contamination from this proton sample, the v_{1R} is estimated.

The errors propagated via statistics, background, non-uniformity are summarized in the Table 5.3.

Type of Error	Error [%]
Statistical	0.4
Uniformity	2.1
Background	2

Table 5.3: The estimated errors are summarized

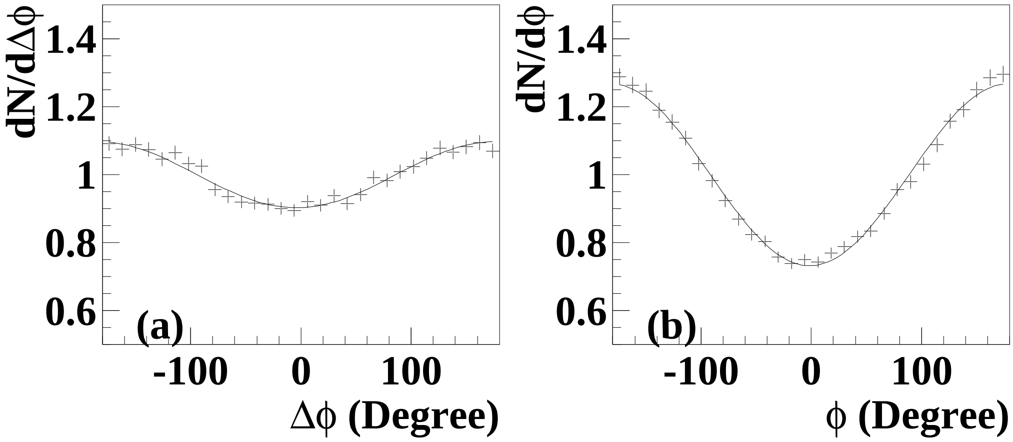

Figure 5.11: The azimuthal distribution of pion with respect to Φ_0 when the contamination is 10 % and $\langle p_x \rangle$ is -20 MeV.

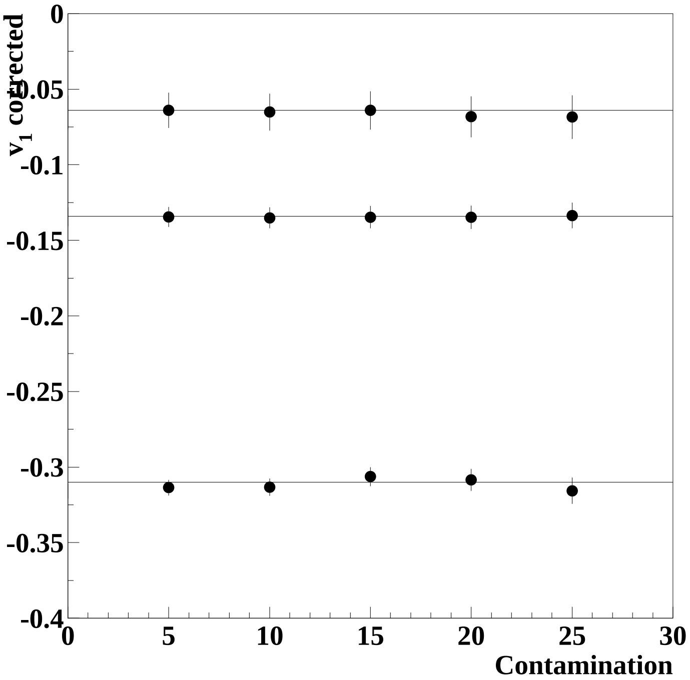

Figure 5.12: The v_1 obtained by the following experimental analysis method against for the various contamination

Finally, the ${v_1}'$ and corrected v_1 are listed for each centrality in Table 5.4, 5.5 for protons and pions, respectively.

E_T [GeV]	proton	
	${v_1}'$	v_1
420 ~	0.0029 ± 0.0013	0.0167 ± 0.0214
380 ~ 420	0.0081 ± 0.0011	0.0276 ± 0.0164
350 ~ 380	0.0168 ± 0.0013	0.0639 ± 0.0134
320 ~ 350	0.0263 ± 0.0015	0.113 ± 0.0138
280 ~ 320	0.0332 ± 0.0014	0.119 ± 0.0123
200 ~ 280	0.0453 ± 0.0013	0.133 ± 0.0112
100 ~ 200	0.0566 ± 0.0011	0.149 ± 0.0108
50 ~ 100	0.0468 ± 0.0020	0.121 ± 0.0124
0 ~ 50	0.0259 ± 0.0356	0.0823 ± 0.0252

Table 5.4: ${v_1}'$ and v_1 obtained from proton

E_T [GeV]	pion	
	${v_1}'$	v_1
420 ~	-0.0137 ± 0.0019	-0.0259 ± 0.0231
380 ~ 420	-0.0170 ± 0.0016	-0.0468 ± 0.0163
350 ~ 380	-0.0204 ± 0.0020	-0.0454 ± 0.0131
320 ~ 350	-0.0319 ± 0.0025	-0.0688 ± 0.0145
280 ~ 320	-0.0317 ± 0.0025	-0.0669 ± 0.0123
200 ~ 280	-0.0403 ± 0.0024	-0.0867 ± 0.0115
100 ~ 200	-0.0634 ± 0.0025	-0.1405 ± 0.0140
50 ~ 100	-0.0777 ± 0.0056	-0.1869 ± 0.0267
0 ~ 50	-0.0846 ± 0.0121	-0.3243 ± 0.0835

Table 5.5: ${v_1}'$ and v_1 obtained from π

5.8 Centrality Dependence

We have evaluated the azimuthal anisotropy of protons and pions with respect to Φ_R in terms of v_1 for each centrality. Now the v_1 of proton and pion are plotted as a function of the transverse energy, E_T measured by MIRAC in Figure 5.13 after the corrections with the systematic error included in the errors. It turns out that the both of species strongly depend on the centrality. The magnitude of v_1 for protons increases with decreasing E_T and reach at maximum point at mid-central collisions, where the impact parameter is ~ 8 fm then decline to peripheral. For the pion, the off set of v_1 is negative and it's magnitude furthermore decrease with increasing with E_T monotonically. The absolute value of v_1 is the comparable order each other.

5.9 Rapidity Dependence

5.9.1 Transverse Momentum Dependence of v_1

The azimuthal asymmetric event shape is found in the azimuthal distribution of protons and pions, then it is quantified with the v_1 in full acceptance of the Plastic Ball at the previous section. In addition to this, v_1 is expanded with the transverse momentum, p_T, and the rapidity. In Figure 5.14, v_1 of proton is displayed as a function of p_T in 4 intervals of rapidity bins at the mid-central collisions (Class G:$100 < E_T < 200$ GeV) where the maximum v_1 is observed. It is found that v_1 depends on p_T and rises linearly with increasing p_T.

5.9.2 Average Transverse Momentum Transfer

The average transverse momentum projected on the direction of Φ_0 $\langle p_x \rangle$, is evaluated as a function of the rapidity for protons and pions. This is done for semi-central collisions ($100 < E_T < 200$GeV) where the largest azimuthal anisotropy is observed for protons (See Figure 5.13). The distribution of $d^3N/dydp'_xdp'_y$ is constructed for protons and pions as shown in Figure 5.15,

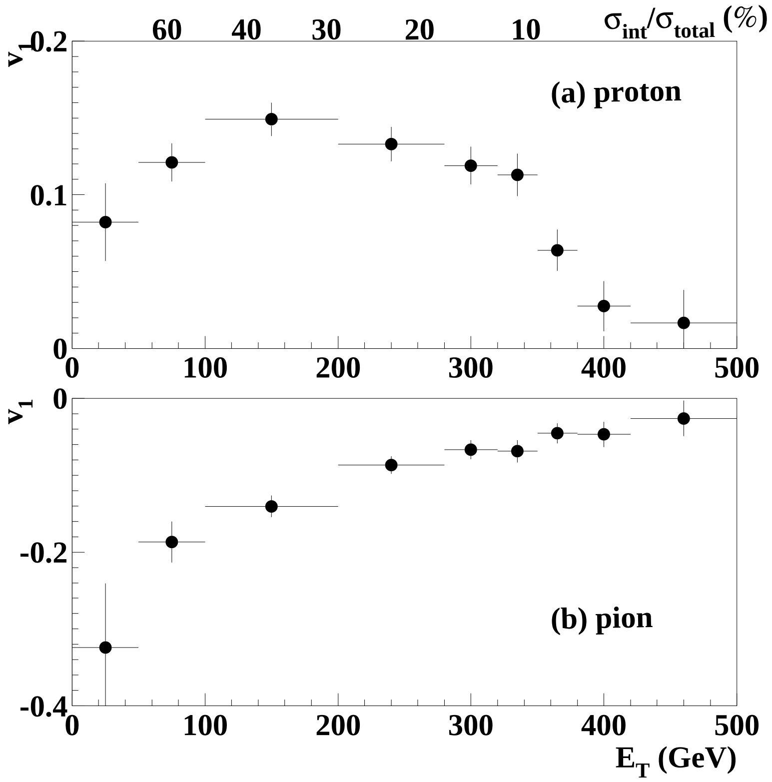

Figure 5.13: Centrality dependence of v_1. Upper shows for protons and lower shows for pions.

where new axis is determined as

$$\begin{aligned} p'_x &= p_T \cos(\phi - \Phi_0) \\ p'_y &= p_T \sin(\phi - \Phi_0) . \end{aligned} \tag{5.15}$$

At each rapidity, the $\langle p'_x \rangle$, is calculated from the fits to the experimental distribution by using the Gaussian distribution:

$$\frac{d^3N}{dy dp'_x dp'_y} = \exp\left(-\frac{(p'_x - \langle p'_x \rangle)^2}{2\sigma^2_{p_x}} - \frac{{p'_y}^2}{2\sigma^2_{p_y}} \right) , \tag{5.16}$$

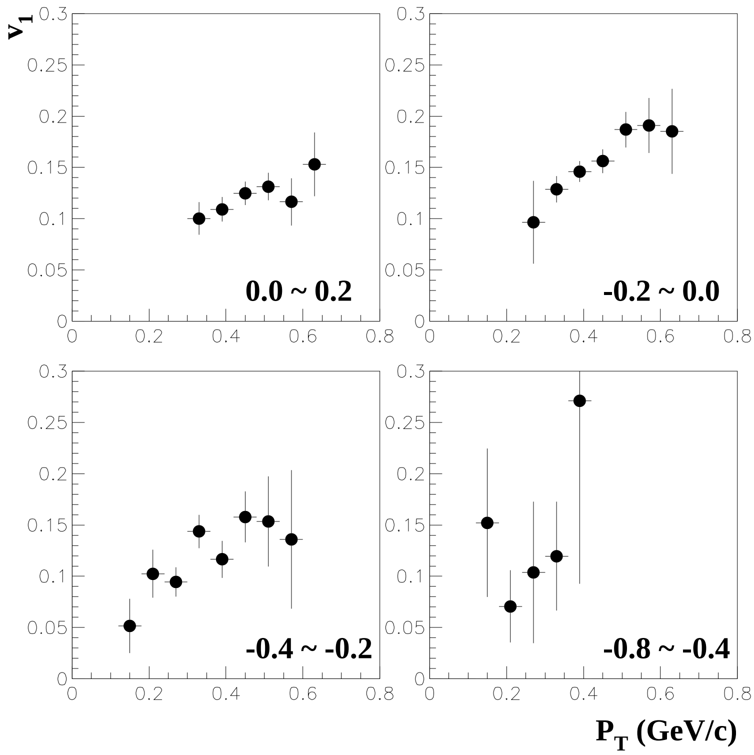

Figure 5.14: Transverse momentum dependence of v_1 for 4 rapidity bins at the mid-central collisions (Class G).

The fitting is done with reasonable χ^2. The $\langle p'_x \rangle$ is corrected by the resolution factor of the $\langle \cos(\Delta\Phi_0) \rangle$. After correction, $\langle p_x \rangle$ for protons and pions are plotted as a function of the rapidity in Figure 5.16.

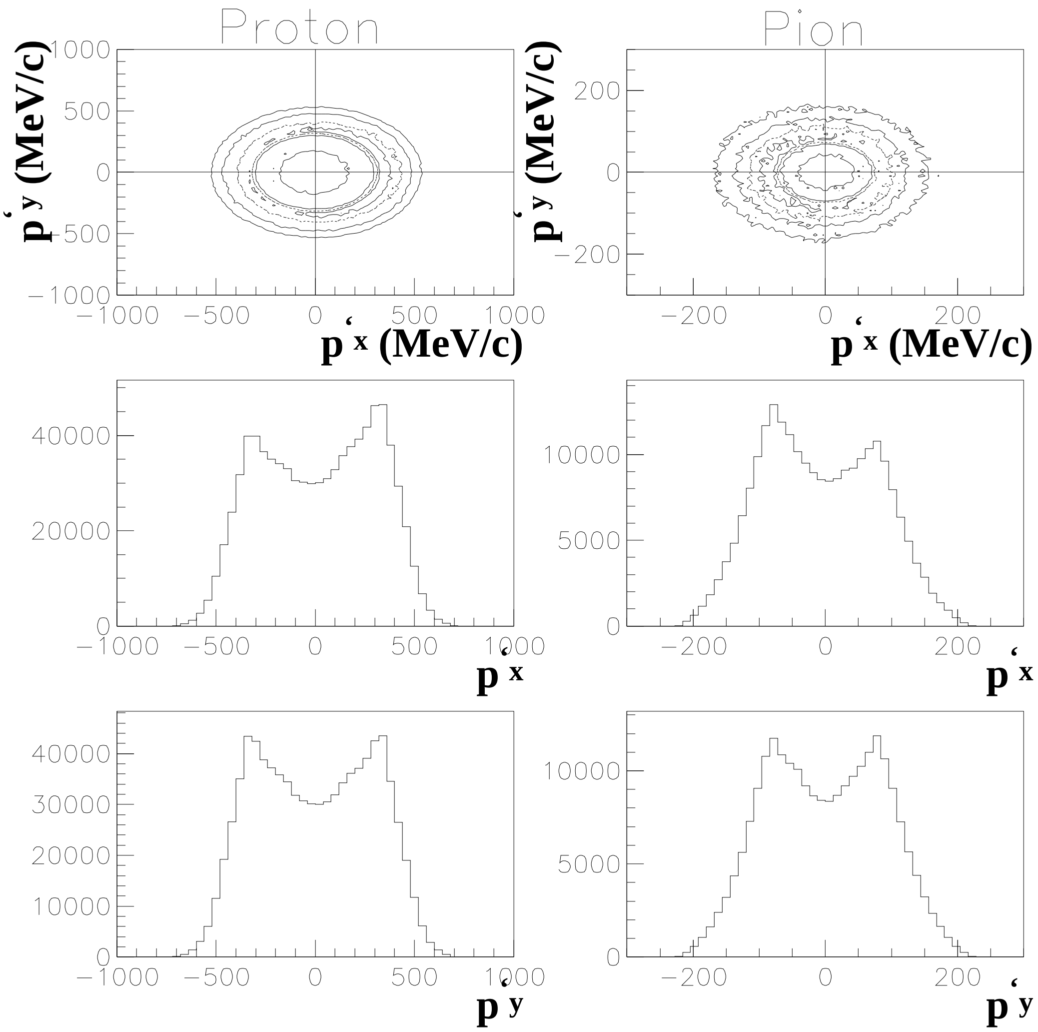

Figure 5.15: Distributions of transverse momentum projected on the direction of Φ_0. The left half shows protons and the right half shows pions.

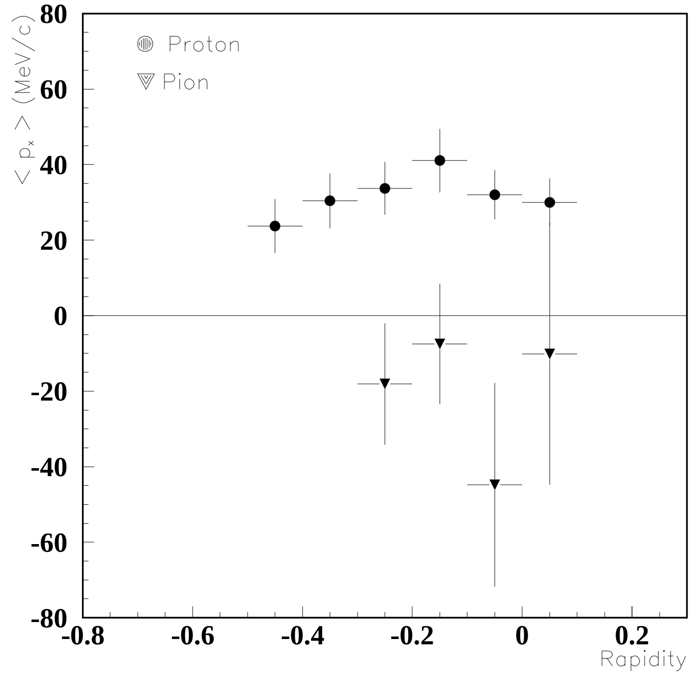

Figure 5.16: Distribution of $\langle p_x \rangle$ as a function of the rapidity. Closed circles show protons and closed triangles show pions.

Chapter 6

Discussion and Comparison with Theoretical Models

In this experiment, it is found that protons are emitted to the same direction of the Φ_0, while pions are emitted to the opposite direction of the Φ_0 at the target rapidity region. Understanding the mechanism of this feature might be a key issue to investigate the meaning of the Φ_0.

We consider what kind of processes produces azimuthal anisotropy of particle emission at target rapidity. There are several approaches to describe particle production in high energy heavy ion collisions. In this thesis, applying a simple nuclear collision model, based on the participant-spectator model, we discuss how to understand our experimental observables. In this simple model, we consider the effect of several interaction processes in the target spectator matter on the anisotropic particle emission pattern. Because the Plastic Ball detector locates at the target rapidity region, particles detected by this detector are influenced by the target spectator matter. We estimate how much effects are produced by ordinary hadronic interactions in the spectator matter. Finally, we introduce RQMD model for the comparison and for the interpretation of the experimental observables.

6.1 Geometrical Features of Collisions

In the model calculation, we assume the geometrical participant-spectator model in which the spectator and the participant regions are well separated by the geometry. In another word, the geometrical shape of the target spectator is uniquely defined for a given impact parameter as is schetched in Figure 6.1 in the beam view. The hatched region indicates the participant and the shaded region presents the target spectator and the region surround by the broken line signifies the target spectator.

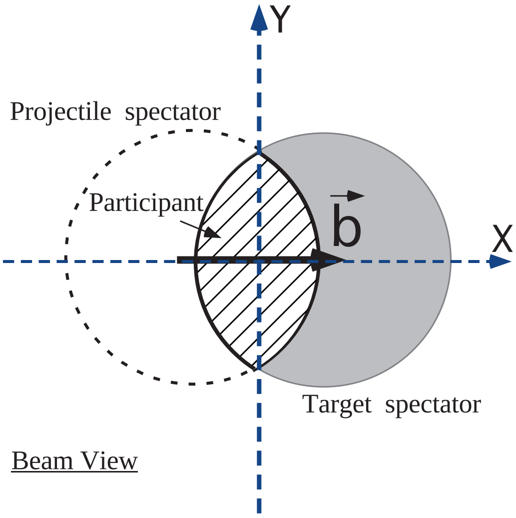

Figure 6.1: Schematic picture of colliding nuclei in the beam view. The hatched region indicates the participant and the shaded region presents the target spectator and the region surround by the broken line signifies the target spectator.

This assumption is supported experimentally by a comparison between a geometrical calculation and observed differential cross sections with ZDC. The number of nucleons in the spectator is evaluated from the energy measured by ZDC:

$$N_{spec}^{ZDC} = \frac{E_{ZDC}[\mathrm{GeV}]}{\sqrt{158^2 + 0.98^2}[\mathrm{GeV}]} \tag{6.1}$$

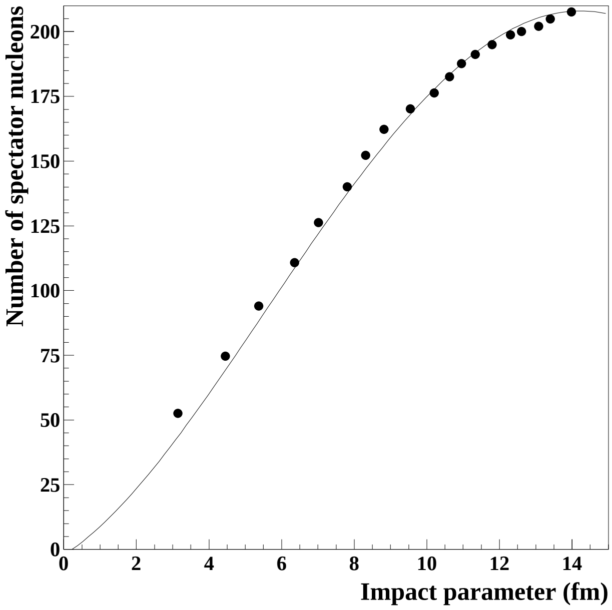

Figure 6.2: Number of nucleons in projectile spectator as a function of impact parameter. The closed circles indicate the data evaluated from measurement by ZDC. The solid line is obtained from geometrical calculation of colliding nuclei.

where E_{ZDC} is the energy observed in ZDC, which is divided by the total energy per nucleon of the beam. Obtained values are plotted in Figure 6.2 as a function of the impact parameter which is calculated from the cross section at each bin of E_{ZDC}. The solid curve in the figure shows the estimation of this number from the geometrical calculation of the spectator region by assuming the normal nuclear density. The measurement agrees well at the impact parameter more than 4 fm. The small discrepancy at $b < 4$ fm might be due to less density at the surface of Pb nucleus, where the sharp cut off picture does not hold well.

This result is suggesting that the geometry of the spectator can be determined by the geometrical participant-spectator model which assume clear cut separation.

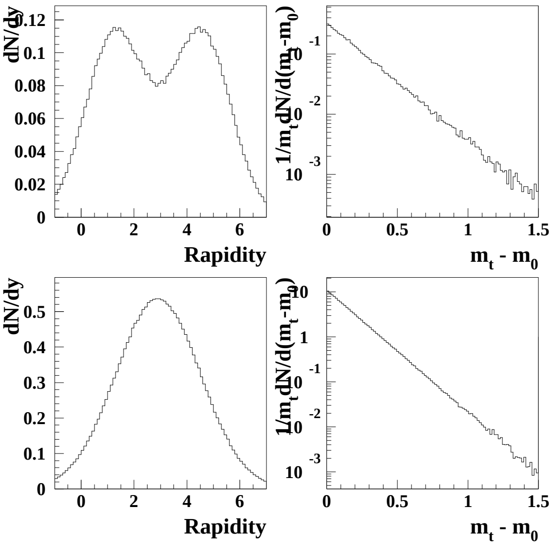

Figure 6.3: Parameterized distributions of dN/dy and $1/m_T dN/d(m_T - m_0)$ for model calculation. Uppers are for proton and lowers are for pion.

6.2 Simple Models

There are several processes which may produce an anisotropic particle emission. In this model calculation, four effects listed below are discussed. Strength of the following effects are evaluated one by one in the model calculations of mode I $\sim$ IV.

1. statistical fluctuation
2. absorption by the target spectator
3. elastic scattering with the nucleons in the target spectator
4. resonance from pions with nucleons in the target spectator

First we check whether it is simply caused by the statistical fluctuation (Mode I). Since the multiplicity of proton and fragments observed in the Plastic

Ball is about ~ 8 in average, it is required to investigate the effect of the statistical fluctuation on the azimuthal distribution. Secondly, we consider three interaction processes in the target spectator which may produce the azimuthal anisotropy of protons and pions (Mode II $\sim$ Mode IV). The mean free path of those particles in the normal nuclear density are expected to be smaller than the radius of the lead target, ($R \sim$ 7.2fm), for instance, $\lambda_p \simeq 3 \sim 6$ fm and $\lambda_\pi \simeq 2 \sim 5$ fm are estimated from the cross section of $p+p$ and $\pi+p$ [46] for proton and pion in the energy range detected by the Plastic Ball.

Assuming the geometrical features of collisions, pions and protons are generated from the participant region (hatched region in Figure 6.1). To simulate realistic, transverse momentum and rapidity distribution of protons/pions are parameterized with the double/single Gaussian function and a single exponential function, respectively (See Figure 6.3). The particles are randomly generated in the azimuthal direction. In each model of calculation (mode I $\sim$ IV), interaction process of those generated particles in the spectator are taken into account. In the model calculations of mode II $\sim$ IV, it is assumed that the density of the target spectator is equivalent to the normal nuclear density, i.e., $\rho = 0.16\text{fm}^{-3}$ and the cross sections of p + p and p + π are 12.5mb. Finally, azimuthal angle distributions are studied for particles within the Plastic Ball acceptance.

6.2.1 Mode I: Statistical Fluctuation

It is an important question how much the azimuthal anisotropy is produced simply due to statistical fluctuation under the multiplicity in study. To evaluate this effect, particles are generated randomly simulating the observed charged multiplicity distribution in Pb + Pb collisions. Although the geometrical frame of the model is adopted in this mode of calculation, no interaction of produced particles is included; only the statistical fluctuation is taken into account. Particles which get into the Plastic Ball acceptance are collected. The multiplicity distribution reproduces the measurement well as shown in left panel of Figure 6.4.

For those particles, the subevent analysis is performed using the same code for the real data; each event is randomly divided into two equal size subevents then the azimuthal angle of total transverse momentum is evaluated in each subevent. The relative angle distribution, $\Phi_a - \Phi_b$, is shown in the right panel of Figure 6.4. Distribution is flat within statistical error. To confirm the flatness of the distribution, A_1 parameter of Equation 5.4 is obtained for various multiplicity events as is shown in Figure 6.5. They are consistently zero within the error at the whole range of multiplicities.

Therefore, we conclude that the statistical fluctuation alone with the current analysis method can not be responsible for the anisotropic event shape as observed in the real data. Now we consider effects of rescattering with nucleons in the target spectator in the following sections.

6.2.2 Mode II: Absorption by the Spectator

In this mode of calculation, we simulate how the azimuthal anisotropy would be created if pions and protons are absorbed by the target spectator. The protons and pions are emitted from the participant region with the same manner as discussed previously. As schematic picture is shown in Figure 6.6, we consider that some of particles penetrate the target spectator on the way out, but some of particles might be absorbed inside the matter. Survival probability, P is introduced in the simulation by assuming the certain mean free path,λ, and path length L, in the matter:

$$P = \exp\left(\frac{-L}{\lambda}\right), \tag{6.2}$$

where λ is assumed by the normal nuclear density of $0.16\mathrm{fm}^{-3}$ and the cross section of 12.5mb for both pions and protons. The pions and protons are emitted with the same manner as discussed previously. The geometry of the spectator matter is uniquely defined for a given impact parameter and the direction of the impact parameter vector is fixed to the positive x-axis as is shown in Figure 6.6. Then the survival probability and the acceptance

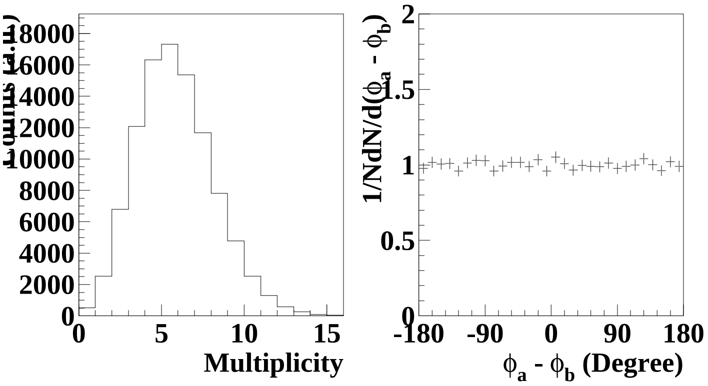

Figure 6.4: Multiplicity distribution (left) and the relative angle distribution (right)

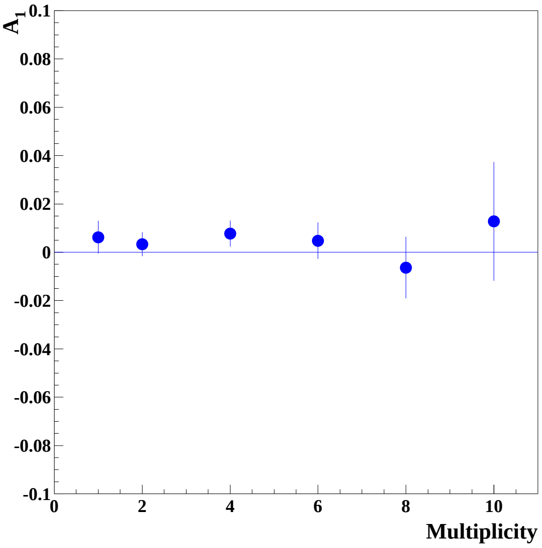

Figure 6.5: Multiplicity dependence of the strength of azimuthal anisotropy between two subevents, A_1.

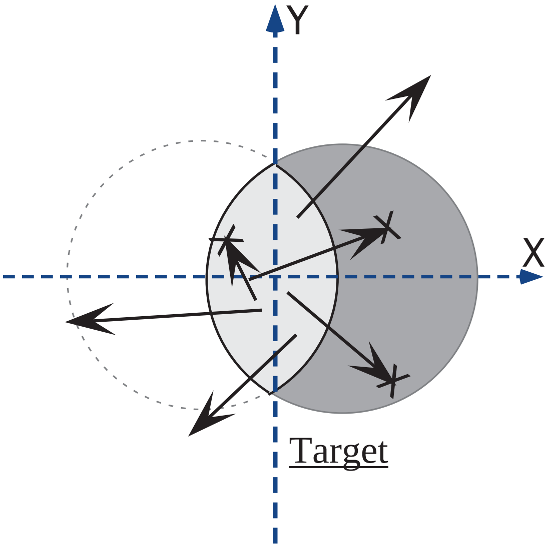

Figure 6.6: Schematic picture of absorption process (Mode II)

of the Plastic Ball are considered. The average of survival probabilities as a function of the azimuthal angle is shown in Figure 6.7 for pion at $b = 8$fm and $\lambda = 5$fm Clear absorption by the target spectator sitting at around $\phi = 0^o$ is seen; the survival probability is minimum around at zero degree where the thickness of the target spectator is largest.

In Figure 6.8, the azimuthal distributions for both of protons and pions are calculated at the Plastic Ball acceptance, Azimuthal angle distributions at the impact parameter of 2, 4, 8 and 12 fm are shown from the top to the bottom. The results show that the azimuthal anisotropic emission is visible with less particles emission on the side of the target spectator for both protons and pions. And the anisotropy becomes larger with increasing impact parameter for both species. The strength of the anisotropy, v_1 is quantified by fitting with the Equation 5.5. The v_1 is plotted as a function of E_T in Figure 6.13 and Figure 6.14 for proton and pion, respectively. The closed squares show the results of this model calculation and the experimental data are also shown with the closed circles for the comparison. The corresponding

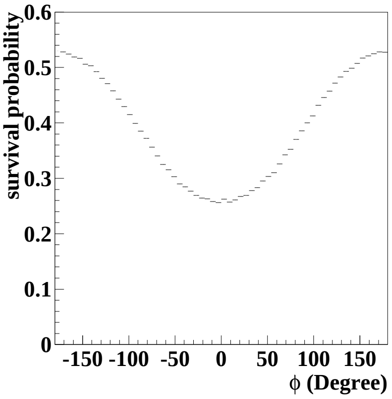

Figure 6.7: Survival probability as a function of the azimuthal angle for pion at $b = 8$fm and $\lambda = 5$fm. Clear absorption by the target spectator, sitting at around $\phi = 0^o$ is seen.

impact parameter value is shown on the top of these figures. In the experimental data, the sign of proton's v_1 is always positive, because protons tend to be emitted to the same direction of Φ_0. We apply this definition for the results of model calculation to compare with the data. The results show that v_1 of protons increase with increasing the impact parameter. This model calculation overestimates the data. On the other hand, v_1 of pions indicates positive sign, while the data show negative value. Therefore, this scenario totally fails to explain the data.

Considering the energies of pions and protons observed with the Plastic Ball, complete absorption is a reasonable assumption for pions but for protons, elastic scattering is more realistic. In the next section, proton-nucleon scattering process in the spectator are taken into account instead of complete absorption for protons.

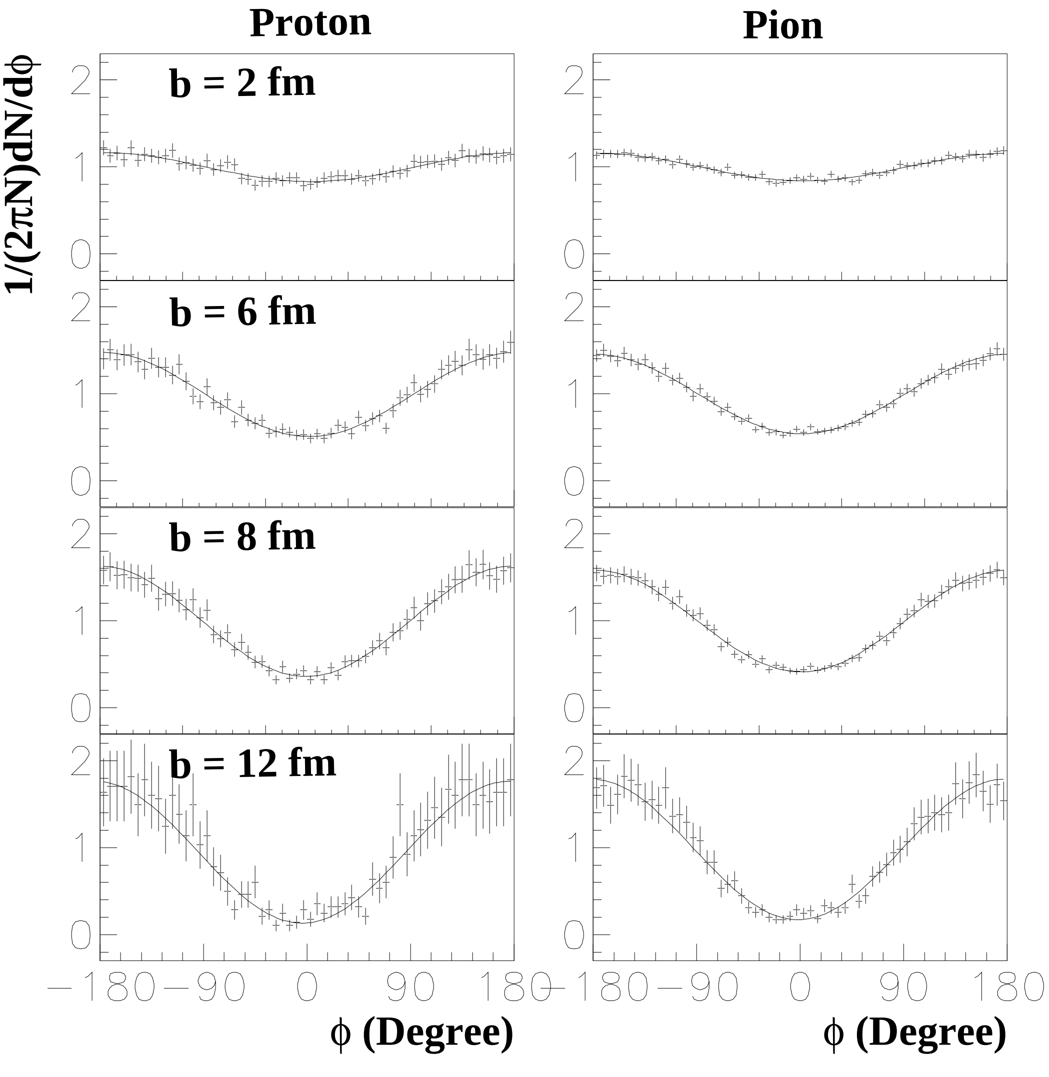

Figure 6.8: Azimuthal distributions simulated in the absorption mode (Mode II). Acceptance filter of the Plastic Ball is required. Left panels are for protons and right panels are for pions. Each corresponds to impact parameter of 2, 6, 8 and 12 fm from the top the bottom. Solid lines indicate the fitting results with Equation 5.5.

6.2.3 Mode III: Rescattering of Proton with Nucleon

In this mode of calculation, we replace the complete absorption to rescattering process in the target spectator for protons. In this calculation, elastic scattering of proton + nucleon is considered. Scattered two protons share the kinetic energy and there is a chance to have both protons in the Plastic Ball acceptance (See Figure 6.9). The probabilities of the rescattering are evaluated from the path length and the cross section of 12.5 mb in the normal nuclear density. The scattering angle and the momentum transfer are calculated according to the initial momentum of the incident proton and the Fermi momentum of nucleons in the spectator, where normal nuclear density is assumed. Angular differential cross sections are also taken into account [47, 48]. For simplicity, we assume that the rescattering is taken place only once for each generated proton.

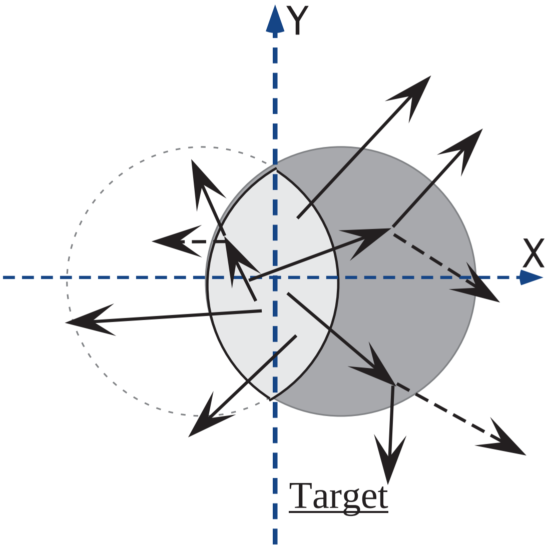

Figure 6.9: Schematic picture of rescattering process for proton (Mode III)

Similarly, protons within the Plastic Ball acceptance are collected. The azimuthal distribution of protons are plotted in the left panel of Figure 6.10, where the impact parameter is at 2, 6, 8 and 12 fm from the top to the bottom. It is found that the anisotropy is small but the peak position is shifted from 180 degree to 0 degree. For pions, the results of absorption model calculation are replotted in the right panel of Figure 6.10 since this rescattering process does not affect on pions. For the comparison with the data, the v_1 is obtained for both protons and pions by fitting with the Equation 5.5 and plotted in the Figure 6.13 and Figure 6.14 with closed triangles. Those figures show v_1 of protons is smaller than data and it does not change within the error even if the cross section is increased to 20 mb. However, v_1 of pions show up in the negative direction. The centrality dependence of pions shows monotonic decrease with increasing the impact parameter. This tendency is consistent with our observation. However, the complete absorption of pions seems to be too strong. Thus, we consider another process concerning the pions.

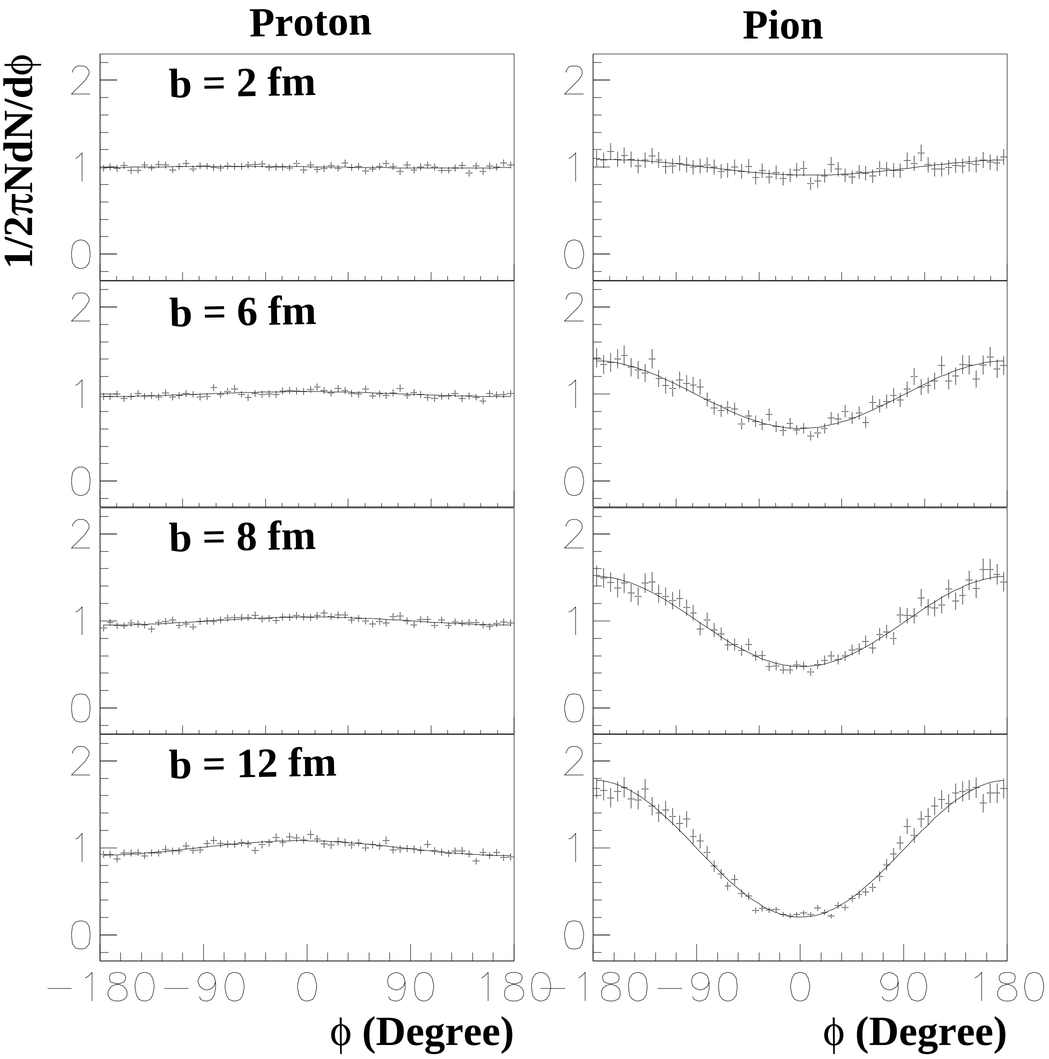

Figure 6.10: Azimuthal distributions simulated in the rescattering mode for protons (Mode III). Left panels are for protons and right panels are for pions. For pions, the results obtained by the absorption mode (Mode II) are replotted. Each distribution corresponds to the impact parameter of 2, 6, 8 and 12 fm from the top to the bottom. Solid line indicates the fitting results with Equation 5.5.

6.2.4 Mode IV: Resonances from π + nucleon

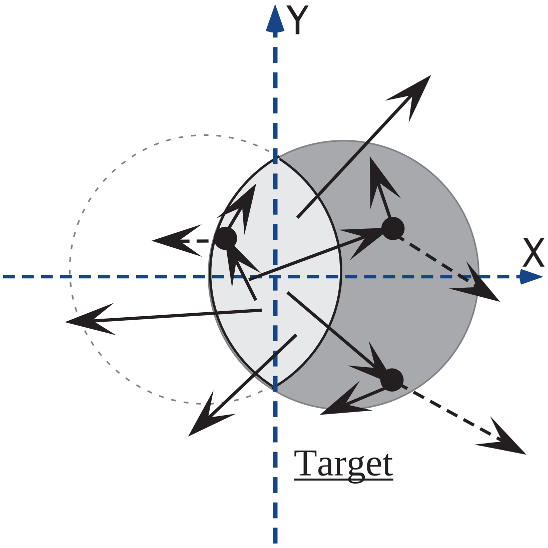

Figure 6.11: Schematic picture of resonance process (Mode IV)

Another important process which differentiates the behavior of pion and proton is the process via resonance production of pions [49, 50, 51] such as,

$$\begin{aligned} \pi^+ + p \to & \quad \Delta^{++} & \to \pi^+ + p \\ \pi^+ + n \to & \quad \Delta^{+} & \to \pi^0 + p. \end{aligned}$$

In the first process, one proton is scattered by a pion and in the second one, one pion is absorbed and one proton comes out. Since the total cross section of pions at this energy, production of Δ resonance is dominant process. This Δ production might make anisotropy of pion weaker compared to the absorption process and enhance anisotropy of protons. When the resonances decay into proton and pion, this proton carries most of the momentum, because of the larger mass of protons. We expect pions emitted to the target spectator may produce more resonances, then those resonances emit additional protons to the direction of the target spectator.

In this mode of calculation, pions produce resonances with nucleons which have Fermi momentum in the normal nuclear density. With a certain probability estimated from the path length and the cross section of 12.5 mb, those resonances are assumed to decay into the original pair of π^+ and nucleon. Hence pion absorptions are excluded from this calculation.

The azimuthal distributions of the particles accepted by the Plastic Ball are shown in Figure 6.12 for proton and pion on the left and right side for the impact parameters of 2, 6, 8 and 10 fm from the top to the bottom, respectively. It becomes clearer that the enhancement of protons at 0 degree and the opposite tendency for pions. The v_1 obtained from those distributions are plotted in Figure 6.13 and Figure 6.14 with the closed inverted triangles. The v_1 of protons become close to data, however still underestimate. For pions, the centrality dependence of v_1 is similarly decrease with increasing the impact parameter. In this case, however, the absolute value is smaller than the data with a factor of a half even if the cross section is increased to 20 mb. In this calculation, the anti-correlations of protons and pions are also reproduced.

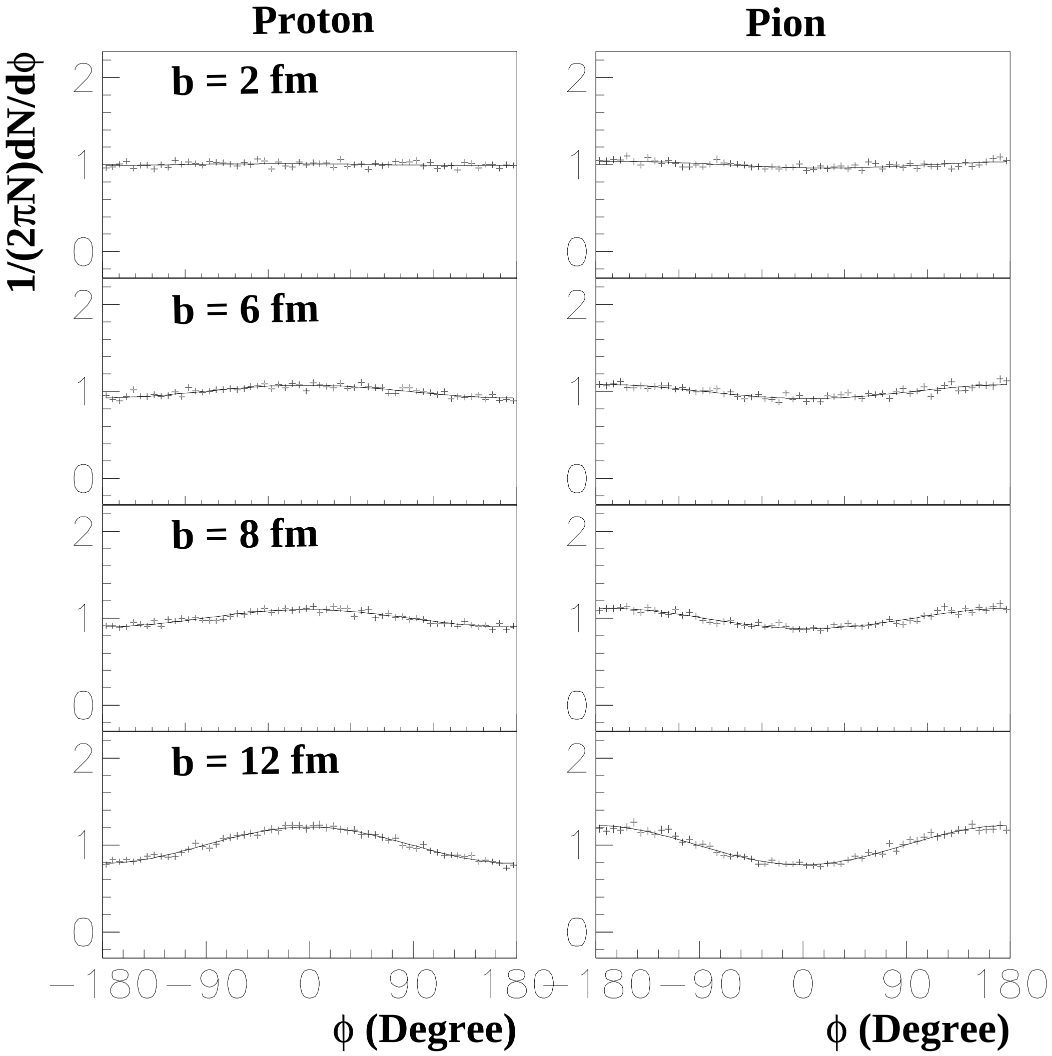

Figure 6.12: Azimuthal distributions simulated in the resonance of pions (Mode IV). Left panels are for protons and right panels are for pions. Each corresponds to impact parameter of 2, 6, 8 and 12 fm from the top the bottom. Solid lines indicate the fitting results with Equation 5.5.

6.2.5 Summary of Simple Model: Mode I to IV

We summarize the results obtained from the simple models in the mode I to IV.

- **Mode I : Statistical fluctuation**

    - The flat distributions are observed in whole multiplicity region.

  It confirms that the statistical fluctuation can not be responsible for the anisotropic event shape.

- **Mode II : Absorption by the target spectator**
  anisotropy

    - proton: enhanced at $\phi = 180^o$
    - pion: enhanced at $\phi = 180^o$

  centrality dependence of v_1

    - proton: gradually increase with increasing the impact parameter. larger than the data (a factor 2).
    - pion: the positive v_1 is found.

  This model calculation fails to explain the anti-correlation of protons and pions.

- **Mode III: Rescattering of proton with nucleon (Absorption for pion)**
  anisotropy

    - proton: enhanced at $\phi = 0^o$
    - pion: enhanced at $\phi = 180^o$

  centrality dependence of v_1

  - proton: gradually increase with increasing the impact parameter. smaller than data (a factor 1/7).
  - pion: the negative v_1 is found.
    monotonically decrease with increasing the impact parameter.
    larger than data (a factor 2).

  This mode of calculation explains the data, semi-qualitatively.

- **Mode IV: Resonance from pions with nucleon**
  anisotropy

  - proton: enhanced at $\phi = 0^o$
  - pion: enhanced at $\phi = 180^o$

  centrality dependence of v_1

  - proton: gradually increase with increasing the impact parameter. smaller than data (a factor 1/3).
  - pions: the negative v_1 is found.
    monotonically decrease with increasing the impact parameter.
    smaller than data (a factor 1/2).

  This mode of calculation explains the data, semi-qualitatively.

The all of interaction processes of Mode II $\sim$ IV produce the azimuthal anisotropic distributions for protons and pions. The calculations of mode III and IV explain the anti-correlation of protons and pions observed in the data. In both of cases, the protons are emitted to the $\phi = 0^o$, which is the direction of the target spectator sitting. Those features are understood as the following: the pions are likely to be reduced by the spectator. On the other hand, the protons are likely to be enhanced to the target spectator direction, because of additional protons from the target spectator.

Whenever the anti-correlation of protons and pions is observed, the emitted direction of protons are face to the direction of the target spectator which is the direction of the impact parameter vector.

The absolute v_1's disagree for proton and pion. For pions, the calculation of the complete absorption overestimate the data, while that of the full resonance mode underestimate the data. Those discrepancies might be due to the following reason. The reality may be between the both of mode III and mode IV. If we consider the secondary collisions of the resonances with nucleons in the spectator, pion absorption might be occurred.

$$\pi^+ + p \rightarrow \Delta^{++} \tag{6.3}$$

$$\Delta^{++} + n \rightarrow p + p \tag{6.4}$$

In the case of that 50 % of pions are absorbed and the rest are survived through this resonance process, the agreement becomes better as shown with open squares in Figure 6.14. It is suggesting that the secondary interaction process should be taken into account.

For the proton, the tendency of the centrality dependence is not reproduced. The model calculation show anisotropy becomes larger towards the peripheral collisions, while the data reached at the maximum at around $b = 8$ fm. This disagreement might be due to the following reasons: In the calculation, we do not take into account the secondary collisions which is expected to be more effective in the peripheral collisions. It is also suggesting that we need to take into account secondary cascade collisions. Another one is that we assumed the isotropic emission from the participant region. It might be not true. Concerning this issue, it is briefly discussed in Appendix B.2.

6.2.6 Conclusion of Simple Model

From those model calculations, it is found that the azimuthal anisotropy of emissions observed in protons and pions are explained by the interactions with nucleons in the spectator, semiquantitatively. Protons are enhanced at the direction of the target spectator, while pions are reduced. Consequently, it is confirmed that the azimuthal direction of protons at the target rapidity region points to the direction of the target spectator which is the direction of the impact parameter vector. Therefore, we conclude that the Φ_0, which is the direction defined from the transverse momentum vector of protons (and fragments), points to the direction of the impact parameter vector.

In another thing, the model calculations are requiring the more realistic cascade calculation which simulate including the secondary collisions and resonance processes. From this pion of view, we employ relativistic quantum molecular dynamics (RQMD) cascade model and discuss comparing our data in the next section.

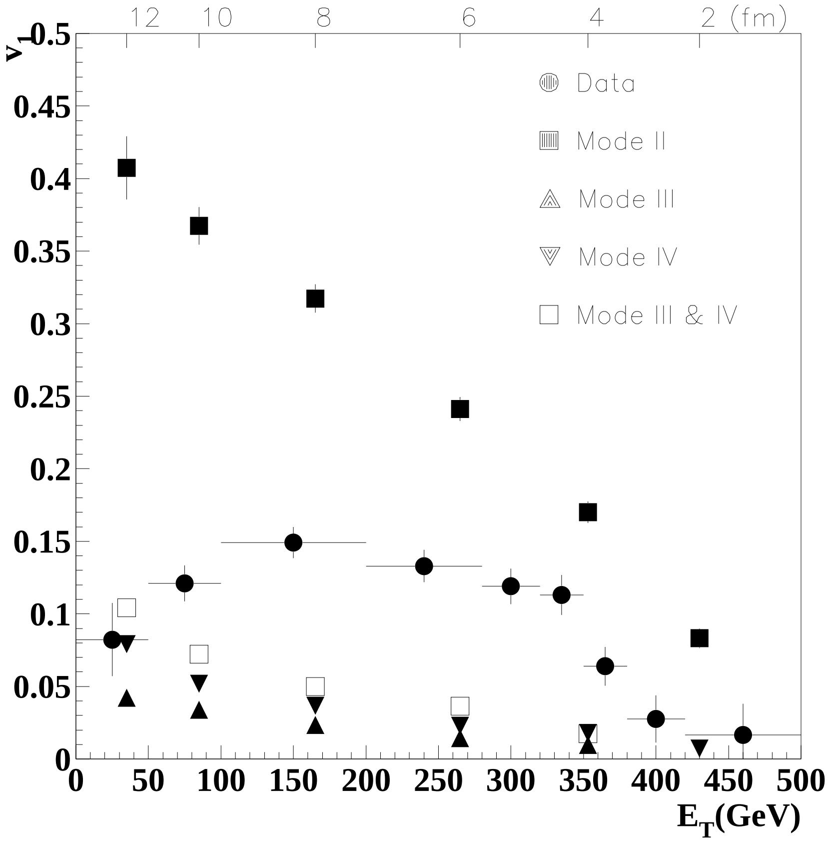

Figure 6.13: Centrality dependence of v_1 obtained from the model calculations and the experimental data for protons. Open squares show the result for the combination of mode III and IV.

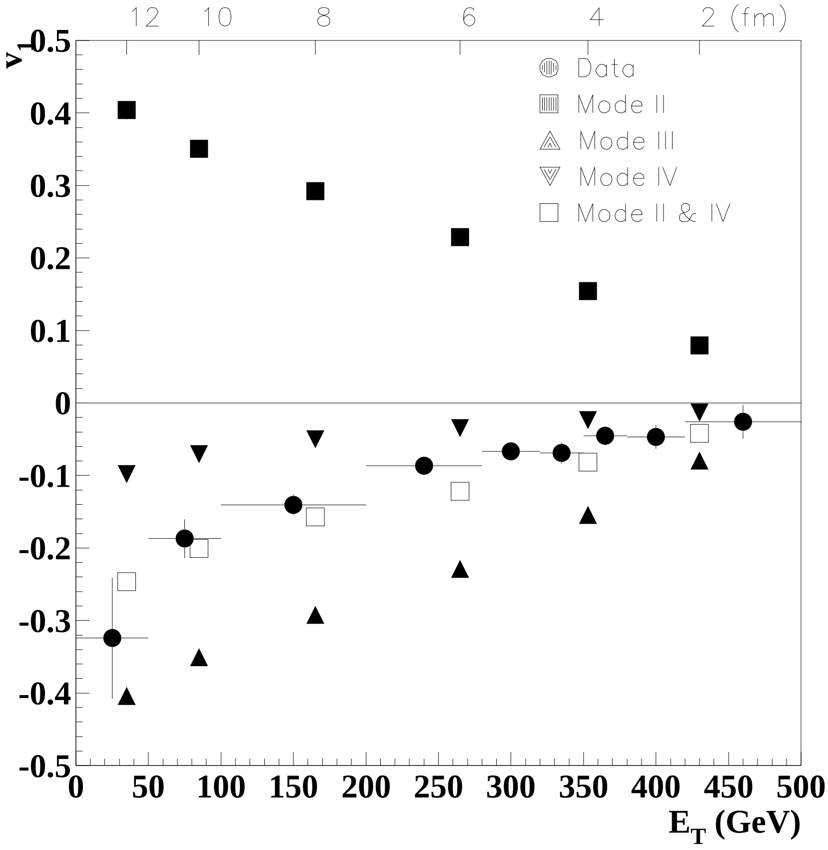

Figure 6.14: Centrality dependence of the v_1 obtained from the model calculations and the experimental data for pions. Open squares show the result for the combination of mode III and IV.

6.3 Relativistic Quantum Molecular Dynamics (RQMD) Model

In the preceding section, we discussed the secondary interaction processes would play a key role to explain the anisotropic emission. In order to understand the experimental data including such a effect, we introduce a intranuclear cascade model which has successfully predicted the anisotropic particle emission as well as particle production at AGS energy [23, 28] and also predicted particle production at SPS [52]. This model is called as Relativistic Quantum Molecular Dynamics Model (RQMD) provided by Sorge *et al.* [53].

In this model, the motion of particles is described in the classical dynamical propagation. In order to prove the Lorentz-invariance, the phase space is extended to 8N dimensions which consist of the positions and momenta of the N particles as 4-vectors. Consequently, every particles carries its own time and energy.

Collisions occur for any two particles when the proper time is equivalent and their minimum distance, $d \ll \sqrt{\sigma/\pi}$ is fulfilled in their center of mass system, where σ is the cross section. The experimentally measured cross sections in the free space are used.

The particle production mechanism is treated as the results of the decay of excited resonances produced in inelastic collisions. The lower mass resonance contributions are predicted by the branching ratios extracted from the experimental data. To predict multi-particle production from the higher energy collisions, a string fragmentation scheme [54] is incorporated along with parameters observed in high energy experiments and contribution of higher resonances is taken into account. However, productions of composite particles from elementary particles are not included yet.

For convenience, the direction of the impact parameter vector is fixed to the same direction as the simple model depicted in Figure 6.11.

6.3.1 Pb + Pb Collisions in RQMD

Utilizing RQMD model, Pb + Pb collisions are simulated. The azimuthal particle emissions at Pb + Pb collisions are calculated for the comparison. In this simulation, the direction of the impact parameter vector is fixed to zero degree in the azimuthal angle. The particles produced and emitted after the intranuclear cascade process are filtered with the Plastic Ball acceptance to compare with the experimental data.

The azimuthal angle distribution of protons and pions are shown on the left half and the right half of Figure 6.15, respectively. It is clearly seen that the azimuthal anisotropic emission for protons and pions exist in the simulation. Moreover, protons are enhanced at $\phi = 0^o$, where the target spectator is sitting, while pions are enhanced at $\phi = 180^o$.

The observed anisotropy parameterized as v_1 is plotted as a function of E_T for both of protons and pions in Figure 6.16. Our data are also plotted with closed circles. For the pions, RQMD results also indicate that the anisotropy becomes larger with decreasing the E_T (increasing the impact parameter) monotonically. Moreover, the absolute v_1 agrees with our data quite well. For proton, the magnitude of v_1 becomes maximum around the mid-central collisions and slightly decreases in the central and peripheral collisions, which is not produced in our model calculation. This tendency is consistent with our data. However, the absolute value is almost twice larger than our data, although successfully predict the multiplicity distribution of protons (See Appendix B.1). One of the reasons to explain this discrepancy is that the RQMD does not take into account the production of fragments from nucleons while fragments are removed from proton samples in the real data. Protons emitted to the same direction, are likely to be compounded into fragments, or detected as heavier particles if those get into the same module of the Plastic Ball. The anisotropy of v_1 is obtained from the data including deuterons and tritons and is plotted with closed triangles in Figure 6.16. It shows those particles produce larger anisotropy as is expected.

In this RQMD model calculations, it is found that the protons are emitted to the direction of the impact parameter ($\phi = 0^o$), while pions are opposite of protons. The anti-correlation between them is reproduced in RQMD. Moreover, the direction of proton emission is face to the target spectator. This result is consistent with our simple model calculations. The RQMD results are confirming that the direction of Φ_0 points to the direction of the impact parameter vector.

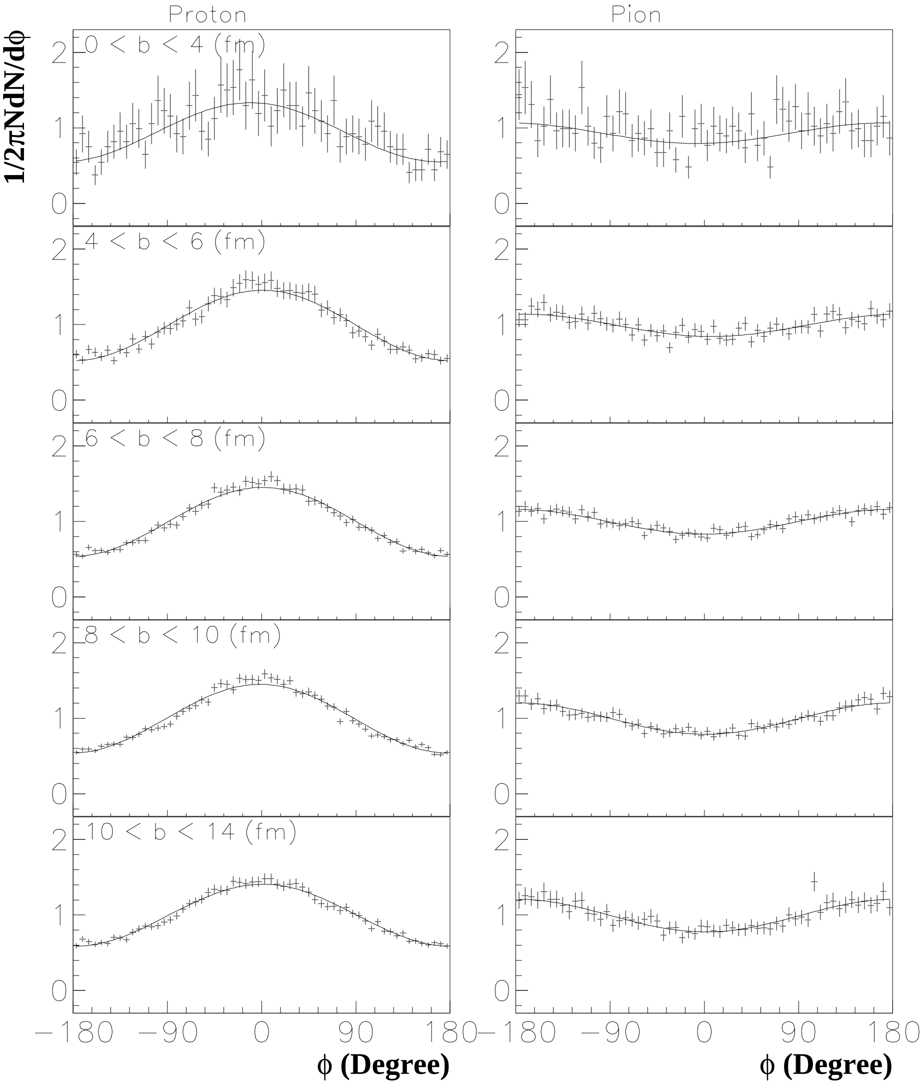

Figure 6.15: Azimuthal angle distribution of proton and pion simulated in RQMD v2.3 [53]

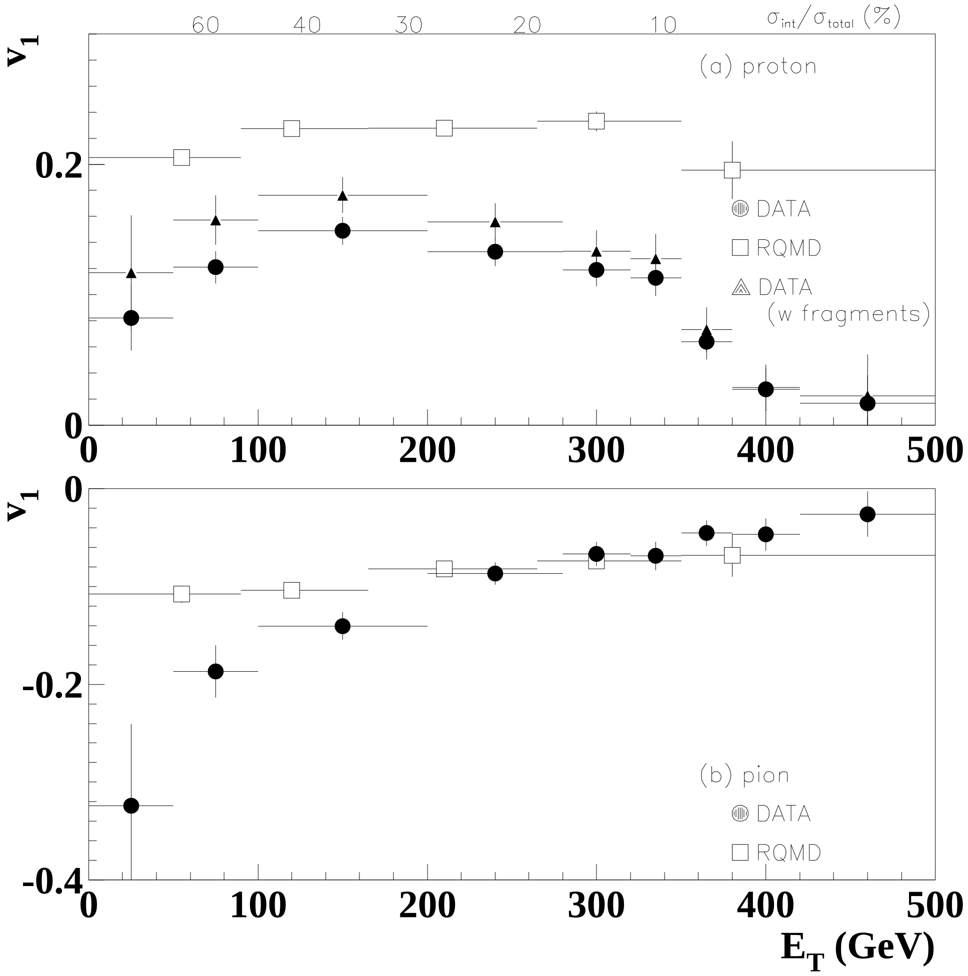

Figure 6.16: Centrality dependence of v_1. The upper panel is for proton and the lower panel is for pion. In the both figures, closed circles show the data and open squares show RQMD prediction. The closed triangles in the upper panel show the results including deuterons and tritons.

Chapter 7

Conclusion and Summary

The measurements of particle production at 158 AGeV Pb + Pb collisions had been carried out at WA98 experiment in CERN SPS. Particles produced around the target rapidity region were observed by the Plastic Ball detector with a full azimuthal coverage. The particle identification for π^+, proton, deuteron and triton had been performed by using the $\Delta E - E$ particle identification method. For better identification of pions, a delay signal which is originated from a π^+ decay was required.

In order to study the characteristics of particle emission at 158 A GeV Pb + Pb collisions, the azimuthal angle, Φ_0, was defined as the direction of total transverse momentum vector from protons, deuterons and tritons event by event. The azimuthal anisotropy of particle emission was studied by the subevent analysis related to the Φ_0. In mid-central collisions, a clear correlation was seen between two azimuthal angles defined by each subevent. The experimental resolution of the Φ_0 was estimated as $\langle \cos(\Delta\Phi_0) \rangle = 0.377$ from this analysis.

The azimuthal anisotropy of particle emission with respect to the Φ_0 was studied for protons and pions as a function of centralities. Protons and pions showed anisotropic emission and protons tended to be emitted to the same direction as Φ_0, while pions were emitted to the opposite direction. The strength of the anisotropy, quantified as v_1, showed clear centrality dependence. Protons indicated maximum anisotropy at the mid-central collisions and decreased towards the central and peripheral collisions. While for pion, the anisotropy showed monotonic increase with decreasing the centrality.

In order to understand the mechanism of those anisotropic emissions, the geometrical participant-spectator model with interaction processes was employed. In this model calculation, we estimated the effects of four processes (mode I $\sim$ IV) on the azimuthal anisotropic emission step by step. This model explained that the anti-correlation of protons and pions was produced by the rescattering of protons and pions. The pions which are emitted to the target spectator direction are likely to be reduced by the spectator though the absorption and resonance processes. On the other hand, the protons are likely to be enhanced to the target spectator direction, because of additional proton emissions from the target spectator through the rescattering and the resonance processes. As a result of these processes, it was found that protons show the tendency to be emitted to the azimuthal direction of the target spectator, while pions were opposite. Whenever the anti-correlation of protons and pions is observed, the emitted direction of protons pointed to the direction of the target spectator which is the direction of the impact parameter vector.

This simple model calculation also suggested the importance of the secondary interactions in the target spectator. Motivated by this requirement, the intranuclear cascade model, RQMD was introduced. In RQMD, it was found that protons tended to be emitted to the direction of the target spectator, while pions tended to be emitted to the opposite direction. The RQMD gives better reproduction of the anisotropies of pions and protons than the simple model.

From those model calculations reaction mechanism of the anisotropies are semiquantitatively understood. Consequently, it was confirmed that the azimuthal direction of protons at the target rapidity region pointed to the direction of the target spectator, which is the direction of the impact parameter vector. Therefor, we conclude that the Φ_0 pointed to the direction of the impact parameter vector.

In this thesis, we established the technique to define the azimuthal direction of the impact parameter at 158 A GeV Pb + Pb collisions as a first time. This contribution is expected to provide a new additional information of particle production at 158 A GeV Pb + Pb collisions.

Appendix A

Resolution of the reaction plane

A.1 Numerical Method

The another numerical method to estimate the resolution of the reaction plane is also performed for our data. Now we turn to a discussion of **Q** determined in Equation 5.1. If **Q** were a just a sum of randomly oriented momenta, then this relation must be approved: $\langle Q^2\rangle = \langle\sum p_t^2\rangle$. Because

$$\begin{aligned} \langle Q^2 - \sum p_t^2\rangle &= \langle\left(\sum p_t\right)^2 - \sum p_t^2\rangle \\ &= \langle\left(\sum p_t^2 - \sum_{\mu\neq\nu} p_{t_\nu} p_{t_\mu}\right) - \sum p_t^2\rangle \\ &= \langle\sum_{\mu\neq\nu} p_{t_\mu} p_{t_\nu}\rangle \\ &= \langle\sum \left|p_{t_\mu}\right| \left|p_{t_\nu}\right| \cos\left(\phi_\mu - \phi_\nu\right)\rangle \end{aligned} \tag{A.1}$$

the averaged cosine of the last equation is always zero if ϕ_μ and ϕ_ν are not correlated at all. However, what we get is non zero but $\langle Q^2 - \sum p_t^2\rangle = 0.277$ at the mid-central collisions (Class G:100 $< E_T <$ 200 GeV). Furthermore, the equation A.1 can be expanded;

$$\begin{aligned} &= \langle\sum \left|p_{t_\mu}\right| \left|p_{t_\nu}\right| \cos\left\{\left(\phi_\mu - \Phi_R\right) - \left(\phi_\nu - \Phi_R\right)\right\}\rangle \\ &= \langle\sum \left|p_{t_\mu}\right| \left|p_{t_\nu}\right| \left\{\cos\left(\phi_\mu - \Phi_R\right)\cos\left(\phi_\nu - \Phi_R\right) + \sin\left(\phi_\mu - \Phi_R\right)\sin\left(\phi_\nu - \Phi_R\right)\right\}\rangle \\ &= \langle\left(\sum p_{t_\mu}\cos\left(\phi_\mu - \Phi_R\right)\right)^2\rangle \end{aligned} \tag{A.2}$$

It indicates that this values is the square of the average transverse momentum on the ideal direction, Q_x. Thus,

$$\langle Q_x \rangle \equiv \sqrt{\langle Q^2 - \sum p_t^2 \rangle} \tag{A.3}$$

In another way, we can calculate the $\mathbf{Q'_x}$ as

$$\mathbf{Q}'_x \equiv \sum p_{t_\mu} \cdot \mathbf{Q}_\mu / Q_\mu \tag{A.4}$$

where $\mathbf{Q}_\mu$ is a vector of total transverse momentum determined from all particles in one event excluding the μ^{th} particle:

$$\mathbf{Q}_\mu = \sum_{\nu \neq \mu}^{\mathbf{M}} \left[\mathbf{p_x}_\nu, \mathbf{p_y}_\nu \right]. \tag{A.5}$$

thus $\mathbf{Q}_\mu / Q_\mu$ indicates the unit vector of the total transverse momentum direction evaluated from the remaining particles. If we take the ratio of them,

$$\begin{aligned} \frac{\langle Q'_x \rangle}{\langle Q_x \rangle} &= \frac{\langle \sum p_{t_\mu} \cos(\phi_\mu - \Phi_0) \rangle}{\langle \sum p_{t_\nu} \cos(\phi_\nu - \Phi_R) \rangle} \\ &= \frac{\langle \sum p_{t_\mu} (\cos(\phi_\mu - \Phi_R) \cos(\Phi_0 - \Phi_R) + \ldots\ldots) \rangle}{\langle \sum p_{t_\nu} \cos(\phi_\nu - \Phi_R) \rangle} \\ &= \langle \cos(\Phi_0 - \Phi_R) \rangle \end{aligned} \tag{A.6}$$

it is equivalent to the resolution factor $\langle \cos(\Phi_0 - \Phi_R) \rangle$.

Appendix B

Comparison with RQMD

B.1 Cross Section

First of all, the rapidity distributions dN/dy obtained at experimental data are compared with RQMD results for the central, mid-central and peripheral collisions in Figure B.1. The experimental results almost agree with RQMD results at the target rapidity region.

B.2 Azimuthal Distribution in p + Pb collisions

We move to the discussion for the possibility to reproduce the azimuthal anisotropic emission concerning on the the participant region. Before going into the full cascade calculation of Pb + Pb collisions we start from an elementary process of p + A collision at RQMD. Utilizing the RQMD model, p (fixed) + Pb (158 AGeV) collisions are simulated, which correspond to the condition of no target spectator. Hence, it is possible to estimate effects caused by the scattering with nucleons in the projectile nucleus.

The azimuthal distribution at the target rapidity ($y < 1$) is shown in Figure B.2(a)(b) for proton and pion. The angle $\phi = 0^o$ indicates the direction of the impact parameter, which is direction from the Pb beam to the proton target. The simulation results show that the azimuthal angle

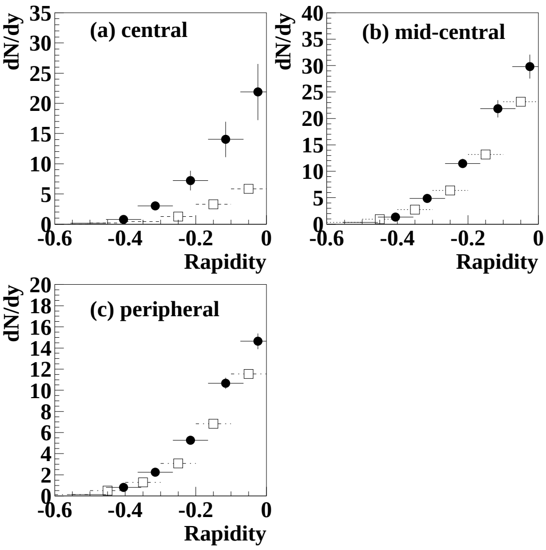

Figure B.1: Comparison with RQMD and experimental results in multiplicity distributions, dN/dy Three figures show difference centralities.

distributions are slightly anisotropic and tend to be emitted to the direction of the impact parameter vector for both of proton and pion.

This tendency can be explained by the multiple-rescattering process in the projectile nucleus. Particles scattered to the direction of the impact parameter would see less nuclear matter, while particles coming out the opposite direction would come across many nucleons of the projectile which have large momentum to the beam direction. Collisions with those nucleons sweep out particles from the target rapidity region by momentum transfer toward the beam direction, as is illustrated in Figure B.3. As a consequence, more particles are emitted to the direction of the impact parameter.

It seems a small effect on p + A collisions, however, it is suggesting the multiple rescattering processes contribute to produce the azimuthal anisotropy of particle emissions.

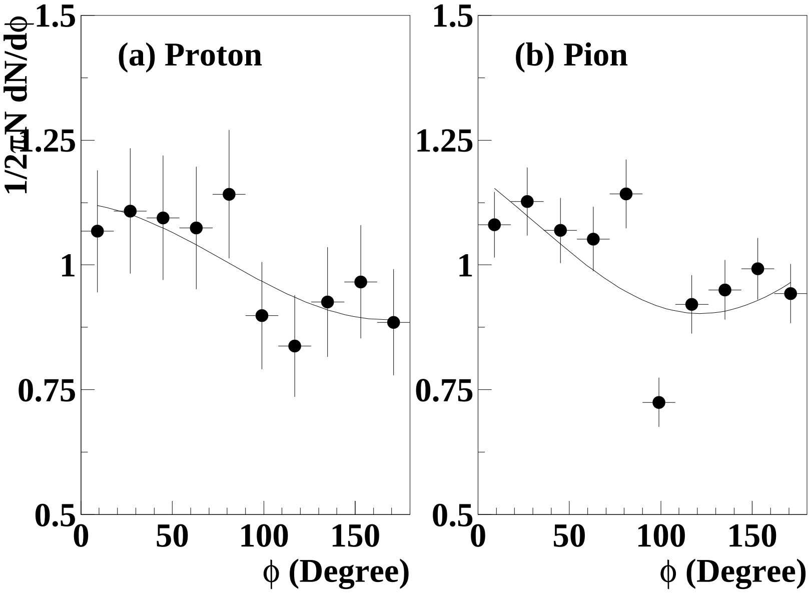

Figure B.2: Azimuthal distribution of protons (left) and pions (right) obtained for p + Pb collisions in RQMD calculations.

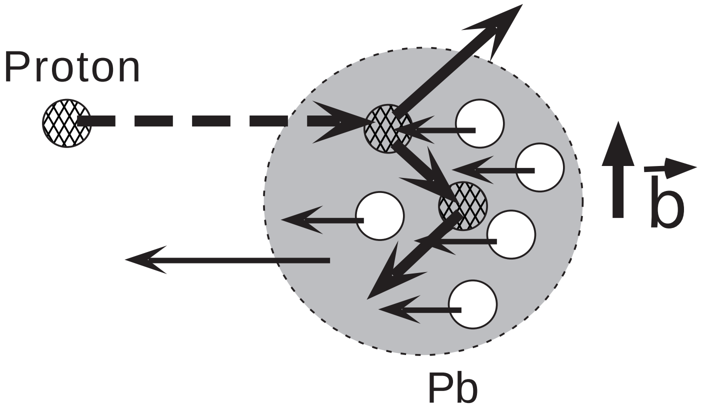

Figure B.3: The schematic picture of p + A collisions It is suggesting the multiple-rescattering process contribute to produce the azimuthal anisotropy of particle emissions.

B.3 Interpretation from RQMD

The question is that the protons observed by the Plastic Ball is originally from the participant or the spectator? In the simple model calculation, we understand that the anisotropic emission of protons is generated by additional protons which are emitted from the target spectator through the collision processes. If the anisotropy is caused by such protons, the number of protons in the spectator is reduced.

The number of nucleons in the spectator, N_{spec}^{RQMD}, is estimated by requiring the ZDC acceptance filter and is plotted with open triangles in Figure B.4. In the RQMD calculation, it is possible to distinguish the nucleons which do not have any interactions. The number of those nucleons in spectator, $N_{spec}^{no\_int}$, is calculated for the several impact parameter regions in RQMD results. Then $N_{spec}^{no\_int}$ is compared with the number evaluated from the geometrical participant-spectator model, N_{spec}^{GEOM}. In Figure B.4, the $N_{spec}^{no\_int}$ and N_{spec}^{GEOM} are also plotted as a function of the impact parameter. The N_{spec}^{RQMD} well agree with N_{spec}^{GEOM}, however, the $N_{spec}^{no\_int}$ is smaller than N_{spec}^{GEOM} for the whole impact parameter range. Especially, the discrepancy seems to be the largest around the middle impact parameters. This result suggests that larger number of nucleons participate in interactions than one expected from the geometrical participant-spectator model. It is consistently understood by our models calculation. Because some of nucleons are removed from the spectator region through interaction processes such as rescattering, resonances and so on. Furthermore, the difference between $N_{spec}^{no\_int}$ and the N_{spec}^{GEOM} is presented in Figure B.5. The number of difference reaches at the maximum value at the impact parameter of ~ 8 fm This dependence is quite similar to the centrality dependence observed in v_1 of protons, experimentally.

Our interpretation is following; the protons around the boundary of spectator region are scattered by other nucleons then coming out to the Plastic Ball acceptance. Those protons are anisotropically distributed in azimuthal angle. The number of nucleons in this boundary region is evaluated with changing the distance, R_b from the origin (the center of the impact parameter in Figure B.6). In Figure B.5, those number are plotted as a function of the impact parameter for the R_b from 1 fm to 6 fm by 1 fm step together with the $N_{spec}^{no\_int}$. The maximum value and the impact parameter at the maximum are increasing with increasing the distance, R_b and it is found that N_{spec}^{GEOM} agree with $N_{spec}^{no\_int}$ at the R_b of 3 fm, qualitatively. The RQMD result is suggesting that the nucleons in the boundary region of the spectator, would have been interacted with other particles. As a result of the interactions, those scattered nucleons contribute to produce the anisotropic emission. The maximum anisotropy observed around the impact parameter of 8 fm is interpreted the correspondence with the maximum number of nucleons in the boundary.

Thus, the anisotropy of particle emission observed at the target rapidity region is consistently understood as the results of the interaction processes at the target spectator of the produced particles.

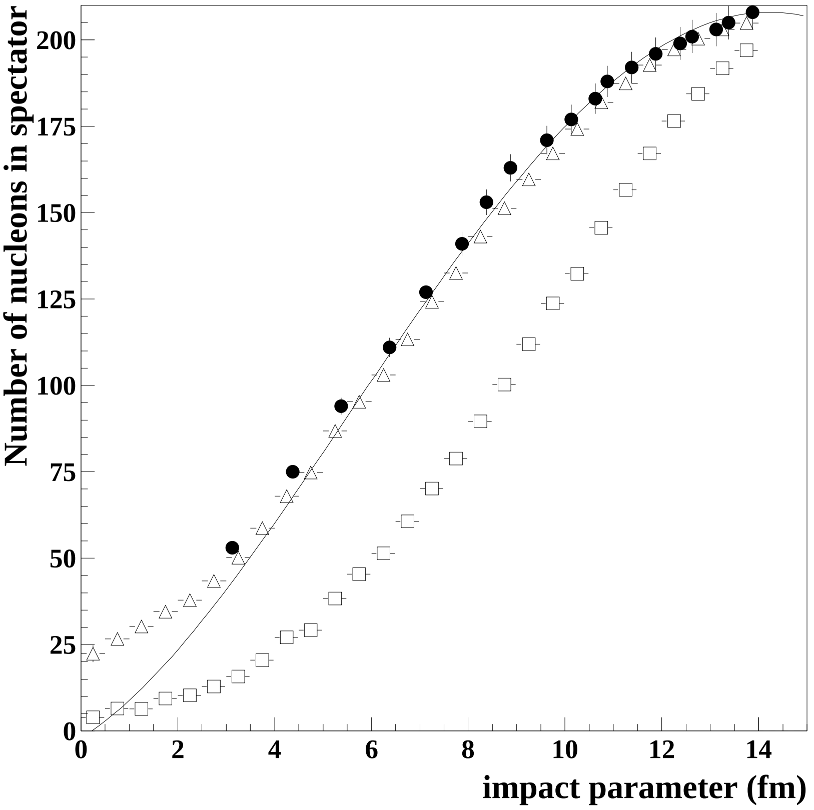

Figure B.4: Number of nucleons in projectile spectator matter versus impact parameter. The closed circles indicate the data calculated from measurement by ZDC. The solid line is obtained from geometrical calculation of colliding nuclei. The open triangles show that number obtained in RQMD and open squares show the number of nucleons which have never had any interactions through RQMD calculations.

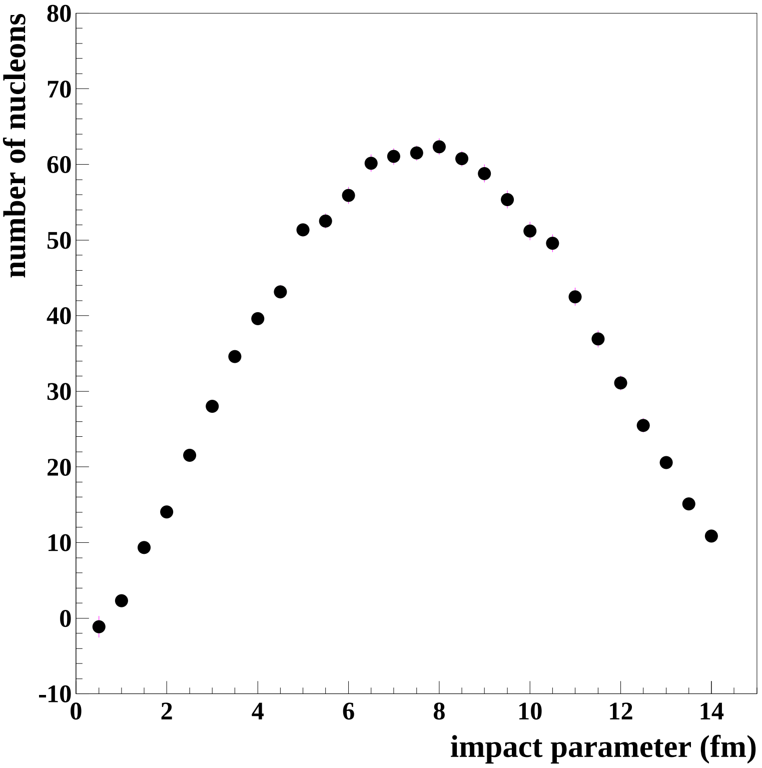

Figure B.5: Difference of the number of nucleons in projectile spectator between the geometrical calculation (solid line in preceding figure) and no interacted nucleons in RQMD (open squares in the same figure)

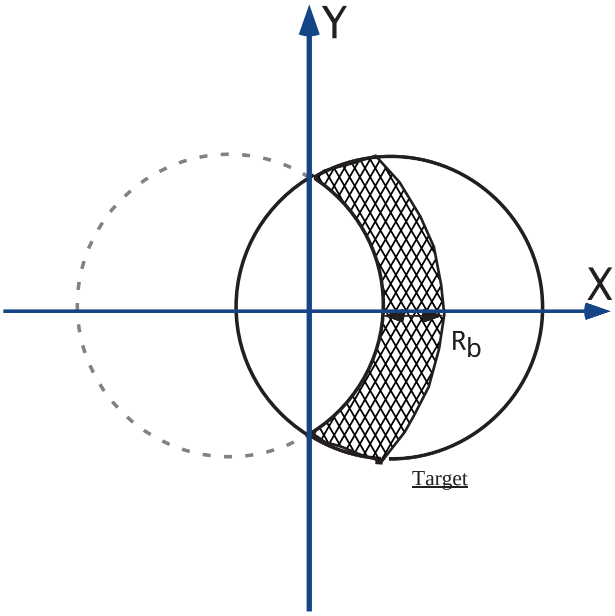

Figure B.6: Schematic beam view.

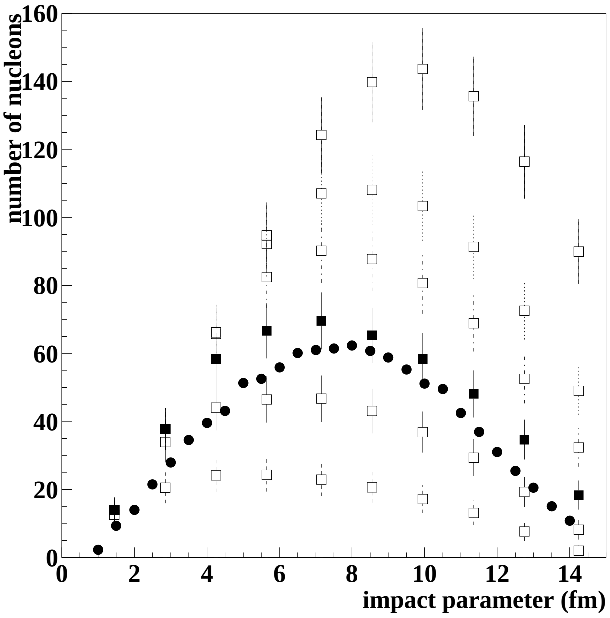

Figure B.7: Number of nucleons in the boundary (hatched region in the Figure B.6) as a function of the impact parameter.

B.4 Average Transverse Momentum

The average transverse momentum on the impact parameter vector is compared with RQMD calculation in Figure B.8. The positive side and the negative side correspond to protons and pions, respectively. The rapidity dependence of $\langle p_x \rangle$ for protons is maximum at $y = -0.2$ for both the experimental data and RQMD calculation. However, the RQMD prediction is almost a factor of 2 larger than the data, On the other hand, at AGS energies, the cascade mode RQMD calculations underpredict the observations by about a factor of two but the good agreement is obtained when mean field effects are included [28] (See Figure 2.6). In this figure, the $\langle p_x \rangle$ of protons, deuterons and tritons are plotted in the summing over the Plastic Ball acceptance. Those $\langle p_x \rangle$ are scaled with the mass as is seen deuteron and triton and become closer to RQMD prediction. Therefore the disagreement of the proton data and RQMD is due to the effect of heavy fragments which are excluded in the experimental data. At SPS energies, mean field effects are expected to be smaller, hence the cascade calculation predicts better than in AGS energies.

For pions, the RQMD calculations show the agreement with the data again.

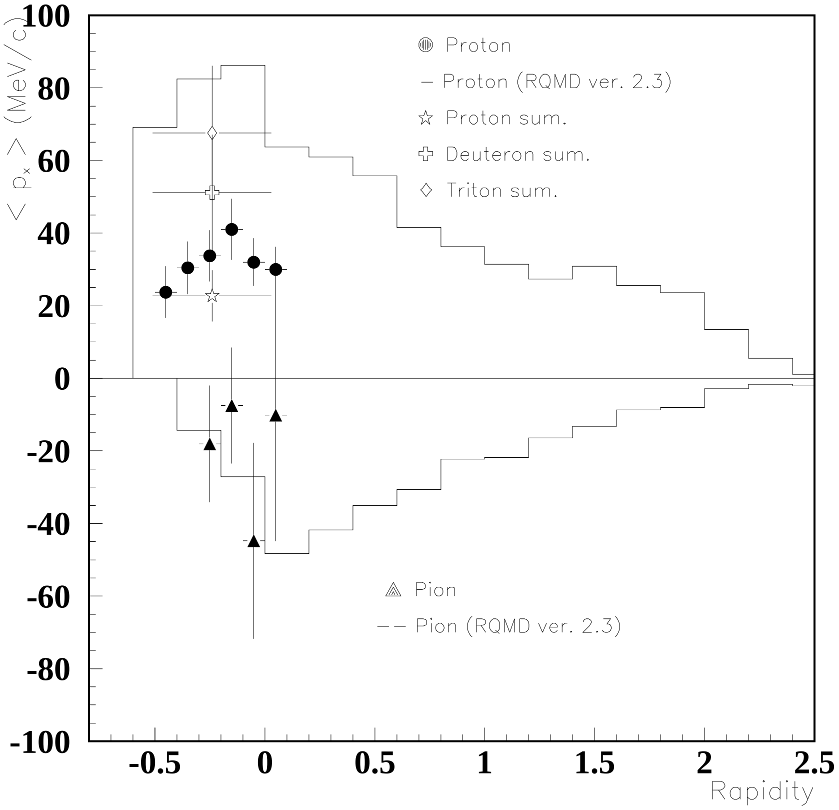

Figure B.8: Comparison of average transverse momentum on the impact parameter vector with RQMD. The open marks indicate $\langle p_x \rangle$ in the summing over the Plastic Ball acceptance, for protons, deuterons and tritons [55].

Appendix C

Comparison between AGS and SPS

C.1 Centrality Dependence

The centrality dependence of the strength of the azimuthal anisotropy is obtained for nucleons at AGS (Figure 2.5) and SPS energies (Figure 5.13) around the target/beam rapidity region. The results show the maximum anisotropy around the mid-central for both energies. However, the impact parameter of the maximum point corresponds to $\sim 4fm$ at AGS energy, while this indicates $\sim 8fm$ at SPS energy. This change of the maximum point might be caused by the the difference of multiplicity of produced particles. As we considered from RQMD comparison, the maximum anisotropy seems to be connected with the number of nucleons in the boundary region of the spectator. Since less number of particles are produced at AGS energy, the effective number of nucleons which hit the nucleons in the spectator and produce anisotropy is comparable in the smaller impact parameter at AGS energy with the larger impact parameter at SPS energy.

C.2 Average Transverse Momentum

The average transverse momentum on the impact parameter vector is compared between AGS and SPS energies. In Figure C.1, $\langle p_x \rangle$ for protons (on the top) and pions (on the bottom) are plotted as a function of the normalized rapidity, $(y - y_{cm})/y_{cm}$. The $\langle p_x \rangle$ of protons at SPS energy show almost 1/3 of that of AGS energy. On the other hand, the $\langle p_x \rangle$ of pions for both energies show opposite sign and comparably small value.

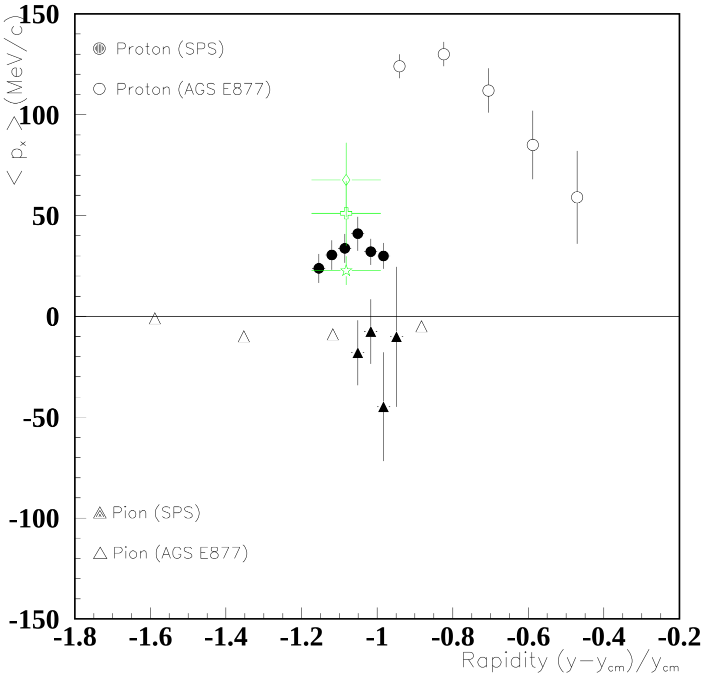

Figure C.1: Average transverse momentum on the impact parameter vector $\langle p_x \rangle$ for protons (on the top) and pions (on the bottom) as a function of the normalized rapidity, $(y - y_{cm})/y_{cm}$. The results obtained at AGS and SPS energies are represented.

Bibliography

[1] C-Y. Wong. Introduction to high-energy heavy-ion collisions, 1994.

[2] J.D. Bjorken. *Phys. Rev.*, **D27**, 865, 1983.

[3] H.R. Schmidt and J. Schukuraft. The physics of highly relative heavy-ion collisions, j.phys. g, 1991.

[4] T. Abbott et al. *Phys. Rev. Lett.*, **64**, 847, 1990.

[5] T. Abbott et al. *Phys. Rev. Lett.*, **66**, 1567, 1991.

[6] J.B. Costales et al. *Nucl. Phys.*, **A525**, 455c, 1991.

[7] Y. Miake. private communication.

[8] F. Videbek. *Nucl. Phys.*, **A590**, 249c, 1995.

[9] V. Blobel et al. *Nucl. Phys.*, **B69**, 454, 1974.

[10] J-Y. Ollitrault. *Phys. Rev.*, **D46**, 229, 1992.

[11] J-Y. Ollitrault. *Phys. Rev.*, **D48**, 1132, 1993.

[12] P. Filip. *hep-ex/9605001*, 1996.

[13] D. H. Rischke. *Nucl. Phys.*, **A610**, 88c, 1996.

[14] H. Gutbrod et al. *Rep. Prog. Phys*, **52**, 1267, 1989.

[15] H. Å.Gustafsson et al. *Phys. Rev. Lett.*, **52**, 1590, 1984.

[16] H. Å.Gustafsson et al. *Phys. Lett.*, **B142**, 141, 1984.

[17] P. Danielewicz and G. Odyniec. *Phys. Lett.*, **B157**, 146, 1985.

[18] L.B. Venema et al. *Phys. Rev. Lett.*, **71**, 336, 1993.

[19] D. Brill et al. *Phys. Rev. Lett.*, **71**, 835, 1993.

[20] V. Ramillien. *Nucl. Phys.*, **A587**, 802, 1995.

[21] H.G. Ritter et al. *Nucl. Phys.*, **A583**, 491c, 1995.

[22] M.D. Partlan et al. *Phys. Rev. Lett.*, **75**, 2100, 1995.

[23] J. Barrette et al. *Phys. Rev. Lett.*, **73**, 2532, 1994.

[24] T.K. Hemmick et al. *Nucl. Phys.*, **A610**, 63c, 1996.

[25] Y. Zhang. PhD thesis, SUNY at Stony Brook, 1995.

[26] B. Blättel et al. *Phys. Rev.*, **C43**, 2728, 1991.

[27] J. Barrette et al. *Nucl. Phys.*, **A590**, 259c, 1995.

[28] W-C. Chang. PhD thesis, SUNY at Stony Brook, 1997.

[29] N. Angert et al. Cern heavy-ion facility design report. technical report, cern, 1993.

[30] T. Chujo et al. *Nucl. Inst. and Meth.*, **A383**, 409, 1996.

[31] T.C. Awes et al. *Nucl. Inst. and Meth.*, **A279**, 479, 1989.

[32] G.R. Young et al. *Nucl. Inst. and Meth.*, **A279**, 503, 1989.

[33] A. Baden et al. *Ncul. Inst. and Meth*, **203**, 189, 1982.

[34] J.M. Rubio et al. *Nucl. Inst. and Meth.*, **A367**, 358, 1995.

[35] J.M Rubio. PhD thesis, University of Geneva, 1997.

[36] H. Naef. PhD thesis, University of Geneva, 1997.

[37] P.A. Steinberg. PhD thesis, Massachusetts Institute of Technology, 1998.

[38] S. Neumaier et al. *Nucl. Inst. and Meth.*, **A360**, 593, 1995.

[39] T. Peitzmann et al. *IKP-MS-96/0101*, 1996.

[40] A.L. Wintenberg et al. In *Proc. of Electronics for Future Colliders Conference*, 1994.

[41] C.M. Manus and Strickler. 1982.

[42] M. Purschke. *ANPACK manual.* GSI.

[43] CERN. *library PAW manual.*

[44] K. Nagatani T. Shimoda, M. Ishiraha and T. Nomura. *Nucl. Inst. and Meth.*, **165**, 261, 1979.

[45] A.M. Poskanzer and S.A. Voloshin. *nucl-ex/9805001*, 1998.

[46] The American Physical Society. Review of particle properties, 1994.

[47] F. Shimizu et al. *Nucl. Phys.*, **A389**, 445, 1982.

[48] K. Niita et al. *Phys. Rev.*, **C52**, 2620, 1995.

[49] S.A. Bass et al. *Phys. Lett.*, **B302**, 381, 1993.

[50] S.A. Bass et al. *Phys. Rev.*, **C51**, 3343, 1995.

[51] H. Stöcker R. Mattiello, H. Sorge and W. Greiner. *Phys. Rev.*, **C55**, 1443, 1997.

[52] H. Sorge. *Phys. Lett.*, **B402**, 251, 1997.

[53] H. Stöcker H. Sorge and W. Greiner. *Ann. of Phys.*, **192**, 226, 1989.

[54] G. Gustafson B. Andersson and B. Nilsson-Almqvist. *Nucl. Phys.*, **B281**, 289, 1987.

[55] H. Schlagheck. private communication.